Blast response of structures: limits to deformation and fluid-structure interactions

Ye Yuan

Department of Mechanical Engineering

University College London

A thesis submitted for the degree of

Doctor of Philosophy

November 2015

Declaration

I, Ye Yuan, confirm that the work presented in this thesis is my own. Where information has been derived from other sources, I confirm that this has been indicated in the thesis.

Abstract

This thesis investigates the blast response of simple structural components - fully clamped beams and plates - underwater and in air. Experimental work by others have shown that, with increasing loading intensity, these components deform in one of either three modes: mode I (large inelastic deformation), mode II (tensile tearing) or mode III (transverse shear failure). The aim of this thesis is to develop theoretical and numerical models that can accurately predict these damage modes, taking into account the effects of fluid-structure interactions, for both impulsive and non-impulsive blast loadings.

A fully-clamped ductile beam model is proposed that is capable of capturing large elasto-plastic deformation, progressive damage and failure through detachment from its supports. Predictions by the model were validated against experimental data in the literature and with finite element models developed in this thesis. Parametric studies were also performed to elucidate the effects of loading duration on the mode of deformation and the conditions governing their transition. Numerical evidence on elimination of pulse-shape effects using an effective rectangular pulse loading (Youngdahl's approach) has been provided.

The effects of fluid-structure interaction (FSI) are investigated for fully-clamped, elasto-plastic beams in deep underwater explosions and intense air blast loadings. The main objective is to understand how the introduction of fully-clamped clamped supports alter existing well-known results grounded on rigid, free-standing counterpart; and, to quantify how different modes of deformation affects the impulse and energy transmitted to the structure by the blast wave. Sensitivity analyses were carried out to elucidate the dependence of the results on the beam's aspect ratio and inertial mass.

The deformation and failure of fully clamped rectangular plates subjected to blast loading are modelled numerically using finite element method. The numerical results are validated against experimental data. Deformation maps delineating the different deformation régimes for different combinations of blast impulse and aspect ratio are constructed for plates of equal mass. The effects of imposing a finite period, as opposed to a zero-period, pressure pulse upon the deformation mode and maximum deflection are discussed.

Acknowledgements

This thesis would not have been possible without the advice, help and support from my supervisor Dr. PJ Tan to whom I wish to acknowledge here my indebtedness. This work has been much elevated by Dr. Tan's helpful guidance and his incredible attention to detail. His questions and comments always pushed me, to some extent, further than my original attempt. The almost endless discussions made it possible, not only a constant check for gaps and inconsistencies, but also a better understanding of the intricate links between various parts of this project.

I have greatly benefited from the advices, comments, critical reading of various chapters of this thesis by many helpful colleagues and friends. In particular, I would like to acknowledge those of Dr. Paul Fromme, Ioannis Christodoulou, Anna Chiara Faralli, Liu Liu, Yuanchang Liu and Rui Song of the Department of Mechanical Engineering at UCL; Dr. Amir Schojaei of Halliburton Energy Services, Houston; Dr. Kevin Lau of the Departments of Surgery and Biomedical Engineering, University of Michigan; Yinhua Zhou of the Department of Aerospace Engineering, Northwestern Polytechnical University. Comments and suggestions made by anonymous referees have been particularly helpful.

Last, but not least, I want to acknowledge the support and encouragement of my parents for what has been a challenging few years.

Contents

List of Figures

List of Tables

Nomenclature

a	Half length (longer side) of plate
A	Cross-section area of the beam
b	Half width (shorter side) of plate
B	Width of the beam
c_a	Speed of sound in ambient air condition
c_w	Wave speed in water
C_R	Pressure coefficient
d	Standoff distance
d_0	Length of one-dimensional 'compressed air container'
D	Damage variable
D_q, q	Material strain rate parameters
e	Internal energy
E	Young's modulus
$\bar{E}^F$	Non-dimensional maximum total energy transmitted to a free-standing beam
E^P	Total potential energy
E_{ext}	Impulsive external energy
E^T, E^K	Transmitted energy and kinetic energy of the elasto-plastic beam, respectively
$\bar{E}^T$, $\bar{E}^K$	Non-dimensional maximum E^T and E^K, respectively
E_{ktr}	Residual kinetic energy of the elasto-plastic beam
E_S^b, E_S^s, E_S^m	Bending, shear, membrane energy obtained via the rotational, axial and vertical springs, respectively

E_B^b, E_B^s, E_B^m	Bending, shear, membrane energy of the elasto-plastic beam, respectively
E_i	Incident energy of blast wave per unit area
F	Deformation gradient
G	Shear modulus
H	Beam (or plate) thickness
I	Second momentum of area
I_{ext}	External impulse
I_{ktr}	Residual momentum
I_i	Incident impulse per unit area
$\bar{I}^F$	Maximum total impulse transmitted to a free-standing beam per unit area
I^T, I^K	Transmitted impulse and momentum, respectively
$\bar{I}^T$, $\bar{I}^K$	Non-dimensional maximum I^T and I^K, respectively
I^*	Non-dimensional impulse
$\hat{I}$	Impulse per unit area
j	Iteration number
K_ϕ	Rotation spring stiffness
l	Width of shear band
l_e	Length of plastic hinge
L	Half length of the beam member
L_e	Characteristic length of the first-order element used in the FE model
L_w	Length of water tank in FE model
m_e	Equivalent mass of beam
M	Total mass of the plate
M_B, M_S	Bending moment at the mid-span and support, respectively
M_0	Fully plastic bending moment
M_Y	Bending moment at the elastic limit
M_{ij}	Generalised mass of the beam member
$\bar{M}_B$, $\bar{M}_S$	M_B/M_0, M_S/M_0
$\bar{M}_B^f$, $\bar{M}_S^f$,	$\bar{M}_B$ and $\bar{M}_S$ at the onset of damage, respectively
n	Material hardening coefficient

N	Membrane force
N_Y	Membrane force at the elastic limit
N_0	Fully plastic membrane force
$\bar{N}$	N/N_0
$\bar{N}^f$	$\bar{N}$ at the onset of damage
p	External pressure loading
p_c	Fully plastic collapse force
p_{eff}	Effective pressure loading
p_s	Peak incident overpressure
p_{eff}	Effective pressure
p_I	Incident wave in air and water
p_r	Peak reflection overpressure
p_R	Reflected pressure in air
p_{R1}	Reflected wave in water
p_{R2}	Rarefaction wave in water
p_{Int}	Interface pressure in air and water
$\bar{p}_{\text{Int}}(t)$	Average interface pressure
Q	Transverse shear force
Q_0	Fully plastic shear force
Q_i	Generalised force
Q_Y	Transverse shear force at the elastic limit
Q_S	Transverse shear force at support
$\bar{Q}_S$	Q_S/Q_0
$\bar{Q}_S^f$	$\bar{Q}_S$ at the onset of damage
R	Idea gas constant
t_1, t_2, t_3	Termination time of phase I, II and III, respectively
t_c	Cavitation time
t_d	Pulse duration
t_i	Decay constant
t_y, t_f	Beginning and termination time of plastic deformation, respectively
t_{mean}	Centroid of the effective pulse

T	The time to attain maximum mid-span deflection under a zero-period impulse
$\bar{u}_f^p$	Effective plastic displacement at failure
U_s	Propagation speed of shock front, i.e. shock speed
v_0	Peak initial velocity of 'compressed air container'
V_0	Initial velocity of the structure under impulsive loading
w_i	Generalised displacements
W	Overall transverse displacement of the structural beam system
W_0	Maximum mid-span deflection
W_f	Critical mid-span deflection at mode I→II transition
W_B, W_S	Displacements at the mid-span and support, respectively
W_0^{FSI}, $W_0^{\text{NO FSI}}$	Maximum mid-span deflection with and without FSI effect
$\bar{W}$	$\bar{W} = W_0^{\text{FSI}}/W_0^{\text{NO FSI}}$
x_e	Eulerian coordinate
Z	Undeformed Lagrangian coordinates
β	Ratio of the plastic work absorbed through shearing deformation to the total plastic work done
β_c	Critical value of β to separate mode II and III
β_a, β_w	FSI index in air and water, respectively
$\chi(= b/H)$	Ratio of half width to thickness of plate
$\dot{\epsilon}$	Strain rate
Δ	Total membrane displacement
Δ_S, Δ_B	Membrane displacement at the support and mid-span, respectively
ϵ_{eff}	Effective strain
ϵ_{xx}	Total in-plain effective strain
ϵ_m, ϵ_b	Membrane and bending strain, respectively
ϵ_d, ϵ_r	Uniaxial damage and rupture strain, respectively
$\bar{\epsilon}^p$	Equivalent plastic strain
$\bar{\epsilon}^d$	Damage strain
ϵ_V	Volumetric strain
γ_c	Critical shear strain
γ_{xz}	Transverse shear strain

$\gamma = a/b$	Aspect ratio of plate
γ_a	Specific heat ratio
κ	Curvature of longitudinal axis of beam
$\mathcal{L}$	*Lagrangian* of the structural beam system
ν	Poisson's ratio
ω_d	State variable for damage criterion
ω_s	State variable for shear failure criterion
$\phi_i(x)$	Admissible mode functions
ψ^{el}, ψ^{p}	Elastic and fully plastic stress conditions, respectively
Ψ	Area fraction of plate detached from boundary
ρ	Density of structural material
ρ_a, ρ_w	Air and water density, respectively
σ_y, σ_d	Static and dynamic yield strength, respectively
Θ	Viscous dissipation
φ	Incident pressure profile in air
ξ	Location of the travelling hinge
$\bar{\xi}$	ξ/L

Chapter 1

Introduction and literature survey

1.1 Introduction

An explosion generates an over-pressure which propagates into quiescent ambient air as a blast, or shock, wave. The blast loading is transient in nature, lasting for a few milli-seconds to a few seconds. If the blast wave is sufficiently intense, a target structure is likely to develop large plastic deformation, resulting in partial or complete detachment from its supports. In order to improve structural safety and/or to assess the consequences of the blast hazard, a thorough understanding of the mechanisms of loading, damage and failure of structures to blast loadings is of fundamental importance.

Although the intensity and duration of a blast wave are not normally known in advance, they can broadly be classified into two types, viz. impulsive or non-impulsive. A considerable body of literature exists on characterising the response of structures to impulsive loading where the duration of the blast pulse is insignificant compared to the natural response time of the structure. Analytical and finite element models were successfully developed that are capable of predicting the critical impulsive velocities needed to initiate damage and failure, and they have been shown to be in excellent agreement with experiments. However, the majority of blast loadings in real-life are, in fact, non-impulsive; especially if the source of an explosion occurs at a considerable standoff distance from the target structure. Compared to the abundant literature on the impulsive response of structures, there is limited published literature to date, and relatively little is known, of how structures respond to non-impulsive blast loads.

The interactions between a structure and the blast wave is known as fluid-structure interaction or, for brevity, FSI. The basic concept of FSI is that the receding motion of the structure alleviates the pressure acting on it, and thus reduces the impulse transmitted by the blast wave. Our current state of knowledge on FSI, in both compressible or incompressible medium, is still very much grounded on works based on rigid free-standing structures (Taylor, 1941; Kambouchev et al., 2006, 2007; Hutchinson, 2009), or elastic structures (Schiffer et al., 2012; Schiffer and Tagarielli, 2014, Subramaniam et al., 2009, Teich and Gebbeken, 2011). Moreover, FSI effects are often neglected in many of the current design guidelines. For instance, TM5-1300 (1990) recommends that the reflected blast pulse from a fixed, rigid surface at the relevant standoff distance can be used as the design loading for the structure. This recommendation could potentially lead to large inaccuracies in the predicted structural response. There is a need for more thorough investigations into the role of FSI on the structural response and failure of actual deformable structures - taking into account large elasto-plastic deformation and the influence of supports - to blast loadings; and its implications on momentum and energy transfer from the blast wave. To this end, a comprehensive understanding of the physics of FSI and the ability to accurately model the interactions between a general blast pulse and deformable structural components are needed.

The present thesis outlines a systematic study, by a combination of analytical and numerical modelling, to assess the performance of deformable structures subjected to impulsive and non-impulsive loadings. The topics covered will range from large elasto-plastic deformation, to progressive damage and failure at the supports, through to energy and momentum transfer resulting from fluid-structure interaction in both air blasts and underwater explosions.

1.2 Literature survey

There exists a significant body of research on the blast response of simple structural components - beams, plates, shells, etc. - in topics ranging from fluid-structural interactions to dynamic structural response (large deformation, damage and failure). This section provides a brief review of the pertinent central findings from these works.

1.2.1 Blast loadings on structures

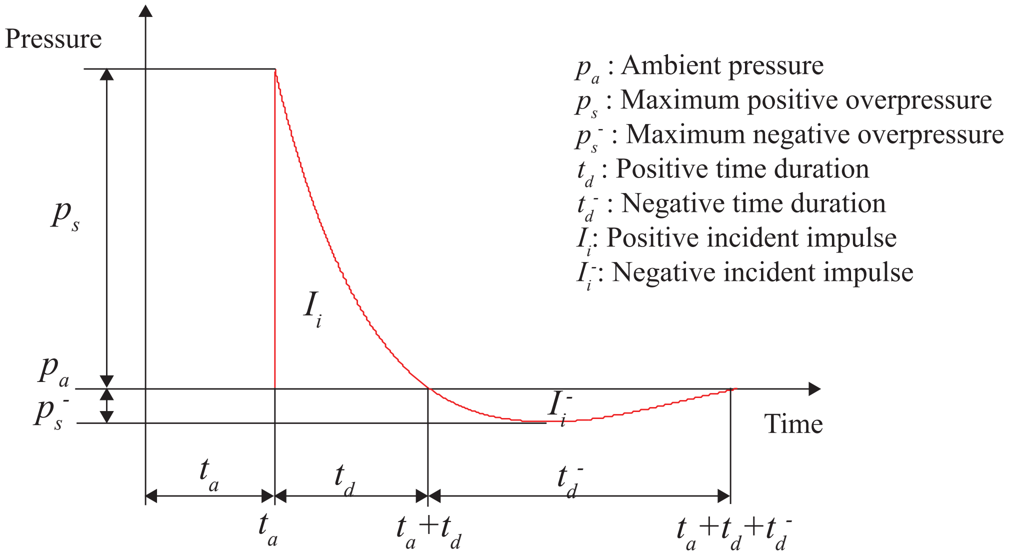

Figure 1.1: Schematic of a typical incident pressure-time history generated by a blast event (TM5-1300, 1990).

Explosions, from conventional or nuclear explosives (American Society of Civil Engineering, 1961, 1985), high pressure gases (Baker et al., 1983) or dust mixtures (Baker et al., 1983), generate gases that expand violently outwards, forcing the surrounding atmosphere away from the expanding volume. A blast wave is generated, as a consequence, by the zone of compressed air that forms, and propagates outwards, in front of the gases. The propagation velocity decreases with time (and distance) but it is typically greater than the speed of sound in the medium. If a pressure transducer is placed at a fixed location, relative to the source of explosion, an incident overpressure (the difference between the static pressure and the ambient atmospheric pressure) of a type shown schematically in Fig 1.1 would be recorded (Feng et al., 2007). Notice that compression is regarded as *positive* in the figure. At $t = t_a$ (arrival time of the blast pulse), the pressure increases rapidly - with a negligibly small rise time - to a peak value $p_s + p_a$; thereafter, it decays monotonically to an ambient level p_a at time $(t_a + t_d)$ - this is known as the 'positive phase' of a blast pulse. It is followed by a period of under-pressure which creates a partial vacuum - known as the 'negative suction phase'- before returning to ambient conditions at time $(t_a + t_d + t_d^-)$.

There exists various empirical formulae for estimating the peak incident overpressure p_s (Brode, 1955; Dewey, 1964; Henrych, 1979; Smith and Hetherington, 1994). For example, Henrych (1979) expressed p_s as a function of scaled distance Z given by

$$p_s = \begin{cases} \frac{14.072}{Z} + \frac{5.540}{Z^2} - \frac{0.357}{Z^3} + \frac{0.00625}{Z^4}, & 0.05 \leq p_s/p_a \leq 0.3 \\ \frac{6.194}{Z} - \frac{0.326}{Z^2} + \frac{2.132}{Z^3}, & 0.3 \leq p_s/p_a \leq 1 \\ \frac{0.662}{Z} + \frac{4.05}{Z^2} + \frac{3.288}{Z^3}, & 1 \leq p_s/p_a \leq 10 \end{cases} \tag{1.1}$$

where $Z = r/W^{1/3}$ (also known as the scaled distance), r is the distance from the source of the explosion to the point of measurement and W is the weight of charge (expressed in TNT-equivalent). Most analytical models neglect the negative suction-phase of a blast pulse (Kinney, 1962; Baker, 1973). One of the simplest approximation of the positive phase of a typical blast pulse is an exponentially decaying pressure profile given by

$$\varphi(t) = e^{-\frac{t}{t_i}}, \quad 0 \leq t \leq \infty \tag{1.2}$$

where the decay constant t_i is chosen so that the peak overpressure p_s and the impulse of the positive phase

$$I_i = \int_0^\infty p_s e^{-\frac{t}{t_i}} \mathrm{d}t \tag{1.3}$$

matches that measured by experiments. Equation 1.2 is commonly used in one-dimensional (1D) studies of a blast wave impinging on rigid plates (Schiffer et al., 2012; Taylor, 1941) or on sandwich panels (Deshpande and Fleck, 2005; Fleck and Deshpande, 2004; Liang et al., 2007; McMeeking et al., 2008., Xue and Hutchinson, 2004).

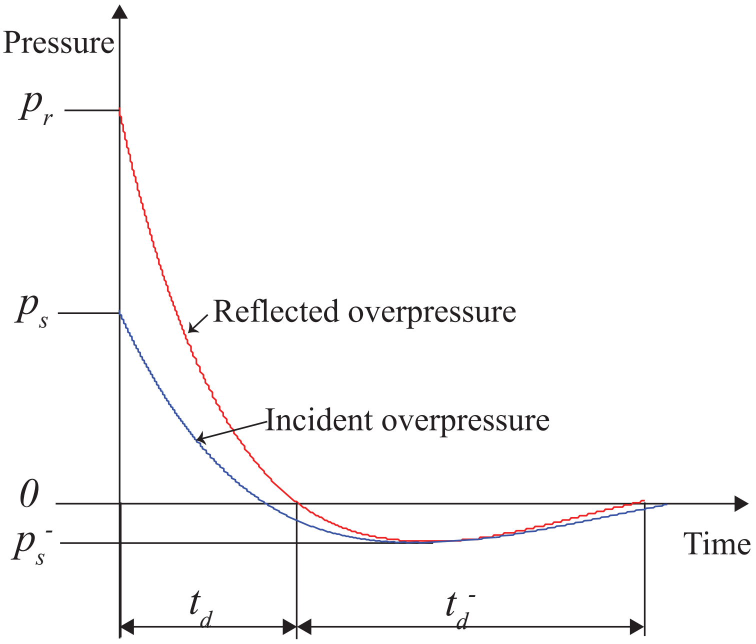

Figure 1.2: Schematic of a reflected pressure-time history from an obstacle (TM5-1300, 1990).

The incident wave is reflected from any surface that is not parallel to the direction of propagation (such as a wall or a structure). Neglecting any attenuation, the reflected pressure profile is often assumed to be similar in profile to the incident but with a higher peak pressure as shown schematically in Fig 1.2. The peak reflected overpressure can be expressed in the form of (Anderson, 2001)

$$p_r = C_R p_s \tag{1.4}$$

where the reflection coefficient C_R is given by the well-known Rankine-Hugoniot relationship as follows:

$$C_R = \frac{8p_s + 14p_a}{p_s + 7p_a}. \tag{1.5}$$

It is clear from Eq. 1.5 that the reflection coefficient ranges between $2 \leq C_R \leq 8$ where the lower limit corresponds to the acoustic range and the upper limit for very strong shocks.

The loading by the blast wave may be categorised into three different régimes - static ($t_d/T \gg 1$), dynamic ($t_d/T \approx 1$) or impulsive ($t_d/T \ll 1$) - depending on the time ratio (t_d/T) where t_d is the duration of the positive phase and T is the natural response time of the structure upon which the blast wave impinges (Smith and Hetherington, 1994). The limiting case for the impulsive régime is termed zero-period impulsive loading (Xue and Hutchinson, 2004) where the pressure profile is insignificant and the structure acquires an instantaneous velocity given by

$$V_0 = \frac{I_i}{m} \tag{1.6}$$

where I_i is given by Eq. 1.3 and m is the mass per unit area of the structure. It will be highlighted later that strong blast loadings can often be approximated - rather accurately - as zero-period impulses (Jones, 1971; Jones, 1976; Yu and Chen, 1992, 2000).

1.2.2 Impulsive response of structures

There exists an extensive literature on the deformation and damage of beams and plates to impulsive loadings: see, for example, Jones (1975, 1978, 1981, 1985, 1989, 1996, 2013), Jones and Shen (1993) and Yu and Chen (1998, 2000). In this section, the focus will be on reviewing the key salient findings.

The classical experiment by Menkes and Opat (1973) showed that the mode of deformation in a fully clamped aluminium (6061-T6) beam subjected to impulsive loading ($t_d/T \ll 1$) can be categorised as: mode I - large inelastic deformation; mode II - tensile-tearing and deformation; mode III - shear-band localisation, as shown in Fig 1.3. Olson et al. (1993) demonstrated that fully clamped square mild-steel plates also exhibit similar damage modes. It is worthwhile noting that the terms 'deformation modes' and 'damage modes' are often used interchangeably. Nurick and Shave (1996) further demonstrated the same for blast-loaded square plates; in addition, they proposed that the mode II deformation may be

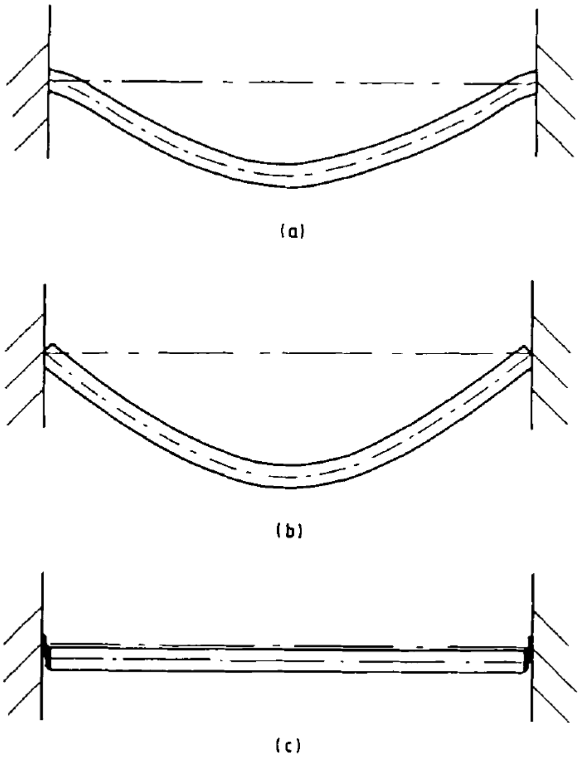

Figure 1.3: Schematic of damage modes for impulsively loaded beams by Menkes and Opat (1973): (a) mode I-large inelastic deformation; (b) mode II-tensile tearing at the supports; (c) mode III-shear-band localisation (Olson et al., 1993).

sub-divided into three distinct régimes of mode II* (through-thickness tearing along the supports); mode IIa (complete detachment from supports with maximum central deflection *increasing* with impulse); mode IIb (complete detachment from supports with maximum central deflection *decreasing* with impulse). Further, experiments by Ramajeyathilagam and Vendhan (2004) showed that the impulsive response of rectangular plates, with aspect ratio $\gamma > 1$, were broadly similar to the square plates reported by Olson et al. (1993). Distinction between mode I and II, II* and IIa as seen in the experiments by Nurick and Shave (1996) were also identified.

By comparison to the limited experimental investigations alluded to above, a large body of analytical studies exist on damage modes for beams and rectangular plates. The rigid-plastic method of analysis is widely accepted and extensively used to study the deformation and damage of beams and plates (Jones, 1971, 1976; Shen and Jones, 1992; Yu and Chen, 1992). For example, the analytical model proposed by Jones (1976) has been shown to predict well the maximum permanent transverse deflection W_0 of a rigid, perfectly-plastic beam. The analytical expression predicting the non-dimensional maximum transverse deflection is given by

$$\frac{W_0}{H} = \frac{1}{4}\left(\sqrt{3\lambda} - 2\right) \tag{1.7}$$

where $\lambda = \rho V_0^2 L^2 / M_0$ is the non-dimensional impulse intensity, ρ is the beam density, L is the half length of the beam, $M_0 = \sigma_Y B H^2/4$ is the fully plastic bending moment and σ_Y is the static yield strength and H is the beam thickness.

Jones (1971) and Yu and Chen (1992) have also provided analytical solutions to predict the maximum permanent transverse deflection of impulsively loaded rectangular plates (fully clamped) with aspect ratio $\gamma \geq 1$. Ignoring membrane effects, Jones (1971) showed that the maximum permanent transverse deflection of a rectangular plate, with length $2a$ and width $2b$ $(a > b)$, subjected to a uniform impulsive velocity V_0 is

$$\frac{W_0}{H} = \frac{(3-\xi_0)[(1+\Gamma)^{\frac{1}{2}} - 1]}{2[1 + (\xi_0 - 1)(\xi_0 - 2)]} \tag{1.8}$$

where $\Gamma = (\lambda/6)(3-2\xi_0)(1/\gamma)^2[1-\xi_0+1/(2-\xi_0)]$ and $\xi_0 = (1/\gamma)[\sqrt{3+(1/\gamma)^2} - (1/\gamma)]$ are both functions of the plate aspect ratio $\gamma = a/b$ and the non-dimensional impulse intensity $\lambda = \rho V_0^2 a^2 / M_0$, where $M_0 = \sigma_Y H^2/4$ is the fully-plastic bending moment per unit length. If, however, W_0 approaches or exceeds the plate thickness H, then membrane force becomes important since it dissipates energy, stiffens the structure and reduces the transverse deflection of the plate significantly. Yu and Chen (1992) accounted for the effects of membrane forces by introducing a kinematically admissible time-dependent velocity field that traces the transient phase of motion of the plates. The temporal evolution of W_0/H was given in the form of

$$\frac{W_0}{H} = \frac{W_0}{H}\left[\lambda\left(=\frac{\rho V_0^2 a^2}{M_0}\right), \gamma\left(=\frac{a}{b}\right)\right] \quad , \quad \gamma \geq 1. \tag{1.9}$$

The ordinary differential equations (ODEs) have to be solved numerically using the fourth order Runge-Kutta method.

The minimum impulsive velocities needed to initiate tensile tearing and pure shear failures at the supports are often defined as critical impulsive velocities corresponding to mode I→II and mode II→III transitions, respectively. Several analytical models exist which predict the critical impulsive velocities corresponding to the transitions between deformation modes. Jones (1976) used an elementary failure criterion (critical tensile strain criterion/critical accumulative shear sliding criterion) to estimate the critical velocities corresponding to mode I→II and II→III transitions for the dynamically loaded beam experiments by Menkes and Opat (1973) which are expressed as

$$\epsilon_{\mathrm{max}} = \epsilon_{\mathrm{c}} \quad \text{mode II} \tag{1.10}$$

$$\Delta^s_{\mathrm{max}} = H \quad \text{mode III} \tag{1.11}$$

where ϵ_{max} (sum of bending ϵ_b and membrane ϵ_m strains) is the maximum total in-plane strain within the structure, ϵ_{c} is the critical tensile strain of the material and Δ^s_{max} is the maximum plastic shear displacement. In a rigid-plastic analyses, deformation is localised at the plastic hinges so the strain distribution in a structure cannot be obtained directly (Jones, 1989). To calculate the maximum total in-plane strain in Eq. 1.10, an effective length for the plastic hinge l has to be defined. Jones (1976) assumed a value of $l = H$ for the initial stage of deformation which becomes $l = L/2$ when the fully plastic membrane force $N = N_0$ is reached. The critical impulsive velocities corresponding to the mode I→II and II→III transitions are, respectively, given by (Jones, 1976)

$$V_{\mathrm{c2}} = \sqrt{\frac{\sigma_Y}{3\rho}}\frac{H}{L}\left(1 + \sqrt{4 + \epsilon_{\mathrm{c}}\frac{8L^2}{H^2} - \frac{2L}{H}}\right) \tag{1.12}$$

and

$$V_{\mathrm{c3}} = \frac{2\sqrt{2}}{3}\sqrt{\frac{\sigma_Y}{\rho}}. \tag{1.13}$$

Thus for a given material, the critical impulsive velocity corresponding to mode I→II transition depends on the ratio L/H. By contrast, the critical velocity at the mode II→III transition depends only on the material properties. Two important effects, however, were ignored by Jones (1976): first, on the interaction between shear force and bending moment and, second, on weakening of the sliding sections with damage progression. Focusing on these two effects, Yu and Chen (2000) re-examined the critical velocity for mode II→III transition. They, too, found that the critical impulsive velocity depends only on material properties given by

$$V_{c3} = \lambda_c \sqrt{\sigma_Y / \rho} \tag{1.14}$$

where λ_c - given in Table 1.1 - depends on the yield criterion adopted. Although Jones (1976)'s prediction of V_{c3} agrees reasonably well with the experiments of Menkes and Opat (1973), Yu and Chen (2000) showed that more accurate predictions are achieved with an interactive yield criterion; for example, circular yield criterion, Hodge's yield criterion, etc.

Table 1.1: Tabulation of critical impulsive parameter λ_c and energy ratio β_c for aluminium beams in Eq. 1.15 (Yu and Chen, 2000).

Criterion	Critical impulsive parameter λ_c	Critical energy ratio β_c
Square yield criterion	0.943	0.857
Circular yield criterion	0.840	0.444
Hodge's yield criterion	0.873	0.438

Shen and Jones (1992) developed an energy-based failure criterion to account for the simultaneous influence of bending, membrane stretch and transverse shear. It states that damage in mode II or III occurs when the specific energy dissipation (density of plastic work) θ at any point in the structure reaches a critical value given by

$$\theta_c = \int_0^{\epsilon_r} \sigma_d \mathrm{d}\epsilon \tag{1.15}$$

where ϵ_r and σ_d are the true rupture strain and the true dynamic stress from a uniaxial tensile test, respectively, which they assumed are equal to the equivalent strain and stress in the actual structure. They found that the transition from mode II to III occurs when the ratio of the plastic work absorbed through shearing deformation to the total plastic work done by all the stress components (β) reaches a critical value of

$$\beta_c = 0.45 \tag{1.16}$$

and the failure criteria that delineate the different damage modes, identified previously by Menkes and Opat (1973), may then be expressed as follows:

$$\text{mode I}: \quad \theta < \theta_c, \quad \beta < \beta_c \tag{1.17a}$$

$$\text{mode II}: \quad \theta = \theta_c, \quad \beta < \beta_c \tag{1.17b}$$

$$\text{mode III}: \quad \theta = \theta_c, \quad \beta \geq \beta_c. \tag{1.17c}$$

Calibrating to the experimental data of Menkes and Opat (1973), Shen and Jones (1992) proposed an empirical relationship between the plastic hinge length and the dissipated energy ratio given by

$$\alpha + 1.2\beta = 1.3 \tag{1.18}$$

where $\alpha = l/H$. Since $0 \leq \beta \leq 1$, it follows that $0.1 \leq \alpha \leq 1.3$. Shen and Jones (1992) found that the onset of mode III damage occurs at a critical value of $\beta_c = 0.45$. The efficacy of this value was assessed for aluminium beams by Yu and Chen (2000) using different forms of interactive yield criteria in Table 1.1. It was found that β_c is close to 0.45 if using an interactive yield criterion, but is nearly twice that deduced by Shen and Jones (1992) for a square yield condition. The predictions using an energy density criterion fits the experimental data by Menkes and Opat (1973) best.

To the best of the author's knowledge, there are currently no analytical predictions on the modes I→II and II→III transitional velocities for impulsively-loaded rectangular plates. However, the open literature did contain a number of detailed 3D finite element (FE) simulations of clamped rectangular plates subjected to impulsive loading where predictions were shown to be in reasonably good agreement with the corresponding experiments. For example, Olson et al. (1993) developed a finite element program (NAPSSE) using on a strain-based criterion, akin to Jones (1976)' critical tensile strain criterion in Eq. 1.10, to simulate mode II damage. However, mode III damage was not included. Gupta et al. (2010) adopted an equivalent strain criterion to model tensile tearing in fully clamped circular mild steel plates. A progressive degradation scheme - also known as an 'element-kill method' in ABAQUS/Explicit (2012) - was employed to model tear initiation, crack propagation and the subsequent complete detachment from its supports. Their FE model assumes that the plate material is bilinear with isotropic hardening - see schematic in Fig 1.4 - and incorporates a Mises yield criterion with associated flow rule. The solid line in the figure - $\bar{\epsilon}_D^p$ and $\bar{\epsilon}_f^p$ are, respectively, the equivalent plastic strain corresponding to the onset of damage and failure - represents the damaged stress-strain response whilst the dashed curve is the response in the absence of damage. The damage variable, D, captures the combined effect of all active damage mechanisms. Gupta et al. (2010) adopted a shear strain criterion in ABAQUS to model the onset of damage for a fully clamped circular mild steel plate due to shear band localisation. Their model assumes that the equivalent plastic strain at the onset of damage ($\bar{\epsilon}_S^p$) is a function of the shear stress ratio and strain rate given by $\bar{\epsilon}_S^p(\theta_s, \dot{\bar{\epsilon}}^p)$ where $\theta_s = (q + k_s p)/\tau_{\max}$ is the shear stress ratio, $\tau_{\max}$ is the maximum shear stress and k_s (= 0.3 for aluminium) is a material parameter. The criterion for damage initiation is met when

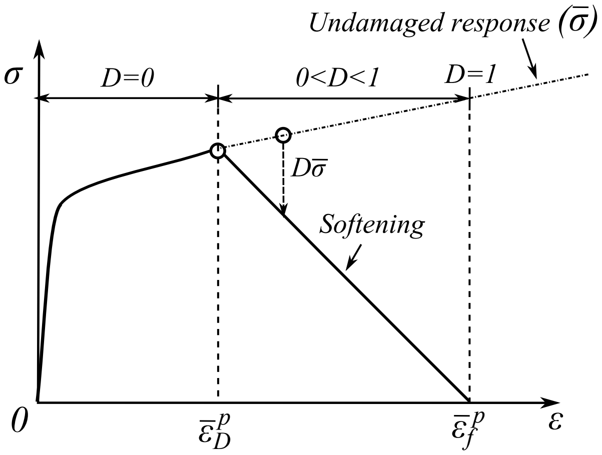

Figure 1.4: Schematic of stress-strain curve with progressive damage degradation.

$$\omega_S = \int \frac{\mathrm{d}\bar{\epsilon}^p}{\bar{\epsilon}_S^p(\theta_s, \dot{\bar{\epsilon}}^p)} = 1 \tag{1.19}$$

where ω_S is a state variable that increases monotonically with plastic deformation and is proportional to the incremental change in equivalent plastic strain. The predictions agree well with the experimental results of Gupta et al. (2010). Ramajeyathilagam and Vendhan (2004) compared the critical tensile strain criterion by Olson et al. (1993) to the equivalent strain criterion by Gupta et al. (2010) for fully clamped rectangular plates (with aspect ratio $\gamma > 1$) using the finite element software CSA/GENSA [DYNA3D]. Both strain-based models predict well the experimental results by Ramajeyathilagam and Vendhan (2004). Rudrapatna et al. (1999) also used the NAPSSE program to simulate damage in rectangular mild-steel plates. Their plates are supported by spring elements rather than conventional constraint conditions. Two different failure models based on the stress and strain ratios were incorporated into NAPSSE: a linear interaction criterion (LIC) where the ratios are added directly and a quadratic interaction criterion (QIC) where the ratios are squared before being added. Failure is assumed to occur when the failure function reaches unity, i.e.

$$\text{LIC:} \quad f = \frac{\epsilon_{\text{max}}}{\epsilon_{\text{r}}} + \frac{\tau_{\text{avg}}}{\tau_{\text{ult}}} = 1 \tag{1.20}$$

$$\text{QIC:} \quad f = \left(\frac{\epsilon_{\text{max}}}{\epsilon_{\text{r}}}\right)^2 + \left(\frac{\tau_{\text{avg}}}{\tau_{\text{ult}}}\right)^2 = 1 \tag{1.21}$$

where the maximum total in-plane strain ϵ_{max} is based on Jones (1976)' beam theory, ϵ_{r} is the rupture strain from a uniaxial tensile test, the shear stress τ_{avg} is assumed to be uniformly distributed around the clamped boundary and given by the reaction forces in the springs, and τ_{ult} is the ultimate shear stress. They showed that the QIC is more accurate than the LIC in predicting the experimental results of Nurick and Shave (1996). Rudrapatna et al. (1999) noted that shear damage does not occur exclusively in mode III but also in mode II.

1.2.3 Non-impulsive response of structures

Single-degree-of-freedom (SDOF) representation of a structure has been widely employed to study the dynamic response of structures subjected to non-impulsive loads and in the preliminary blast assessment of structures; see Fallah and Louca (2007), Fischer and Haring (2009), Krauthammer and Altenberg (2000), Li and

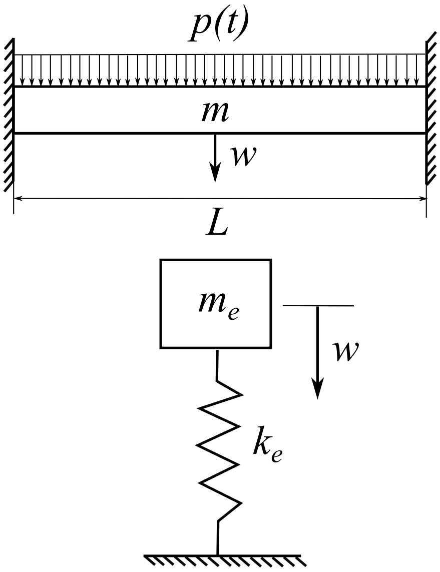

Figure 1.5: Schematic of the transformation of a fully clamped beam system to a SDOF equivalent (Biggs, 1964).

Meng (2002), Rigby et al. (2012, 2014), Subramaniam et al. (2009), Teich and Gebbeken (2010) and Yim and Krauthammer (2009). The parameters of the SDOF model are derived based on energy equivalence with the actual structure. The equation of motion for the SDOF system, shown in Fig 1.5, is given by (Biggs, 1964)

$$m_e\ddot{w} + k_e w = p_e(t) \tag{1.22}$$

where m_e, k_e and p_e are the equivalent mass, stiffness and loading, respectively. Biggs (1964) derived transformation factors (loading factor K_L and mass factor K_M) for the equivalent mass, stiffness and loading as follows:

$$m_e = K_M m_b, \quad k_e = K_L k_b, \quad p_e(t) = K_L p(t) \tag{1.23}$$

where m_b and k_b are the actual mass and stiffness of the beam. The derivation of the transformation factors are based on an assumed shape function $\phi(x)$ for the deformed structure, i.e.

$$K_L = \int \phi(x)\mathrm{d}x \quad \text{and} \quad K_M = \int \phi^2(x)\mathrm{d}x. \tag{1.24}$$

Although Biggs' SDOF method is often employed because of its simplicity and ease of use, with relatively few input requirements, it assumes purely flexural resistance and ignores any membrane action that is induced by large displacement.

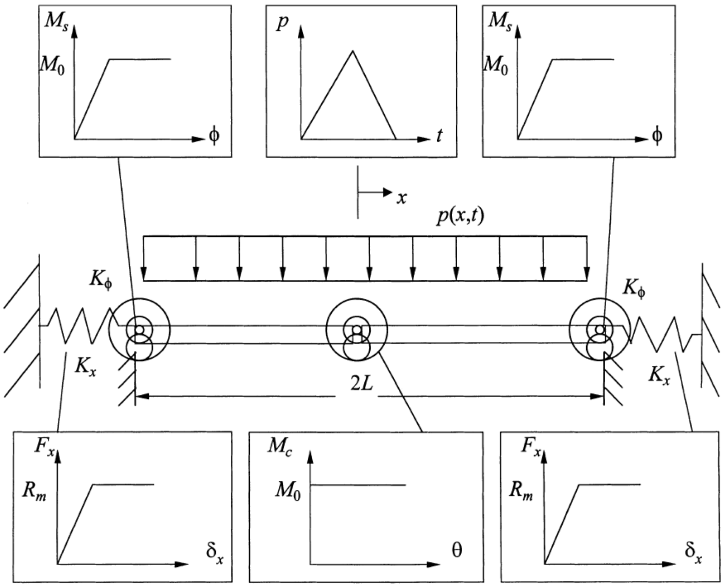

Figure 1.6: Schematic of a structural beam model by Schleyer and Hsu (2000). Finite rotations and elongations are allowed at the supports through the introductions of axial and rotational springs. Resistance-elongation function of axial springs and moment-rotation function at the hinges are as shown.

Modal approximation techniques proposed by Martin and Symonds (1966) were also widely employed to assess the blast response of structures. It assumes that the impulsive response of a rigid-plastic structure results in deformation that continually evolves towards a modal solution, i.e. the velocity field $\dot{W}$ may be written as the product of separate functions of space and time $\dot{W}(x,t)$. The modal solution is a velocity field $\dot{W}(x,t)$ with separated functions for spatial and temporal variables given by

$$\dot{W}(x,t) = \dot{w}(t)\phi(x) \tag{1.25}$$

where $\dot{w}(t)$ is the generalised velocity and $\phi(x)$ is the *mode function* or *mode shape*. The modal solution satisfies the laws of motion, compatibility (kinematic admissibility) and constitutive relations. The corresponding modal displacement (W) and acceleration ($\ddot{W}$) fields can also be written in terms of the same partial functions given by

$$W(x,t) = w(t)\phi(x) \quad \text{and} \quad \ddot{W}(x,t) = \ddot{w}(t)\phi(x). \tag{1.26}$$

The mode approximation methods have been extended to include finite deflections (Symonds, 1980), uncoupled elastic and plastic phases of motion (Symonds and Mosquera, 1985), elastic recovery (Schleyer and Mihsein, 1992) and variable support restraints (Schleyer and Hsu, 2000).

Schleyer and Hsu (2000) used mode approximation technique to investigate the response of beams subjected to non-impulsive loadings. The beam is supported by axial (with stiffness K_x) and rotational springs (with stiffness K_ϕ) at each end as shown in Fig 1.6. The former models purely plastic membrane behaviour whilst the latter models elastic, perfectly plastic characteristics of the supports and plastic hinges. A third rotational spring models a central plastic hinge. In their model the deformation of the structure is divided into three phases in accordance to sequence of plastic hinge formation. The velocity field associated with each phase is linked to the velocity field of the preceding phase using the transitional conditions proposed by Symonds et al. (1984). Their analytical predictions gave excellent agreement with the experimental results by Menkes and Opat (1973). However, their model predictions were limited to the mid-span deflection in mode I and the model neglects the weakening effects of damage and failure.

1.2.4 Effects of fluid-structure interaction

A considerable body of literature exists that deals with the effects of fluid-structure interaction (FSI) in deep underwater explosions and air blasts. The beneficial effects of FSI in reducing the impulse transmitted to a structure have been recognised for deep underwater explosions since Taylor (1941). He modelled the response of a rigid freestanding plate loaded by an exponentially decaying, planar shock wave and showed that the transmitted impulse - in the case of negligible compressibility of the fluid medium - can be expressed as

$$\frac{I^F}{I_i} = 2\beta_w^{-(\beta_w/\beta_w - 1)} \tag{1.27}$$

where I^F is the maximum transmitted impulse per unit area of the free-standing structure, which is governed by a non-dimensional parameter (better known as the FSI index) β_w given by

$$\beta_w = \frac{\rho_w c_w t_i}{\rho H} \tag{1.28}$$

where ρ_w is the density of water and c_w is the wave speed in water. The FSI index β_w is independent of the blast intensity: a direct consequence of the linearity assumption since the reflected pressure profile scales linearly with its corresponding incident values. This 'peculiar' property has been extensively exploited in the design of sandwich panels that can sustain significantly higher impulsive loads than monolithic plates of equivalent weight, leading to greater resistance against underwater blasts: see Fleck and Deshpande (2004), Xue and Hutchinson (2004), Deshpande and Fleck (2005), Tilbrook et al. (2009), McShane et al. (2007), McShane et al. (2010) and Mori et al. (2007), to name a few.

Understanding how cavitation fronts (breaking and closing fronts) develop and evolve is important since the impulse imparted by the blast waves to submerged structures are directly affected by it. Kennard (1943) described theoretically the one-dimensional evolution of cavitation zones in a liquid by treating water as an elastic medium. He found that, when the pressure at any point drops below the cavitation limit of the fluid, two 'breaking fronts' emerge from this and propagate in opposite directions, creating an expanding pool of cavitated liquid. Subsequently, these breaking fronts can arrest, invert their direction of travel and become 'closing fronts' that forces contraction of the cavitated zones.

Schiffer et al. (2012) examined the effects of initial hydrostatic pressure on the underwater blast response of a rigid plate supported by a linear spring. Their model captures propagation of both breaking and closing fronts (Kennard, 1943) as well as their interactions with the structure in a blast event; predictions were shown to be in good agreement with measurements from shock-tube experiments presented by Schiffer and Tagarielli (2013). They found that increasing hydrostatic pressure reduces the transmitted impulse since it moves the point of incipient cavitation away from the structure, and reducing plate mass does not always lead to a reduction in transmitted impulse whilst increasing the supporting stiffness always will.

Analytical and FE models were developed by Schiffer and Tagarielli (2014) to investigate the dynamic response of clamped circular fibre-reinforced composite plate to deep underwater blasts. In their analytical model, the laminated plate is treated as a deformable 2D structure that takes into account the effects of transverse shear, membrane stretch from large deflections, and orthotropic material properties. They found that if an underwater blast loading can be assumed to be impulsive only if the response time of the structure is at least one order of magnitude higher than the decay time of the blast wave. Their predictions were compared to the experiments by Schiffer and Tagarielli (2015) where there is excellent agreement. In addition, Schiffer and Tagarielli (2015) also reported a 'double-cavitation' phenomenon in their experiments. They found that early deformation of the plate, due to the propagation of flexural waves, gives rise to a localised cavitation zone at the fluid-structure interface. This zone quickly collapses upon coalescence of the flexural wave in the centre. Subsequent plate deformation induces an additional cavitation zone at a finite distance from the plate as previously described. It is worth noting that the aforementioned studies were all extensions of Taylor's original theory for an incompressible medium. However, the same approach cannot be employed to study FSI effects in an air blast which involves non-linear, finite amplitude disturbances propagating in a compressible medium (Tan et al., 2005).

Kambouchev et al. (2006, 2007) have extended Taylor's original FSI theory for an incompressible (water) to a compressible (air) medium. They explored analytically the limiting cases of extremely heavy and extremely light plates for arbitrary blast intensities and studied the intermediate asymptotic régimes numerically through a Lagrangian formulation of the Euler equations of compressible flow and conventional shock-capturing techniques. A modified non-dimensional parameter that governs fluid-structure interaction in air - analogous to β_w in Eq.

1.28 - was proposed as follows:

$$\beta_s = \frac{\rho_s U_s t_i}{\rho H}. \tag{1.29}$$

Note that ρ_s is the gas density behind the shock given by

$$\rho_s = \rho_a \frac{2\gamma_a + (\gamma_a + 1)\frac{p_s}{p_a}}{2\gamma_a + (\gamma_a - 1)\frac{p_s}{p_a}}, \tag{1.30}$$

and U_s is the shock speed given by

$$U_s = c_a \sqrt{\frac{(\gamma_a + 1)p_s}{2\gamma_a p_a} + 1}. \tag{1.31}$$

where the subscript a denotes ambient conditions, γ_a is the specific heat ratio, ρ_a is air density, p_a is pressure and c_a is speed of sound in air. The approximate formula for the transmitted impulse can be expressed as a function of this non-dimensional parameter β_s and loading intensity p_s given by

$$\frac{I^F}{I_i} = \lambda_R^{\beta_s(1+\beta_s)} \beta_s^{\beta_s/(1-\beta_s)} \tag{1.32}$$

where the non-dimensional parameter λ_R is

$$\lambda_R = \gamma_R \Big(\frac{C_R f_R}{\gamma_R}\Big), \tag{1.33}$$

the non-dimensional parameter γ_R is

$$\gamma_R = 8 - 42 p_a \frac{\ln(1 + p_s/7p_a)}{p_s}, \tag{1.34}$$

the reflected coefficient C_R is given in Eq 1.5 and f_R is

$$f_R = \Big(6\frac{p_s}{p_a} + 7\Big) \sqrt{\frac{(6 + C_R)\frac{p_s}{p_a} + 7}{\Big(\frac{p_s}{p_a} + 7\Big)\Big((1 + 6C_R)\frac{p_s}{p_a} + 7\Big)\Big(C_R\frac{p_s}{p_a} + 7\Big)}}. \tag{1.35}$$

They found that the transmitted impulse of the free-standing plate reduces with increasing β_s and nonlinear compressibility further enhances the reduction of transmitted impulse provided by FSI effects in the linear range. The beneficial influence of FSI in potentially mitigating the effect of blast has recently been explored as a basis for the design of sandwich structures with increased blast resistance: see Dharmasena et al. (2010, 2011), Ebrahimi and Vaziri (2013), Feng et al. (2007), Main and Gazonas (2008), Vaziri and Hutchinson (2007), Vaziri et al. (2007), Wadley et al. (2010, 2013) and Zhu et al. (2010).

Hutchinson (2009) recently carried out a detailed numerical study to elucidate the effects of non-linear compressibility on the energy and momentum transfer to rigid, free-standing plates subjected to air blasts. In his work, a shock is generated by the sudden release of a highly compressed air layer. The transmitted impulse of the free-standing plate is normalised by the total impulse of the compressed air container I_0 as a function of a non-dimensional parameter β^* given by

$$\beta^* = \frac{1}{2}\frac{I_0^2}{\Delta E_0 \rho H} \tag{1.36}$$

where ΔE_0 is the total energy of the compressed air container. Note that Eq. 1.36 has been defined using invariants of the incident wave compared with β_s, in Eq. 1.29, which must be determined at the instant when the wave strikes a plate. It was found that the impulse transmitted to a plate reduces with increasing β^*. Using this newly-defined non-dimensional variable, it was shown that the maximum impulse transmitted to a plate is around twice the initial total impulse I_0 and this ratio of the maximum transmitted impulse to the initial total impulse I_0 is independent of the loading intensity.

The findings by Kambouchev et al. (2006, 2007) and Hutchinson (2009) apply only to rigid, free-standing plates. Little is known, however, of how the inclusion of supports affect FSI, the momentum and energy transfer, and subsequent failure of a structural component. There are a few recent studies attempting to investigate the effects of FSI for a fully clamped structures. For example, Teich and Gebbeken (2013) investigated the influence of FSI and aerodynamic damping on elastic response of a structure subjected to an air blast. They extended Taylor's model to include aerodynamic damping, stiffness effects and structural damping and developed closed-form solutions to the problem by assuming a linear

FSI effect, i.e. no change in the fluid density and linear superposition of waves. They found that the general assumption of rigid reflection (ignoring FSI effect) leads to a significant overestimation of displacements and thus the internal forces and stresses in flexible systems subjected to blast loadings. Subramaniam et al. (2009) studied interactions between a blast pressure wave and an elastic structure numerically using an Arbitrary Lagrange Euler (ALE) framework. They found that the structural displacement predicted by ignoring FSI is larger than the corresponding displacement considering FSI - this is consistent with the findings of Teich and Gebbeken (2013). The error in the predicted maximum displacement by ignoring FSI effect was found to be directly proportional to the ratio of the velocity of the structure to the velocity of the shock wave.

1.3 Motivations and objectives

Existing models (based on either rigid-plastic methods, single-degree-of-freedom model, or modal approximation techniques) are not applicable when estimating the dynamic response (deformation, damage and failure) of elasto-plastic structures subjected to intense non-impulsive loadings. It is also unclear how pulse shape, and its corresponding duration, influence the mode of damage, and how limits to deformation due to necking localisation and/or ductile fracture at the supports affect the final performance of the structure, with or without fluid-structure interactions. There lacks a general methodology, through an analytical approach or otherwise, to capture large elasto-plastic deformation, and the loss of integrity at the supports for general (impulsive and non-impulsive) loadings.

The current state of knowledge on fluid-structure interactions involving monolithic structures, in both compressible or incompressible medium, is still very much grounded on works based on a rigid free-standing structure (Taylor, 1941; Kambouchev et al., 2006, 2007; Hutchinson, 2009), or an elastic structure (Schiffer et al., 2012; Schiffer and Tagarielli, 2014, Subramaniam et al., 2009, Teich and Gebbeken, 2011). The magnitude of loading from a blast is often sufficiently intense to cause significant plastic deformation in a structure, leading to large deformation and, in extreme cases, to a loss of integrity at the supports. It is as yet unclear how the introduction of supports to a ‘free-standing structure’, and/or the methodology needed to introduce them, affects previously known results. Likewise, on the relaxation of an idealised rigid structure to an elasto-plastic one.

The main objectives of this PhD work are to develop models, both numerical and analytical, to elucidate the following for elasto-plastic structures subjected to general (impulsive and non-impulsive) loadings:

1. To understand how pulse shape and duration affect structural deformation and the critical impulse at mode transitions;
2. The interplay between bending, shear and membrane effects on structural deformation and failure;
3. To quantify how FSI affects energy and momentum transfer during large structural deformation and its subsequent failure; and,
4. On the roles of the fixing condition offered by the supports during FSI.

1.4 Outline of the thesis

This thesis is organised as follows. Chapter 2 develops a model for an elasto-plastic structural beam system that is sufficiently general to capture large elasto-plastic deformation with bending, shear and catenary action, and the loss of integrity at the supports. In Chapter 3, three-dimensional (3D) finite element (FE) models for elasto-plastic beams are developed to simulate its response to blast loadings. Both the FE (Chapter 3) and analytical (from Chapter 2) models - validated against the experimental data of Menkes and Opat (1973) - are used to investigate the effects of pulse duration on the deformation and failure of fully clamped deformable beams. Chapter 4 investigates the effects of FSI in deep underwater explosions for the elasto-plastic structural beam system developed in Chapter 2. Predictions from the previously validated 3D FE models will be used to validate the analytical predictions where they will be shown to be in excellent agreement. The analytical model is then used to carry out parametric studies to investigate the sensitivity of energy and impulse transfer to deformable beams of different mass and aspect ratio. How support conditions affect previously known results based on rigid, free-standing structures are investigated here. Chapter 5 presents results on FSI between an intense air blast (considering the non-linear compressibility of air) and the elasto-plastic structural beam system from Chapter 2. The effects of structural and blast pressure wave parameters on FSI are investigated. The sensitivity of blast response of a deformable beam to its aspect ratio and mass will be quantified. Similar to Chapter 4, the influence of support conditions is also investigated. Chapter 6 deals with the blast response of fully clamped rectangular plates. 3D FE models are developed which are validated against experimental data for square mild-steel and aluminium plates from the literature. Deformation contour maps delineating régimes of deformation modes for combinations of aspect ratio and non-dimensional impulse are produced. Finally, in Chapter 7, conclusions and suggestions for further research are given.

1.5 Contributions to existing literature

The bulk of the research work reported in this thesis have appeared in archival journals, submitted for review or currently under preparation. They are as follows:

1. "Deformation and failure of rectangular plates subjected to impulsive loadings" (Yuan, Y., and Tan, P. J.), *International Journal of Impact Engineering* 59 (2013), 46-59.
2. "Energy and momentum transfer to a 'fully clamped' elastic plate in an air-blast" (Yuan, Y., and Tan, P. J.), *Applied Mechanics and Materials* 566 (2014), 262-267.
3. "Large deformation, damage evolution and failure of ductile structures to pulse-pressure loading" (Yuan, Y., Tan, P. J., Shojaei, A., and Wrobel, P.), submitted to *International Journal of Solids and Structures*, (2015).
4. "The influence of deformation limits on fluid-structure interactions in deep underwater blasts" (Yuan, Y., Tan, P. J., Shojaei, A., and Wrobel, P.), submitted to *International Journal of Impact Engineering*, (2015).

5. “Elastic-plastic response spectra with fluid-structure interaction effect” (Yuan, Y., Tan, P. J., Shojaei, A., and Wrobel, P.), submitted to *Archive of Applied Mechanics*, (2015).
6. “Preliminary assessment of the design guidelines for ships against blast loadings” (Liu, L., Tan, P. J., Yuan, Y., and Wrobel, P.), in preparation for *Ocean Engineering*, (2015).

Chapter 2

Formulation of an elasto-plastic structural beam system

As reviewed in Section. 1.2.2, Menkes and Opat (1973) identified three distinct damage modes that are characteristics of clamped ductile beams subjected to short-duration, high-intensity transverse pressures (referred to, hereinafter, as impulsive loadings): viz. mode I - large inelastic deformation; mode II - tensile tearing over the supports; mode III - transverse shear failure at the supports. Of noteworthy is that damage in mode II and III always initiates in the region of the beam abutting the supports although, in practice, a sharp distinction between the two modes is not found. There are several analytical models - Jones (1976), Yu and Chen (2000), Shen and Jones (1992), Wen (1996) and Alves and Jones (2002a,b) to name a few - on the prediction of critical impulse at mode transitions. However, nearly all were formulated within the constitutive framework of limit analysis and assumed impulsive loading conditions. The model by Jones (1976) proposed that the critical impulsive velocity at mode I→II transition occurs when the maximum in-plane strain - arising from catenary (membrane) and bending actions - over the supports reaches the critical tensile strain of the material from which the beam was made; and when the maximum transverse shear sliding at the supports reaches the beam thickness for the corresponding mode III damage. In reality, however, membrane force must play a significant role during failure in mode III and, likewise, with transverse shear force in mode II. To address this, Shen and Jones (1992) developed an energy-based failure criterion - applicable to a broad class of dynamic structural problems - to account for the simultaneous influence of bending, membrane stretch and transverse shear. It states that damage (mode II or III) occurs when the specific dissipation (density of plastic work) θ at a point in the structure reaches a critical value of $\theta_c = \int_0^{\epsilon_r} \sigma_d \mathrm{d}\epsilon$ where ϵ_r and σ_d are the true rupture strain and the true dynamic stress of a uniaxial tensile test, respectively, which they assumed are equal to the equivalent strain and stress in the actual structure. They found that a transition occurs from mode II to III at the critical value of $\beta_c = 0.45$, where β is the ratio of the plastic work absorbed through shearing deformation to the total plastic work done by all the stress components. Yu and Chen (2000) studied transverse plastic shear failure at the supports (mode III) where the efficacy of $\beta_c = 0.45$, previously proposed by Shen and Jones (1992), was assessed against different forms of interaction yield criteria; furthermore, the weakening effects of the sliding sections - a transverse-displacement discontinuity - during the failing process is also included in their model. Whilst the aforementioned models are able to predict critical impulses that are broadly in agreement with the experimental data of Menkes and Opat (1973), they are limited to impulsive loadings and neglects elastic deformation in the beam.

In order to model the effects of boundary conditions (or supports) upon the momentum and energy transfer to a deformable structure through fluid structure interaction (FSI) - this is to be presented in Chapters 4 and 5 - certain restrictions and assumptions in existing analytical models will need to be relaxed/removed. This chapter presents the formulation of a more general elasto-plastic structural beam system aimed specifically at addressing the aforementioned. The proposed structural model is sufficiently general to (1) describe large elasto-plastic deformation with catenary actions; (2) incorporate the interactions between bending, membrane stretch and transverse shear in the yield and plastic limit functions; (3) model the loss of integrity at the supports through progressive damage and its subsequent detachment; and, (4) account for general (impulsive and non-impulsive) loading conditions. For the sake of definiteness, *damage* shall refer to the onset and subsequent degradation of the generalised stresses in the beam member and at its supports; as opposed to *failure* which refers to a complete loss of load carrying capacity of the beam member, exemplified by the complete detachment of the beam from its supports. Predictions by the present model will be compared to existing experimental data from the literature, and to results from detailed three-dimensional finite-element simulations in Chapter 3, where they will be shown to be in good agreement.

2.1 Features of the structural beam system

Figure 2.1 shows a schematic representation of a structural beam system which consists of a beam member supported at each end by three springs (one rotational and two axials). The beam member - made of a rate-independent, elastic perfectly-plastic material in the present study - is of total length $2L$ and a uniform rectangular cross-section of thickness H and width B where $L/H \gg 1$ (i.e. the beam is slender). Following Schleyer and Hsu (2000), a pressure loading $p(x,t)$ is assumed to always impinge normally over the entire span of the beam regardless of its subsequent transverse deflection. For uniformly distributed pressure loading, $p(x,t) = p(t)$. The pressure pulse may take on any general form: exponentially decaying (EXP), linearly decaying (LIN), rectangular (REC) etc.

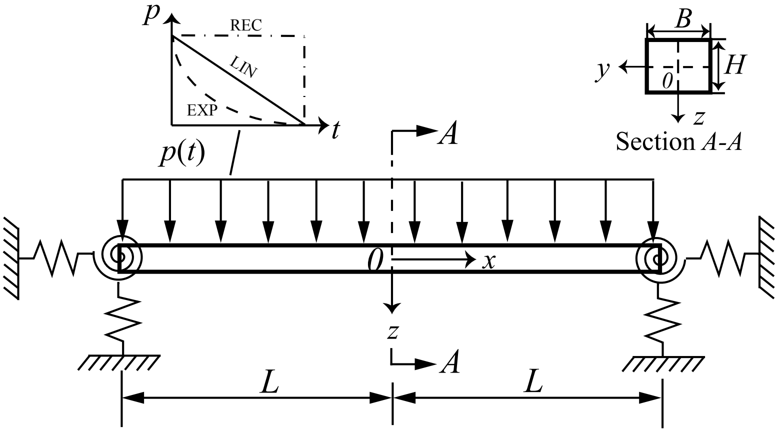

Figure 2.1: Schematic of a structural beam system. A plane of symmetry exists along $x = 0$, $-B/2 \leq y \leq B/2$, $-H/2 \leq z \leq H/2$ so that only the right-half needs to be modelled.

The rotational spring has elasto-plastic characteristics to model the beam rotation at each end and the subsequent plastic hinge formation. Both the axial and vertical springs have rigid-plastic characteristics to model the 'plastic stretch' and 'plastic shear sliding' actions at the supports, respectively. Collectively, the trio of springs may be regarded as a representation of an imperfectly clamped boundary which allows interactions between bending, stretch and shear to be considered and where damage mechanics will be applied to model the progressive loss of support integrity. Experiments and theoretical studies (Menkes and Opat, 1973; Shen and Jones, 1992; Wen, 1996) have all shown that damage (mode II and III) in impulsively loaded beams occurs in the region abutting the supports. In the case of non-impulsive loading, the present model, too, assumes that failure occurs in the same region of the beam member. Detailed three-dimensional finite-element simulations, to be presented in Chapter 3, will show that this is a valid assumption and is, indeed, the case. A plane of geometric and loading symmetry exists at the mid-span of the beam ($x = 0$) which allows one-half of the beam to be analysed.

2.2 Yield, damage and failure criteria

The components of stress σ on any cross-section of the beam member, including at its supports, give the following stress resultants for axial force N, shear force Q, axial torque T and bending moment M (Stronge and Yu, 1993):

$$N = \int_A \sigma_{xx} \mathrm{d}A, \quad Q = \int_A \sigma_{xz} \mathrm{d}A, \quad T = \int_A (y\sigma_{xz} - z\sigma_{xy}) \mathrm{d}A, \quad M = -\int_A z\sigma_{xx} \mathrm{d}A \tag{2.1}$$

where A is the cross-sectional area of the beam; y and z are transverse coordinates measured from the axis through the centroid of every section. Since the beam is loaded by equal but opposing couples that act in directions perpendicular to the plane of symmetry, the beam must bend in the plane of symmetry and does not twist, i.e. $T = 0$. For slender beam members where $L/H \gg 1$, stress resultants arising from the actions of membrane N, shear Q and bending M are analogous to stress components in a continuum and are referred, hereinafter, as generalised stresses (Stronge and Yu, 1993; Jones, 1990; Shen and Jones, 1992). Yield, damage and failure criteria will be presented as functions of these generalised stresses in the following sub-sections.

2.2.1 Yield and fully plastic stress state

The state of stress on any cross-section of an elastic perfectly-plastic beam member, including at its supports, is established through functions of yield (ψ^{el}) and fully plastic (ψ^{p}) stress conditions as follows: (Stronge and Yu, 1993)

$$\text{Elastic state}: \quad \psi^{el} < 0 \tag{2.2a}$$

$$\text{Elasto-plastic state}: \quad \psi^{el} > 0, \quad \psi^{p} < 0 \tag{2.2b}$$

$$\text{Fully plastic state}: \quad \psi^{el} > 0, \quad \psi^{p} = 0. \tag{2.2c}$$

Since every cross-section carries shear force, in addition to axial force and bending moment, the yield function ψ^{el} is given by (Stronge and Yu, 1993)

$$\psi^{el} = \frac{|M|}{M_Y}\sqrt{1 - \frac{Q^2}{Q_Y^2}} + \frac{N}{N_Y} + \frac{Q}{Q_Y} - 1 \tag{2.3}$$

where $M_Y = \sigma_Y BH^2/6$, $N_Y = \sigma_Y BH$ and $Q_Y = 2\sigma_Y BH/3\sqrt{3}$ are the bending moment, membrane force and transverse shear force at the elastic limit, respectively. The yield condition $\psi^{el} = 0$ provides an upper bound on the generalised stresses correponding to elastic (reversible) strains at every point in the cross-section.

When part of the cross-section is strained beyond its elastic limit (i.e. $\psi^{el} > 0$), proportional increases in the stress resultants will lead to an increase in ψ^{el} with deformation. The increases in stress asymptotically approach a limiting, or fully plastic, stress condition $\psi^{p} = 0$ as the curvature and deformation becomes indefinitely large. For solid cross-sections, the distribution of each stress components in the plastically deforming region of the cross-section can conceivably change with deformation. Following Stronge and Yu (1993), these changes are also ignored here. The fully plastic limit function ψ^{p} for generalised stresses in a rectangular cross-section is given by (Stronge and Yu, 1993)

$$\psi^p = \frac{|M|}{M_0}\sqrt{1 - \frac{Q^2}{Q_0^2}} + \frac{N^2}{N_0^2} + \frac{Q}{Q_0} - 1 \tag{2.4}$$

where $M_0 = \phi_m M_Y$, $N_0 = N_Y$ and $Q_0 = \phi_m Q_Y$ are the fully plastic bending moment, membrane force and transverse shear force, respectively. ϕ_m is the shape factor defined as the ratio of fully plastic bending moment (or fully plastic transverse shear force) to its corresponding elastic limit and is equal to 1.5 for a beam of rectangular cross-section. It is convenient to express the fully plastic limit function in non-dimensional form as follows:

$$\psi^p = |\bar{M}|\sqrt{1 - \bar{Q}^2} + \bar{N}^2 + \bar{Q}^2 - 1 \tag{2.5}$$

where $\bar{M} = M/M_0$, $\bar{N} = N/N_0$ and $\bar{Q} = Q/Q_0$ are the non-dimensional fully plastic generalised stresses. The fully plastic stress condition $\psi^p = 0$ is an upper bound for stress states that satisfy yield in any part of the cross-section. This bound for the fully plastic state is based on an assumption that the distribution of normal stress in the fully plastic stress state with, or without, shear is identical (Stronge and Yu, 1993). Plastic hinge forms at the cross section where the fully plastic stress condition $\psi^p = 0$ is reached.

2.2.2 Damage initiation and evolution

The term *damage* describes the onset and subsequent degradation of the generalised stresses in the beam member and at its supports. Figure 2.2 shows a schematic of generalised stresses ($\bar{M}$ or $\bar{N}$ or $\bar{Q}$) versus effective strain ϵ_{eff} where point c corresponds to the generalised stress state at which a cross-section meets the damage initiation criterion ($\omega_d = 1$). Upon damage initiation, the generalised stresses degrade in accordance to an evolution law, denoted by the line $c-d$. This section presents the damage initiation criterion and an evolution law that governs the softening of these generalised stresses.

In general, the effective strain ϵ_{eff} on any cross-section may be expressed as

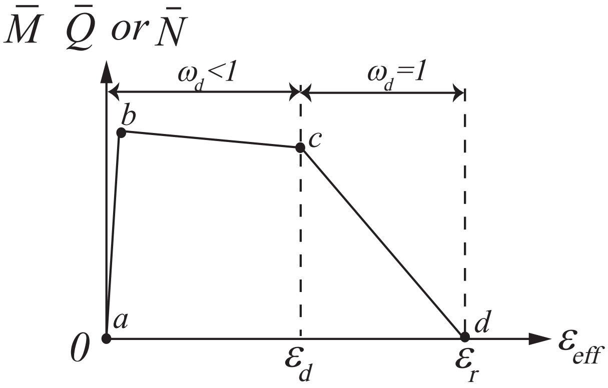

Figure 2.2: Schematic showing non-dimensional generalised stresses as a function of effective strain pre- ($\omega_d < 1$) and post- ($\omega_d = 1$) damage initiation.

(Wen, 1996; Alves and Jones, 2002a)

$$\epsilon_{\text{eff}} = \sqrt{\frac{2}{9}\Big[(\epsilon_{xx}-\epsilon_{yy})^2 + (\epsilon_{yy}-\epsilon_{zz})^2 + (\epsilon_{xx}-\epsilon_{zz})^2 + \frac{3}{2}(\gamma_{xz}^2 + \gamma_{zy}^2 + \gamma_{xy}^2)\Big]}. \quad (2.6)$$

For slender members, out-of-plane warping of cross-sections is negligible since the depth is small compared to its length; consequently, plane sections remain plane (Stronge and Yu, 1993). Therefore, it is reasonable to assume that $\gamma_{xy} = \gamma_{yz} = 0$ (Wen, 1996; Alves and Jones, 2002a). If the material in a dynamic uniaxial test with $\epsilon_{xx} > 0$ obeys the incompressibility relation $\epsilon_{xx} + \epsilon_{yy} + \epsilon_{zz} = 0$, then $\epsilon_{yy} = \epsilon_{zz} = -\epsilon_{xx}/2$ (Jones, 1989). Hence, Eq. 2.6 reduces to

$$\epsilon_{\text{eff}} = \sqrt{\epsilon_{xx}^2 + \frac{1}{3}\gamma_{xz}^2}. \quad (2.7)$$

The maximum total strain ϵ_{xx} experienced at any cross-section x comprises of two parts given by (Wen, 1996; Jones, 1989)

$$\epsilon_{xx} = \epsilon_m + \epsilon_b \quad (2.8)$$

where the membrane strain ϵ_m and bending strain ϵ_b may be expressed, respectively, as functions of the transverse mid-span displacement of the beam W_B as follows:

$$\epsilon_m = 2\Big(\frac{W_B}{L}\Big)^2\Big(\frac{x}{L}\Big)^2 \quad (2.9)$$

and

$$\epsilon_b = \frac{W_B H}{L^2}. \tag{2.10}$$

Note that a linear variation of the membrane strain ϵ_m has been assumed across the beam length (Jones, 1989).

Following Wen (1996), Alves and Jones (2002a), Yu and Chen (2000) and Jones (1976), it is further assumed that the transverse shear strain γ_{xz} is negligible within the beam member but is dependent upon the plastic shear sliding distance over the shear band at the supports. Hence, on any cross-section

$$\gamma_{xz} = \begin{cases} 0 & \text{if } 0 \leq x < L \\ W_S/(l/2) & \text{if } x = L \end{cases} \tag{2.11}$$

where W_S is the plastic shear sliding displacement and l is the width of the shear band. Slip-line field analysis of a rigid-plastic beam with rectangular cross-section and thickness H by Nonaka (1967) have shown that the shear band width ranges between $H \leq l \leq 2H$ for maximum transverse beam deflection of 0 to H. The latter corresponds to the onset of membrane response in the beam. Since large beam deflection invariably leads to membrane stretching, a value of $l = 2H$ is chosen following Jones (1976) and Nurick and Shave (1996). Substituting Eqs. 2.8 - 2.11 into Eq. 2.7, gives an approximate expression for the effective strain on any cross-section x of the beam system as follows:

$$\epsilon_{\text{eff}} = \begin{cases} 2\left(\frac{W_B}{L}\right)^2\left(\frac{x}{L}\right)^2 + \left(\frac{W_B H}{L^2}\right) & \text{if } 0 \leq x < L \\ \sqrt{\left[2\left(\frac{W_B}{L}\right)^2 + \left(\frac{W_B}{L}\right)\left(\frac{H}{L}\right)\right]^2 + \frac{1}{3}\left(\frac{W_S}{H}\right)^2} & \text{if } x = L \end{cases} \tag{2.12}$$

It is noted that the effective strain is greatest at the supports where $x = L$ since its two constituent components (total axial in-plane and transverse shear strains) are both highest there. This is in agreement with Wen (1996) and Alves and Jones (2002a). Expressions for W_B and W_S are to be derived in Section 1.3.

The criterion for damage initiation is met when (ABAQUS/Explicit, 2012)

$$\omega_d = \frac{\epsilon_{\text{eff}}}{\epsilon_d} = 1 \tag{2.13}$$

where ω_d is a state variable that increases monotonically with effective strain ϵ_{eff} and ϵ_d is the effective strain at the onset of damage. Upon the initiation of damage, i.e. $\omega_d = 1$, progressive softening of the non-dimensional generalised stresses follows

$$|\bar{M}| = |\bar{M}^f|(1-D), \quad \bar{N} = \bar{N}^f(1-D) \quad \text{and} \quad \bar{Q} = \bar{Q}^f(1-D) \tag{2.14}$$

where D is the damage variable; $\bar{M}^f$, $\bar{N}^f$ and $\bar{Q}^f$ are the non-dimensional bending moment, membrane force and transverse shear force at the onset of damage, respectively. For the sake of simplicity, a linear evolution of the damage variable D with effective strain ϵ_{eff} is adopted here as follows: (ABAQUS/Explicit, 2012)

$$D = \frac{\epsilon_{\text{eff}} - \epsilon_d}{\epsilon_r - \epsilon_d} \tag{2.15}$$

where ϵ_r is the rupture strain in a uniaxial tensile test. This definition ensures that when $D = 1$, generalised stresses decreases to zero.

2.2.3 Failure criteria

Failure refers to a complete loss of load carrying capacity by the beam member through detachment from its supports. Experiments by Menkes and Opat (1973) have shown that an impulsively loaded beam always fails at its supports for modes II and III; this is also in agreement with predictions by the analytical models of Wen (1996) and Alves and Jones (2002a). Here, Eq. 2.12 too shows that ϵ_{eff} is greatest at the supports ($x = L$) where damage is expected to initiate and evolve. Therefore, failure criteria need only be established for the supports in Fig 2.1.

The criteria delineating the different modes of failure, described by Menkes and Opat (1973), are as follows:

$$\text{Mode I}: \quad D < 1, \quad \omega_s < 1 \tag{2.16a}$$

$$\text{Mode II}: \quad D = 1, \quad \omega_s < 1 \tag{2.16b}$$

$$\text{Mode III}: \quad D = 1, \quad \omega_s \geq 1 \tag{2.16c}$$

The state variable ω_s is expressed as

$$\omega_s = \frac{\beta}{\beta_c} = 1, \tag{2.17}$$

where β is the ratio of the plastic work absorbed through shearing deformation to the total plastic work done by all the stress components given by (Shen and Jones, 1992)

$$\beta = \frac{E_S^s}{E_S^s + E_S^b + E_S^m} \tag{2.18}$$

where E_S^s is the shear strain energy obtained via the vertical axial spring; E_S^b is the bending strain energy of the rotational spring; E_S^m is the membrane strain energy obtained via the horizontal axial spring; and, β_c is the critical β value marking the transition from mode II to III. For aluminium beams, Yu and Chen (2000) showed that the β_c obtained using a square yield criterion is larger than 0.45 obtained by Shen and Jones (1992) with an interactive yield criterion. Furthermore, they found that β_c is a material-dependent parameter which is independent of geometry. Since an interactive fully plastic limit function is used here and material properties corresponding to Aluminium 6061-T6 - the same as Shen and Jones (1992) and Yu and Chen (2000) - is used in the simulations to be presented in Chapters 3 to 5, it is reasonable to assume that $\beta_c = 0.45$.

2.3 Equations of motion

The overall transverse displacement at any point x ($x > 0$) of the structural beam system may be approximated as a sum of n generalised displacements and mode functions given by (Williams, 1996)

$$W(x,t) = \sum_{i=1}^{n} \phi_i(x) w_i(t) \tag{2.19}$$

where the partial functions $\phi_i(x)$ are admissible mode functions that satisfy the geometric boundary conditions and the temporal functions $w_i(t)$ are generalised transverse displacements to be determined by the Lagrange equations of the 2nd kind. Since the transverse displacement will be represented here by the sum of polynomials, instead of the normal modes of transverse vibration in a beam system, the partial functions $\phi_i(x)$ need not be orthogonal (Williams, 1996). According to Eq. 2.19, the displacement at the mid-span and supports are given, respectively, by

$$W_B(t) = W(x=0,t) \quad \text{and} \quad W_S(t) = W(x=L,t). \tag{2.20}$$

The corresponding velocity ($\dot{W}$) and acceleration ($\ddot{W}$) fields also use the same partial functions given by

$$\dot{W}(x,t) = \sum_{i=1}^{n} \phi_i(x)\dot{w}_i(t) \quad \text{and} \quad \ddot{W}(x,t) = \sum_{i=1}^{n} \phi_i(x)\ddot{w}_i(t). \tag{2.21}$$

Defining the generalised mass of the beam member as

$$M_{ij} = \begin{cases} m\int_0^L \phi_i(x)\phi_j(x)\mathrm{d}x & \text{if } i \neq j \\ m\int_0^L \phi_i^2(x)\mathrm{d}x & \text{if } i = j \end{cases} \tag{2.22}$$

where m is the mass per unit length, the total kinetic energy of the beam system at any given time t can be expressed as

$$E_K = \frac{1}{2}m\int_0^L \dot{W}^2(x,t)\mathrm{d}x = \frac{1}{2}\sum_{i}^{n}\sum_{j}^{n} M_{ij}\dot{w}_i\dot{w}_j. \tag{2.23}$$

The total potential (strain) energy of the beam system is

$$V = \underbrace{E_S^b + E_S^s + E_S^m}_{\text{support}} + \underbrace{E_B^b + E_B^m}_{\text{beam}} \tag{2.24}$$

where E_B^b and E_B^m are the bending and membrane strain energies of the beam member, respectively; E_S^s, E_S^b and E_S^m are the shear, bending and membrane strain energies associated with the vertical, rotational and axial springs, respectively, at the supports. Note that subscripts S and B are used to denote support and beam member, respectively; whilst, superscripts s, b and m denote shear, bending and membrane, respectively. The generalised force is given by

$$Q_i = \int_0^L p(x,t)\phi_i(x)\mathrm{d}x, \quad i = 1, 2, ..., n. \tag{2.25}$$

Since the *Lagrangian* of the structural beam system is

$$\mathcal{L} = E_K + V, \tag{2.26}$$

the differential equations governing w_i are obtained by substituting Eqs. 2.26 and 2.25 into the well-known Lagrange equation of the 2nd kind

$$\frac{\mathrm{d}}{\mathrm{d}t}\left(\frac{\partial \mathcal{L}}{\partial \dot{w}_i}\right) + \frac{\partial \mathcal{L}}{\partial w_i} = Q_i, \quad i = 1, 2, ..., n \tag{2.27}$$

to give

$$\sum_{j=1}^{n} M_{ij}\ddot{w}_j + \frac{\partial V}{\partial w_i} = \int_0^L p(x,t)\phi_i(x)\mathrm{d}x, \quad i = 1, 2, ..., n. \tag{2.28}$$

The key to obtaining the governing equations of motion in Eq. 2.28 is to derive the various strain energy components (E_S^b, E_S^s, E_S^m, E_B^b and E_B^m) in Eq. 2.24.

Following Schleyer and Hsu (2000) and Biggs (1964), the dynamic response of the beam system is divided into three phases of motion in accordance to the sequence of plastic hinge formation as follows: (1) Phase 1 ($0 < t \leq t_1$) - when the fully plastic stress condition is not met anywhere in the beam, i.e. $\psi^p < 0$; (2) Phase II ($t_1 < t \leq t_2$) - when a stationary plastic hinge forms at the support; (3) Phase III ($t_2 < t \leq t_3$) - when a travelling plastic hinge A develops, moves towards, and coalesce with, the existing stationary hinge at the mid-span of the beam, ending up in a final two-hinge collapse configuration. The strain energy components corresponding to each are derived in the following subsections.

Note that each phase of motion has its own unique set of initial condition and associated displacement (and velocity) field. In the present study, the transitional conditions between phases follow the proposal by Symonds et al. (1984), which is based on the well-known 'minimum Δ_0 technique'. This technique is commonly employed to determine the starting amplitude of the 'new' velocity field by minimising the difference in kinetic energies between the velocity fields at the end of the terminating phase and at the start of the new phase (Schleyer and Hsu, 2000; Langdon and Schleyer, 2005; Stronge and Yu, 1993).

2.3.1 Phase I: $0 < t \leq t_1$

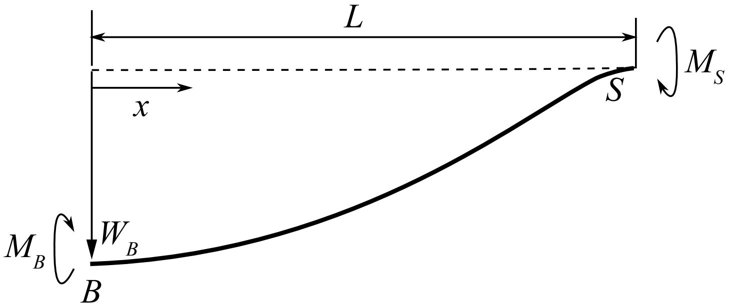

Figure 2.3: Schematic of the transverse displacement for the right-half of the structural beam system in Phase I.

In Phase I, it is reasonable to neglect catenary actions and transverse shear since the transverse deflection is small compared to the beam thickness, i.e. $W_B \ll H$ (Izzuddin, 2005; Schleyer and Hsu, 2000). To simplify the transition from an elasto-plastic to a fully plastic stress state, the true moment-curvature relationship on any cross-section - with its non-linear increase in yield moment M_Y to the fully plastic bending moment M_0 shown schematically in Fig 2.4 - is replaced by a bilinear approximation to simplify the calculations of the bending moment (Jones, 1989; Schleyer and Hsu, 2000; Izzuddin, 2005). Since bending moment is always greatest at either the supports ($x = L$) or the mid-span ($x = 0$) for a transversely-loaded beam, one should expect a plastic hinge to form first at either of these two locations (Biggs, 1964; Schleyer and Hsu, 2000; Izzuddin, 2005, Langdon and Schleyer, 2005). Consequently, fully plastic limit function given by Eq. 2.5 need only be defined at the supports and mid-span of the beam, respectively, as follows:

$$\psi_S^p = |\bar{M}_S| - 1 \tag{2.29}$$

and

$$\psi_B^p = |\bar{M}_B| - 1. \tag{2.30}$$

Phase I motion ends when either $\psi_S^p = 0$ or $\psi_B^p = 0$: whichever is reached first. Notwithstanding, Schleyer and Hsu (2000) and Fallah et al. (2013) have shown that the sequence of hinge formation depends critically upon the non-dimensional parameter $\alpha(= K_\phi L/EI)$, where E is Young's modulus and $I = BH^3/12$ is the beam's second moment of area. Fallah et al. (2013) found that when $\alpha > 6$, a plastic hinge always forms at the supports first. To ensure that the angle between the horizontal and vertical axial springs must always be perpendicular, a relatively large rotational stiffness K_ϕ is used in the present model. Therefore, it is reasonable to assume that a plastic hinge always forms first at the supports since $\alpha \gg 6$.

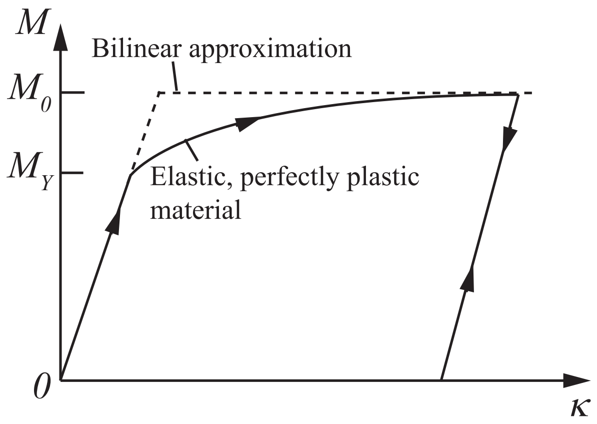

Figure 2.4: Bilinear approximation of the moment-curvature characteristics for an elastic-perfectly plastic beam system with a rectangular cross-section.

Following Schleyer and Hsu (2000), an admissible transverse displacement field for the right-half of the structural beam system in Phase I, shown in Fig 2.3, is given by

$$W(x,t) = \frac{w_1(t)}{2}\left(1 + \cos\frac{\pi x}{L}\right) + w_2(t)\cos\frac{\pi x}{2L}. \tag{2.31}$$

The bending strain energies in the beam member and rotational spring are, respectively,

$$E_B^b(t) = \frac{EI}{2}\int_0^L \left[\frac{\partial^2 W(x,t)}{\partial x^2}\right]^2 \mathrm{d}x \tag{2.32}$$

and

$$E_S^b(t) = \frac{K_\phi}{2}\phi(t)^2 \tag{2.33}$$

where $\phi(t) = \int_0^L [\partial^2 W(x,t)/\partial x^2]\mathrm{d}x$ (Langdon and Schleyer, 2005; Schleyer and Hsu, 2000). Since $W_B \ll H$, it is reasonable to assume that the strain energies due to shear and membrane are negligibly small (Izzuddin, 2005); hence,

$$E_S^s(t) = E_S^m(t) = E_B^m(t) \simeq 0. \tag{2.34}$$

Substituting Eqs. 2.32, 2.33 and 2.34 into Eq. 2.28, and using the initial conditions $w_1 = w_2 = 0$ and $\dot{w}_1 = \dot{w}_2 = 0$ gives the two equations of motion of this phase. When the fully plastic stress condition at the supports is reached, i.e.

$$\psi_S^p = |K_\phi \phi(t)|/M_0 - 1 = 0, \tag{2.35}$$

it marks the end of Phase I deformation with the corresponding time of $t = t_1$.

2.3.2 Phase II: $t_1 < t \leq t_2$

In Phase II, the beam member may be assumed to deform in a manner similar to a simply supported beam, see Biggs (1964). Following Izzuddin (2005), Fallah and Louca (2007) and Fallah et al. (2013), small transverse deflection is also assumed for Phase II; hence, the influence of transverse shear and catenary actions can be ignored. Therefore, the fully plastic stress condition at the supports - since $\psi_S^p = 0$ - reduces to

$$|\bar{M}_S| = 1 \tag{2.36}$$

whilst the same at the mid-span simplifies to

$$\psi_B^p = |\bar{M}_B| - 1. \tag{2.37}$$

Phase II motion ends when $\psi_B^p = 0$.

An admissible transverse displacement field for Phase II motion, shown schemat-

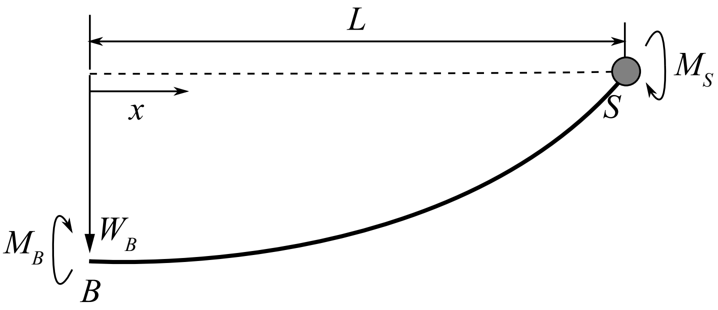

Figure 2.5: Schematic of transverse displacement profile for the right-hand half of the structural beam system in Phase II.

ically in Fig 2.5, is (Schleyer and Hsu, 2000)

$$W(x,t) = \Big[w_1(t_1) + w_2(t)\Big] \cos\frac{\pi x}{2L} \tag{2.38}$$

where $w_1(t_1)$ is the terminating amplitude of the generalised displacement from Phase I at t_1. Expressions for strain energy components are identical to those previously derived in Phase I (Eq. 2.32 for E^b_B; Eq. 2.34 for E^m_B, E^s_S and E^m_S) with the notable exception of the bending strain energy of the rotational spring at the supports which is as follows:

$$E^b_S(t) = |M_S|[\phi(t) - \phi_1] = M_0[\phi(t) - \phi_1] \tag{2.39}$$

where $\phi_1 = M_0/K_\phi$. Substituting Eqs. 2.32, 2.34 and 2.39 into Eq. 2.28 gives the equation of motion for Phase II. Transitional condition between phases proposed by Symonds et al. (1984) is adopted here to calculate the starting amplitude of the velocity in the current phase based on the terminating velocities in the previous phase. The starting amplitude of the generalised velocity in this phase is given by

$$\dot{w}_2 = \frac{8}{3\pi}\dot{w}_1(t_1) + \dot{w}_2(t_1) \tag{2.40}$$

where $\dot{w}_1(t_1)$ and $\dot{w}_2(t_1)$ refer to the terminating amplitude of the generalised velocity from Phase I at time t_1. Once the mid-span of the beam meets the fully plastic stress condition, i.e.

$$\psi^p_B = EI\kappa(t)/M_0 - 1 = 0 \tag{2.41}$$

where $\kappa(t) = \partial^2 W(x,t)/\partial x^2|_{x=0}$ is the curvature at the mid-span, it marks the end of Phase II deformation at the corresponding time of $t = t_2$.

2.3.3 Phase III: $t_2 < t \leq t_3$

Following Shen and Jones (1992) and Schleyer and Hsu (2000), it is assumed that the membrane force $\bar{N}$ is identically distributed throughout the span of the beam whilst the transverse shear force is negligible at the mid-span. The fully plastic stress conditions at the supports and mid-span of the beam are, respectively,

$$|\bar{M}_S|(1-\bar{Q}_S^2) + \bar{N}^2 + \bar{Q}_S^2 = 1, \quad \text{if} \quad |\bar{M}_S| > 0 \tag{2.42a}$$

$$\bar{N}^2 + \bar{Q}_S^2 = 1, \quad \text{if} \quad |\bar{M}_S| = 0 \tag{2.42b}$$

and

$$\bar{M}_B + \bar{N}^2 = 1. \tag{2.43}$$

If motion of the beam member ceases when the damage variable $D < 1$ (Mode I deformation), this will be followed by residual deformation in the form of elastic vibration. By contrast, if this happens when $D = 1$ then the beam will fail in either mode II or mode III.

Phase III motion begins with two existing stationary plastic hinges (one each at the support S and mid-span B) from Phase II. A travelling plastic hinge A then develops that moves towards the stationary hinge at the mid-span (Fig 2.6a) before ending up in a final two-hinge collapse configuration (Fig 2.6b). The admissible transverse displacement field at the beginning of Phase III motion shown in Fig 2.6a, is (Shen and Jones, 1992)

$$W(x,t) = \begin{cases} w_1(t_1) + w_2(t_2) + w_3(t) & \text{if } 0 \leq x \leq L-\xi \\ w_4(t) + \Big[w_1(t_1) + w_2(t_2) + w_3(t) - w_4(t)\Big]\frac{L-x}{\xi} & \text{if } L-\xi < x < L \end{cases} \tag{2.44}$$

where $w_1(t_1)$ and $w_2(t_2)$ are terminating amplitudes of the generalised displacements from Phases I (at time t_1) and II (at time t_2), respectively. When the

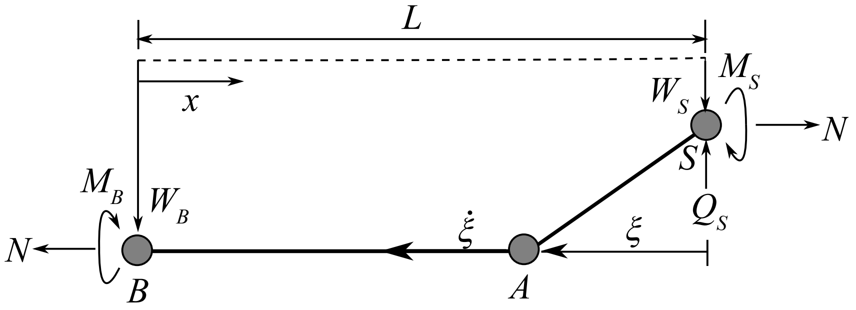

(a) Traveling hinge with $\xi < L$

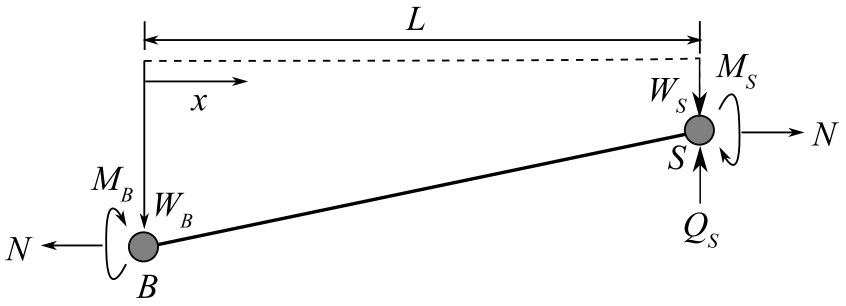

(b) Static hinge with $\xi = L$

Figure 2.6: Schematic of transverse displacement profile for the right-half of the structural beam system in Phase III (a) before and (b) after the travelling hinge reaches its mid-span.

travelling plastic hinge reaches the mid-span, i.e. $\xi = L$, the admissible transverse displacement field for Fig 2.6b becomes

$$W(x,t) = w_4(t) + \Big[w_1(t_1) + w_2(t_2) + w_3(t) - w_4(t)\Big]\frac{L-x}{L}. \tag{2.45}$$

The bending strain energies of the beam member and rotational spring are, respectively,

$$E_B^b(t) = M_B\frac{w_3(t) - w_4(t)}{\xi}, \tag{2.46}$$

and

$$E_S^b(t) = |M_S|\frac{w_3(t) - w_4(t)}{\xi}. \tag{2.47}$$

The membrane strain energies of the beam member and the horizontal axial spring may be expressed, respectively, as

$$E_B^m(t) = N\Delta_B(t) \tag{2.48}$$

and

$$E_S^m(t) = N\Delta_S(t) \tag{2.49}$$

where $\Delta_B(t) = \Delta(t)/(1+1/\sqrt{1-Q_S^2/Q_0^2})$ is the in-plane membrane displacement at the mid-span, $\Delta(t) = [w_3(t) - w_4(t)]^2/\xi$ is the total membrane displacement and $\Delta_S(t) = \Delta(t) - \Delta_B(t)$ is the membrane displacement at the supports. Here, it is assumed that in-plane membrane displacement is significant where a plastic hinge has developed (Schleyer and Hsu, 2000; Langdon and Schleyer, 2005). The shear strain energy of the vertical axial spring is

$$E_S^s(t) = Q_S w_4(t). \tag{2.50}$$

Note that the parameters M_S, Q_S, N, M_B, ξ and $\dot{\xi}$ in Eqs. 2.46–2.50 are unknowns. Recasting them in a non-dimensional form, viz. $\bar{M}_S$, $\bar{Q}_S$, $\bar{N}$, $\bar{M}_B$, $\bar{\xi} = \xi/L$ and $\dot{\bar{\xi}} = \dot{\xi}/L$, they will have to be computed as described below.

The non-dimensional velocity of the travelling hinge A can be expressed in the form of (Shen and Jones, 1992)

$$\dot{\bar{\xi}} = \frac{\sigma_Y}{\rho L^2} \frac{1.5(|\bar{M}_S| + \bar{M}_B) - 2\bar{Q}_S\dot{\bar{\xi}}(L/H)/\sqrt{3} + 6\bar{N}(\bar{w}_3 - \bar{w}_4) + \bar{\xi}[p(t)/p_c]}{\bar{\xi}(\dot{\bar{w}}_3 - \dot{\bar{w}}_4)} \tag{2.51}$$

where $\bar{w}_3 = w_3(t)/H$, $\dot{\bar{w}}_3 = \dot{w}_3(t)/H$, $\dot{\bar{w}}_4 = \dot{w}_4(t)/H$; $p_c = 4M_0/L^2$ is the fully plastic collapse force per unit length, i.e. the largest force per unit length that can be supported by the structural beam system when subjected to a pure bending moment before the bending moment at each plastic hinge equals the fully plastic bending moment M_0 (Jones, 1989). Note that when the travelling hinge A reaches the existing stationary hinge at the mid-span B, they coalesce into a single stationary hinge so that in subsequent motion

$$\dot{\bar{\xi}} = 0 \quad \text{and} \quad \bar{\xi} = 1. \tag{2.52}$$

The calculations of $\bar{M}_S$, $\bar{Q}_S$, $\bar{N}$, $\bar{M}_B$ would depend on whether damage had initiated. If the state variable $\omega_d < 1$, then $\bar{M}_S$, $\bar{Q}_S$ and $\bar{N}$ are governed by normality requirements so that plastic flow must occur at a non-negative energy dissipation rate since they have met the fully plastic stress condition (Eq. 2.42). Therefore, according to Shen and Jones (1992),

$$\bar{N}\Big(1+\frac{1}{\sqrt{1-\bar{Q}_S^2}}\Big) = 2(\bar{w}_3 - \bar{w}_4) \tag{2.53a}$$

$$\bar{Q}_S\Big[\frac{2}{\sqrt{1-\bar{Q}_S^2}} - \frac{|\bar{M}_S|}{\sqrt{1-\bar{Q}_S^2}}\Big] = \frac{4\bar{\xi}(L/H)\dot{\bar{w}}_4}{\sqrt{3}(\dot{\bar{w}}_3 - \dot{\bar{w}}_4)} \tag{2.53b}$$

if $|\bar{M}_S| > 0$, and

$$\bar{N}\Big[\frac{2\dot{\bar{w}}_4}{\sqrt{3}\bar{Q}_S} + \frac{\dot{\bar{w}}_3 - \dot{\bar{w}}_4}{\bar{\xi}(L/H)}\Big] = 2\frac{(\bar{w}_3 - \bar{w}_4)(\dot{\bar{w}}_3 - \dot{\bar{w}}_4)}{\bar{\xi}(L/H)} \tag{2.54}$$

if $|\bar{M}_S| = 0$. If the state variable $\omega_d = 1$, then the non-dimensional bending moment $\bar{M}_S$, membrane force $\bar{N}$ and shear force $\bar{Q}_S$ are governed by the damage equations of Eq. 2.14. Note that non-dimensional bending moment $\bar{M}_B$ remains governed by fully plastic stress condition established for the mid-span ($\psi_B^p = 0$) in Eq. 2.43.

To calculate $\bar{M}_S$, $\bar{Q}_S$, $\bar{N}$ and $\bar{M}_B$, they have to be expressed as functions of $\bar{w}_3$, $\bar{w}_4$, $\dot{\bar{w}}_3$, $\dot{\bar{w}}_4$, $\bar{\xi}$, $\dot{\bar{\xi}}$ and t through Eqs. 2.42, 2.43, 2.51, 2.53 and 2.54 if $\omega_d < 1$; and through Eqs. 2.14, 2.15, 2.43 and 2.51 if $\omega_d = 1$. The temporal evolution of these parameters are obtained by solving the aforementioned equations using the well-known 4th order Runge-Kutta method with the initial conditions of $w_3 = w_4 = 0$ and $\dot{w}_4 = 0$. Following Symonds et al. (1984), the starting amplitude of the generalised velocity $\dot{w}_3$ for Phase III is given by

$$\dot{w}_3 = \frac{12}{\pi^2}\dot{w}_2(t_2) \tag{2.55}$$

where $\dot{w}_2(t_2)$ refers to the terminating amplitude of the generalised velocity from Phase II at time t_2. Phase III deformation ends at time t_3 if motion of the beam member ceases i.e.

$$\dot{w}_3(t_3) = 0. \tag{2.56}$$

If the damage variable $D < 1$ when this occurs, then the beam fails in mode I. Otherwise, a mode II or mode III failure would ensue if $D = 1$.

If the structural system fails before all the initial kinetic energy is expended, then the beam member would have a residual kinetic energy at the point of severance. Parts of this are absorbed through further plastic deformation as the beam member continues to deform until it reaches a rigid permanent set whilst the remaining as translational kinetic energy. In the current model, the energy that is absorbed post failure is not considered. The residual energy and momentum for one-half of the structural beam system at failure are given by (Shen and Jones, 1992)

$$E_{ktr} = \frac{1}{2}m(L-\xi)\dot{W}_B^2(t_3) + \frac{1}{2}m\int_{L-\xi}^{L}\left[\dot{W}_S(t_3) + [\dot{W}_B(t_3) - \dot{W}_S(t_3)]\frac{L-x}{\xi}\right]^2 \mathrm{d}x \tag{2.57}$$

and

$$I_{ktr} = m(L-\xi)\dot{W}_B(t_3) + m\int_{L-\xi}^{L}\left[\dot{W}_S(t_3) + [\dot{W}_B(t_3) - \dot{W}_S(t_3)]\frac{L-x}{\xi}\right]\mathrm{d}x \tag{2.58}$$

or, in non-dimensional form, as

$$\bar{E}_{ktr} = \frac{E_{ktr}}{E_{\text{ext}}} \tag{2.59}$$

and

$$\bar{I}_{ktr} = \frac{I_{ktr}}{I_{\text{ext}}} \tag{2.60}$$

where $I_{\text{ext}} = L\int_0^{t_d} p(t)\,\mathrm{d}t$ is the external momentum, $E_{\text{ext}} = \rho BHLV_0^2/2$ is the external energy and $V_0 = I_{\text{ext}}/\rho HBL$ is the equivalent impulsive velocity.

Chapter 3

Blast response of elasto-plastic beams

3.1 Introduction

As previously highlighted, majority of the analytical models on blast loading of beams and plates in the literature - Jones (1976), Wen (1996), Shen and Jones (1992), Yu and Chen (2000), etc. - were formulated within the constitutive framework of limit analysis which disregards the influence of material elasticity. Whether these rigid-plastic methods of analysis provide an acceptable approximation of the dynamic response of actual elasto-plastic structures is an important issue. Symonds (1985) showed that a rigid-plastic analysis may be acceptable if the energy ratio $R \gg 1$, where R is the ratio of the total energy imparted by the loading E_{in} to the maximum elastic strain energy capacity $U_e^{\max}$ of the structure given by

$$R = \frac{E_{\text{in}}}{U_e^{\max}}. \tag{3.1}$$

This problem was re-investigated by Symonds and Frye (1988) through a single-degree-of-freedom (SDOF) mass spring model - using either an elastic perfectly-plastic or rigid perfectly-plastic spring - where it was found that a large energy ratio ($R \gg 1$) is a necessary, but not a sufficient, condition for a rigid-plastic approximation. If the duration of the load pulse is not brief in comparison to the fundamental period of elastic vibration of the structure, a rigid-plastic idealisation would lead to an unacceptably high error, by as much as 60%. In some cases this error may even be negative, i.e. the rigid-plastic solution grossly underestimates the final deformation of the structure (Stronge and Yu, 1993). Subsequent study by Yu (1993) investigated the influence of elasticity on the dynamic plastic response of cantilever beams and showed that the pulse shape and its rise time, too, have a significant influence on the final beam deformation.

Existing models based on rigid-plastic methods cannot be used to study the dynamic response of elasto-plastic beams subjected to intense non-impulsive loadings. In addition, it is unclear as to how pulse shape, and its duration, influence the mode of deformation and how limits to deformation due to necking localisation and/or ductile fracture affect the final performance of a beam. These issues will be investigated here using the analytical model developed in Chapter 2. For impulsively loaded beams, there exists experimental data by Menkes and Opat (1973) against which the current analytical predictions (Chapter 2) may be validated. However, no equivalent experimental data for non-impulsive load cases exist to the best of the author's knowledge. Hence, a 3D non-linear finite element (FE) model - validated against the data of Menkes and Opat (1973) - is first developed and their numerical predictions are compared to the current analytical model for impulsive load cases. Both the validated FE and analytical models are then employed to study the effects of non-impulsive loading.

3.2 Finite element implementation

3.2.1 Mesh, loading and boundary conditions

Finite element analyses were performed using ABAQUS/Explicit (2012). All the beams modelled have length $2L$, width B and thickness H. Only one-half is modelled since reflective symmetry exists on the plane at $x = 0$, $-B/2 \leq y \leq B/2$ and $-H/2 \leq z \leq H/2$. Figure 3.1 shows the displacement boundary conditions that were imposed on the plane of symmetry and at the supports. 8-node solid brick elements (C3D8R) with reduced integration and hour-glass control were used. All brick elements have equal dimension of 0.000783 m on all sides; hence, a typical 0.203 m ($2L$) $\times$ 0.00635 m (H) $\times$ 0.0254 m (B) beam tested by Menkes and Opat (1973) would comprise of 33024 ($129 \times 8 \times 32$) elements in its corresponding FE model. Results of convergence studies - presented later in Fig 3.3 - will show that this is sufficient to capture necking localisation, progressive damage and ductile fracture with acceptable fidelity.

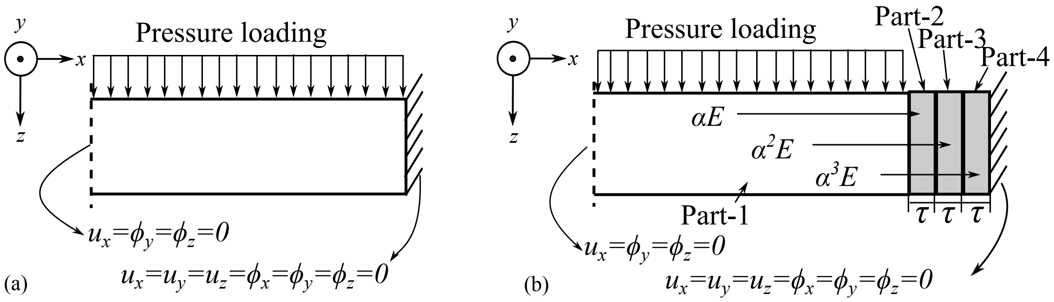

Figure 3.1: Schematic of boundary, or support, conditions (BCs) in the FE simulations: (a) standard fully clamped BC, and (b) modified BC. u and ϕ denote displacement and rotation degree of freedom, respectively.

The ductile beam is loaded transversely by a uniformly distributed pressure pulse. Unless otherwise specified, the pressure pulse is assumed to be linearly-decaying, i.e. $p(t) = p_0(1 - t/t_d)$ where p_0 is the peak pressure (given in load per unit length) and t_d is the pulse duration. A pulse duration of $t_d = 0.01$ ms is used here - this follows Shen and Jones (1992). However, it needs to be established that a pulse of finite duration $t_d = 0.01$ ms can be classed as *impulsive*. Following Xue and Hutchinson (2003), FE simulations were performed to determine the maximum mid-span deflection W_0 for fully-clamped beams subjected to a linearly-decaying pressure loading of different duration t_d. All beams modelled have identical dimensions 0.203 m ($2L$) $\times$ 0.00635 m (H) $\times$ 0.0254 m (B) and material properties listed in Table 3.2 - identical to the beams tested by Menkes and Opat (1973). The response time T of the beam - defined as the time it takes to attain maximum mid-span deflection under a zero-period impulse ($t_d = 0$ so the beam acquires an instantaneous initial velocity) - was found numerically to be 0.3 ms. Figure 3.2 shows the variation of the maximum non-dimensional mid-span displacement W_0/H versus pulse duration t_d/T for different levels of impulse

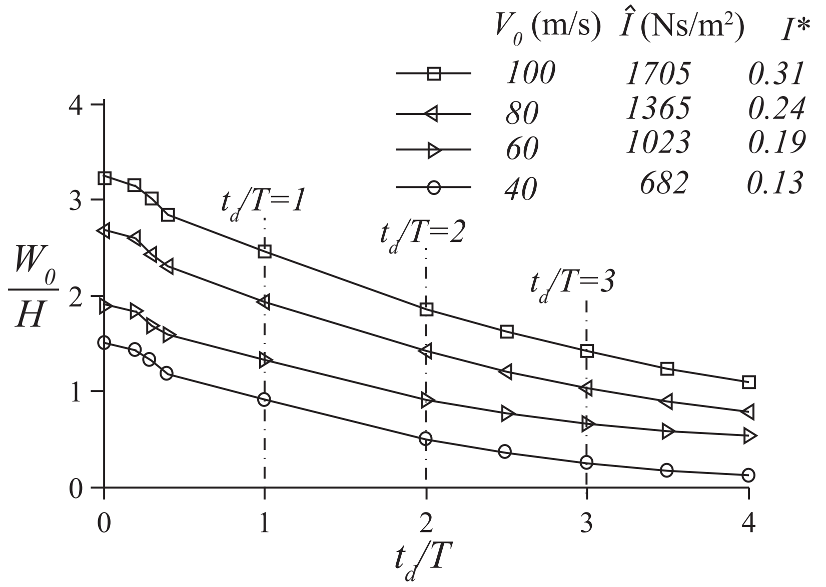

Figure 3.2: Non-dimensional mid-span displacement W_0/H versus impulse duration t_d/T at different levels of $\hat{I}$. The aluminium beam has dimensions 0.203 m ($2L$) × 0.00635 m (H) × 0.0254 m (B).

per unit area $\hat{I}$, expressed as

$$\hat{I} = \frac{1}{B}\int_0^{t_d} p(t)\mathrm{d}t. \tag{3.2}$$

For linearly decaying pulse, $\hat{I} = p_0 t_d/2B$. At $t_d/T = 0.4$, the predicted maximum deflection is 12% less than its corresponding zero-period limit. This discrepancy increases to more than 50% at $t_d/T = 3$. This trend is representative of solid beams subjected to blast loadings and is independent of pulse shape. Thus, a linearly-decaying pressure pulse of finite duration $t_d = 0.01$ ms is, indeed, impulsive since $t_d/T = 0.033 \ll 0.4$. To simulate non-impulsive loading $t_d/T \gg 1$ should be used. The intensity of loading, for both impulsive and non-impulsive load cases, is characterised by a non-dimensional impulse I^* given by

$$I^* = \frac{\hat{I}}{H\sqrt{\sigma_Y \rho}}. \tag{3.3}$$

Figure 3.1a depicts a standard displacement boundary conditions that would need to be imposed for a fully-clamped boundary condition (BC). It is shown later that the local equivalent plastic strain in the beam abutting the supports does not converge with repeated mesh refinement. In order to accurately model progressive ductile fracture at the supports, a modified BC given in Fig 3.1b is adopted. To demonstrate its efficacy, it needs to be shown that both the standard and modified BCs give similar beam deflection profiles, but only the latter gives a converged equivalent plastic strain at the boundary/support. For the modified BC, three additional parts (labelled 2-4) are added to the end of the original solid beam (part-1) to form an extended boundary shown schematically in Fig 3.1b. Note that the standard fully-clamped BC of Fig 3.1a is imposed on part 4. All the additional parts have equal width τ and identical material properties as the solid beam, apart from a gradation of their elastic modulus E, by a factor α. The parameters $\tau = H/6$ and $\alpha = 10$ are obtained by calibration to the experimental data of Menkes and Opat (1973).

Table 3.1: Number of elements in each direction for Part-1 of the beam (0.203 m ($2L$) $\times$ 0.00635 m (H) $\times$ 0.0254 m (B))

Mesh	Number of elements along z-direction	Number of elements along x- direction	Number of elements along y-directions
1	1	16	4
2	2	32	8
3	3	48	12
4	4	64	16
5	5	80	20
6	6	96	24
7	7	112	28
8	8	128	32
9	9	144	36
10	10	160	40

Figure 3.3 plots the maximum equivalent plastic strain $\bar{\epsilon}^p$ versus mesh density in part-1 for the two BCs. The number of elements in each direction of the beam is listed in Table 3.1. For a beam with a standard BC (Fig 3.1a), the maximum $\bar{\epsilon}^p$ must occur next to the supports where tearing is expected to initiate. It is

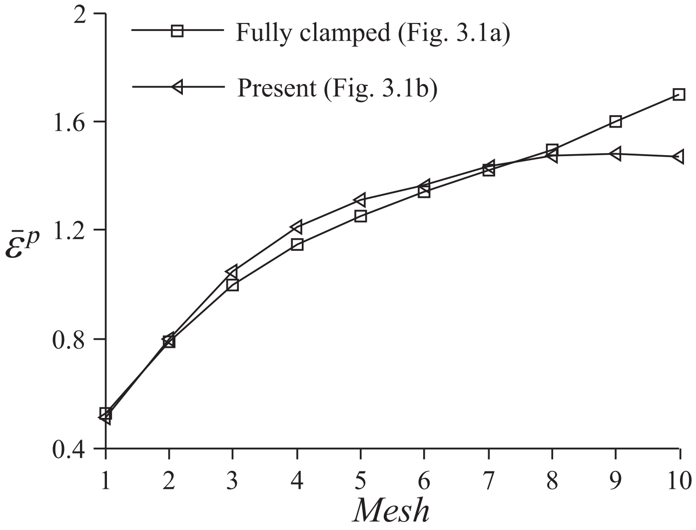

Figure 3.3: Maximum equivalent plastic strain $\bar{\epsilon}^p$ predicted for part-1 by the FE model. Results shown are for an aluminium beam of dimensions 0.203 m ($2L$) × 0.00635 m (H) × 0.0254 m (B) subjected to a non-dimensional impulse $I^* = 0.466$ with $t_d = 0.01$ ms. Properties for the aluminium beam is given in Table 3.2. 'Present' refers to predictions using the modified boundary condition in Fig 3.1b.

evident that $\bar{\epsilon}^p$ does not converge with repeated mesh refinement for the standard BC. Figure 3.3 shows that mesh size No.8 gives sufficiently accurate results and will be used here.

Figure 3.4a compares the deflection profiles predicted by the two BCs which show negligible differences; likewise, for the temporal-history of their mid-span deflection in Fig 3.4b. Therefore, it is reasonable to conclude that the modified BC predicts acceptable mid-span deflection provided necking localisation and ductile fracture had not intervened.

3.2.2 Material properties and damage model

The material description adopted is based on the conventional J_2 plasticity constitutive relation with linear isotropic hardening, which allows progressive degradation of material stiffness to be implemented in finite elements. This ap-

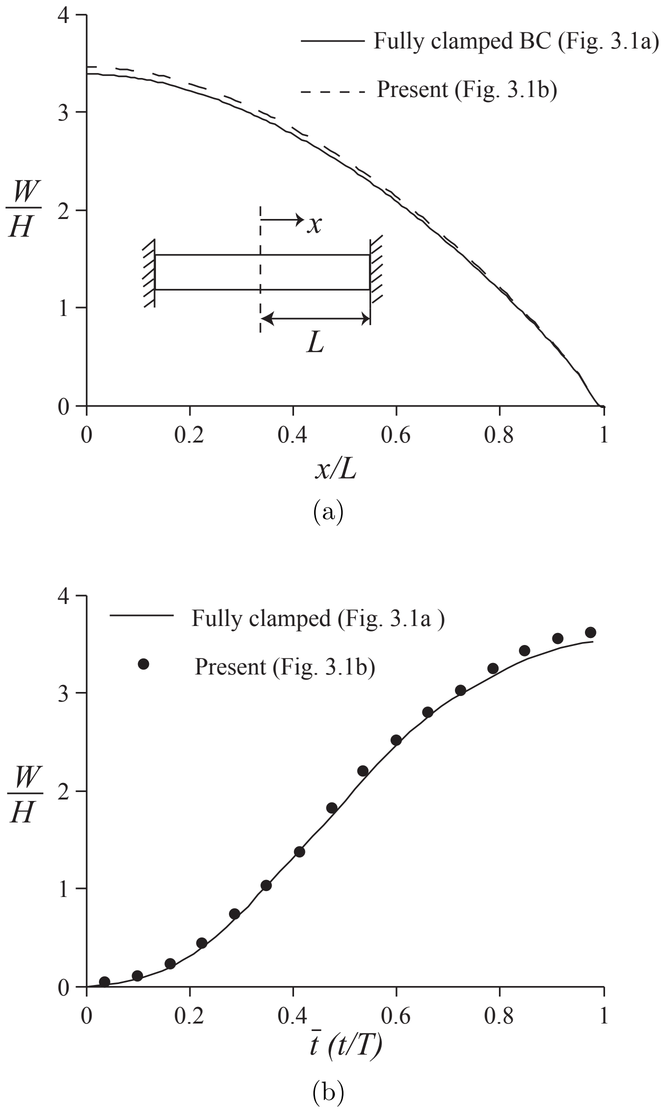

Figure 3.4: (a) Deflection profile along the x-axis and (b) temporal-history for the mid-span deflection. Results shown are for aluminium beams of dimensions 0.203 m ($2L$) $\times$ 0.00635 m (H) $\times$ 0.0254 m (B) subjected to a non-dimensional impulse of $I^* = 0.354$ with $t_d = 0.01$ ms. Material properties for the beam are listed in Table 3.2. 'Present' refers to predictions using the modified boundary condition in Fig 3.1b.

proach, coupled with element deletion, is widely used to model progressive damage and fracture in ductile materials (Hancock and Mackenzie, 1976; Johnson and

Cook, 1983). All the beams modelled are made of Aluminium 6061-T6, which is often assumed to be strain rate insensitive (Jones et al., 1971). Table 3.2 lists the material properties of the beams tested by Menkes and Opat (1973).

Table 3.2: Material properties for the Aluminium 6061-T6 beam (Menkes and Opat, 1973)

Density, ρ (kg/m^3)	Young's modulus, E (GPa)	Static yield stress, σ_Y (MPa)	Ultimate yield stress, σ_U (MPa)	Poisson's ratio
2686	69	283	320	1/3

The progressive damage model for ductile materials in ABAQUS/Explicit is adopted here. The criterion for ductile damage initiation is given by

$$\omega_d = \int \frac{d\bar{\epsilon}^p}{\bar{\epsilon}^p_d(\eta, \dot{\bar{\epsilon}}^p)} = 1 \tag{3.4}$$

where ω_d is a state variable that increases monotonically with the equivalent plastic strain. Here, the equivalent plastic strain $\bar{\epsilon}^p_d$ at the onset of ductile damage is assumed to be a function of stress triaxiality η and plastic strain rate $\dot{\bar{\epsilon}}^p$. When Eq. 3.4 is met, the damage variable D would increase according to (ABAQUS/Explicit, 2012)

$$\dot{D} = \frac{L_e \dot{\bar{\epsilon}}^p}{\bar{u}^p_f} \tag{3.5}$$

where $\bar{u}^p_f$ is the effective plastic displacement at failure and $L_e = 7.83 \times 10^{-4}$ m is the characteristic length of the first-order element used in the FE model. Any element whose stiffness is fully degraded, i.e. $D = 1$, is deleted from the mesh. The two parameters needed to implement a ductile damage model are the damage strain $\bar{\epsilon}^p_d = 0.8$ and the failure displacement $\bar{u}^p_f = 0.011$ m; both are found through calibration to the experimental data of Menkes and Opat (1973).

In line with the definition of *failure* in Chapter 2, the FE simulation terminates when a beam member completely detaches from its supports. The smallest impulse needed to induce beam failure either in mode II or III is referred to here as the critical impulse at mode I→II or II→III transition, respectively (Jones, 1989). To distinguish between failure in mode II and III in the FE simulations, a separate damage parameter for shear would need to be introduced since a sharp distinction between the two modes is not normally found. The two possibilities are the maximum transverse shear sliding ($\Delta^s_{\max}$) criterion by Jones (1976) and Yu and Chen (2000), or an energy-based criterion by Shen and Jones (1992). However, neither of these are feasible since $\Delta^s_{\max}$ is not a monotonic function of I^* and the plastic work per unit volume (energy density) is a mesh-dependent quantity (Yu and Chen, 2000). Consequently, the critical impulse at mode II→III transition is not predicted by FE unlike the analytical model developed in Chapter 2.

3.3 Validation of FE and analytical predictions

All the beam specimens tested by Menkes and Opat (1973) - they have different length (L) and thickness (H) combinations but identical width ($B = 25.4$ mm) - are made of Al 6061-T6 with material properties given in Table 3.2. The pressure pulse, in both the FE and analytical models, was assumed to be linearly-decaying with a pulse duration $t_d = 0.01$ ms. An algorithm flow-chart on the numerical implementation of Chapter 2 is given in Fig 3.5.

Figure 3.6 compares the predicted mid-span deflection (W_0/H), at either the point of cessation of motion or failure (if complete detachment from the supports had occurred), to its corresponding experimental data. The analytical predictions by Shen and Jones (1992) - these are available only for specimens 3 and 5 - are included for comparison. In mode I, there is good agreement between experiments, FE and analytical predictions. The current FE and analytical models correctly predict a reduction in W_0/H with increasing I^* in modes II and III; they are also broadly in agreement with the predictions by Shen and Jones (1992) for specimens 3 and 5. Apart from specimen 1, the predicted critical impulse at mode I→II and II→III also agree well with those reported by Menkes and Opat (1973).

There is a notable lack of experimental data for modes II and III deformation in Fig 3.6. To address this, relative mid-span deflections ΔW_0 ($\triangleq W_B(t_3) - W_S(t_3)$)

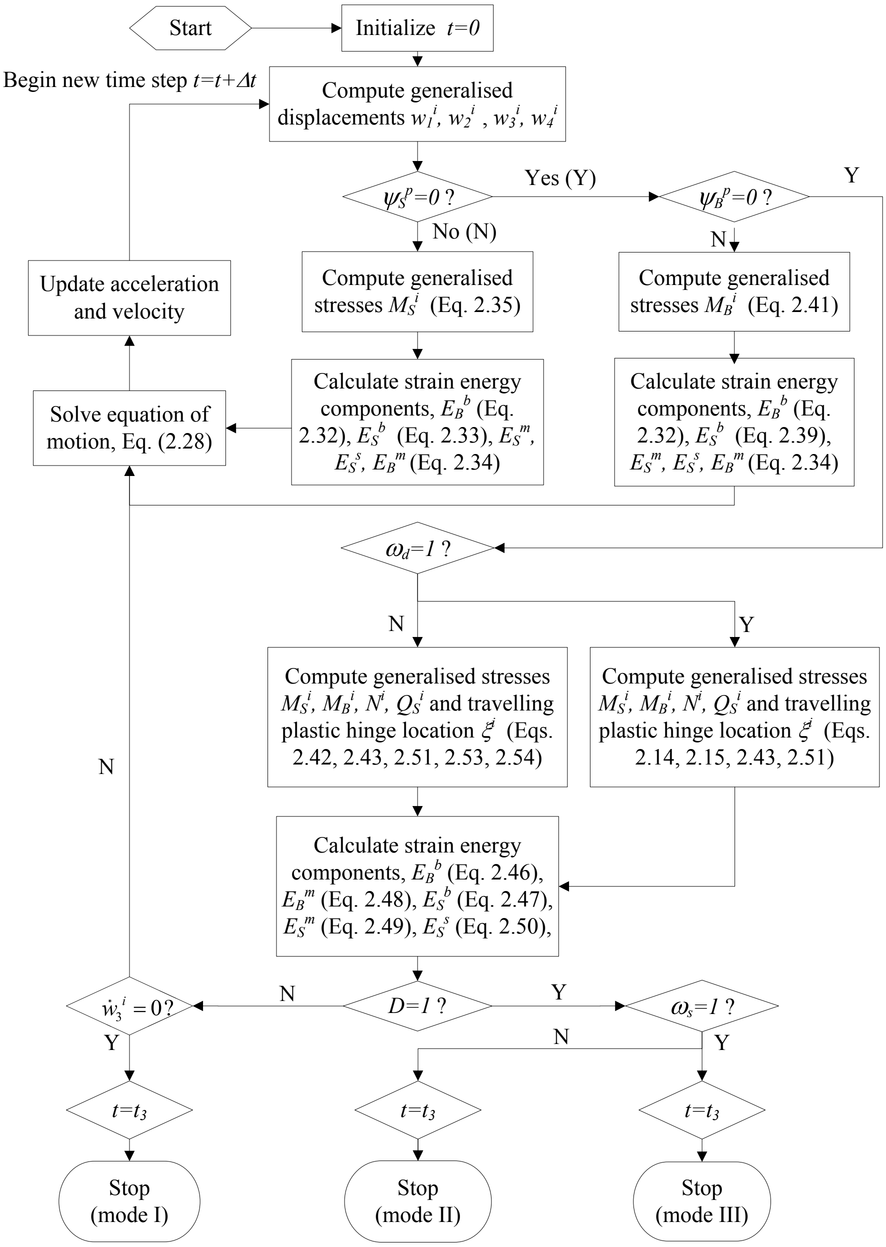

Figure 3.5: Algorithm flow-chart on the numerical implementation of the analytical model presented in Chapter 2.

were deduced using existing 'post-test' photographs for specimens 3 and 5 provided by Menkes and Opat (1973). Figure 3.7 compares this relative mid-span deflection $\Delta W_0/H$ to the current analytical predictions and that by Shen and

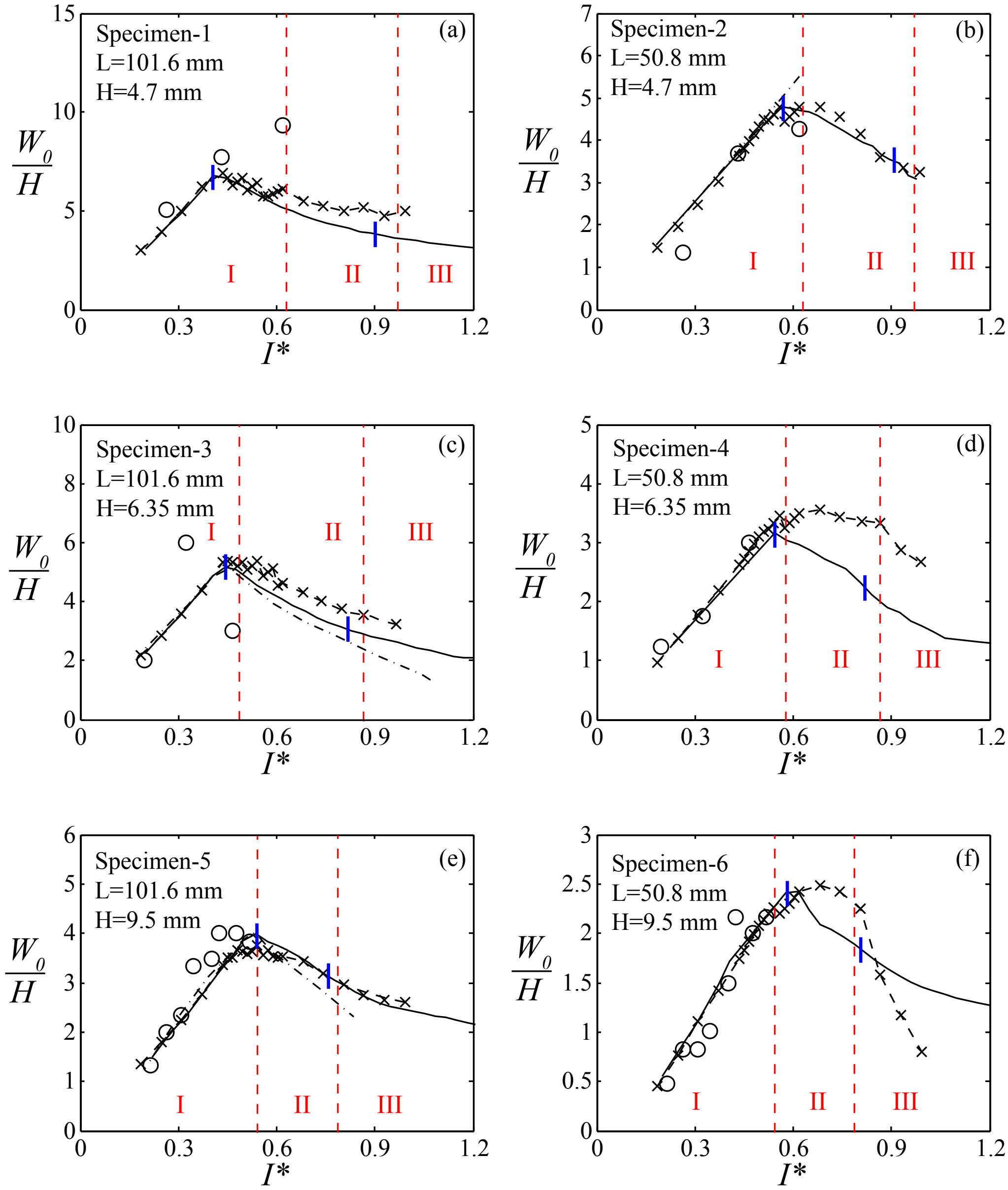

Figure 3.6: Variations of the non-dimensional mid-span deflection W_0/H with non-dimensional impulse I^*. I, II and III indicates the three distinct damage modes reported by Menkes and Opat (1973). ○ Experiments by Menkes and Opat (1973); -.- Analytical predictions by Shen and Jones (1992); — current analytical model; | critical impulse at mode transition by current analytical model; -×- current FE predictions.

Jones (1992): a reasonably good agreement for modes I and II is noted. However, the current model over-predicts $\Delta W_0/H$ in mode III because it assumes a constant hinge length of $l = 2H$ - this follows the approach of Wen (1996), Jones (1976) and Alves and Jones (2002a) - instead of re-calibrating for a new hinge length using each data point which was employed by Shen and Jones (1992).

Table 6.4 compares the critical non-dimensional impulse I^* at mode transitions. The current analytical model adopts a rupture strain of $\epsilon_r = 0.5$ (Shen and Jones, 1992) and an effective strain of $\epsilon_d = 0.38$ corresponding to the onset of damage. The latter was obtained by calibrating to the critical I^* corresponding to mode I→II transition for specimen 5. Similarly, for the FE model, $\bar{\epsilon}_d^p = 0.8$ and $\bar{u}_f^p = 0.011$ m are also obtained through calibration to the aforementioned. Current predictions (FE and analytical) for the critical I^* corresponding to mode I→II transition are in good agreement with the experimental data - as does the predictions by Shen and Jones (1992) - with the notable exception of specimen 1

Table 3.3: Critical impulse I^* for mode transitions.

Specimen No	Mode	Current Analytical	Current FE	Analytical[1]	Experiments[2]
1	I → II	0.40	0.43	-	0.63
	II → III	0.90	-	-	0.97
2	I → II	0.57	0.51	-	0.63
	II → III	0.92	-	-	0.97
3	I → II	0.44	0.43	0.46	0.49
	II → III	0.82	-	0.81	0.87
4	I → II	0.55	0.54	-	0.58
	II → III	0.82	-	-	0.87
5	I → II	0.54	0.54	0.54	0.54
	II → III	0.76	-	0.76	0.79
6	I → II	0.58	0.56	-	0.54
	II → III	0.81	-	-	0.79

[1](Shen and Jones, 1992) and [2](Menkes and Opat, 1973).

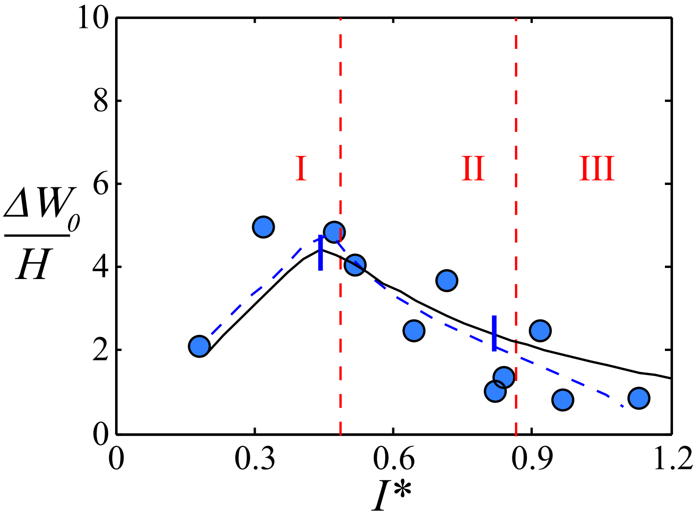

(a) Specimen-3

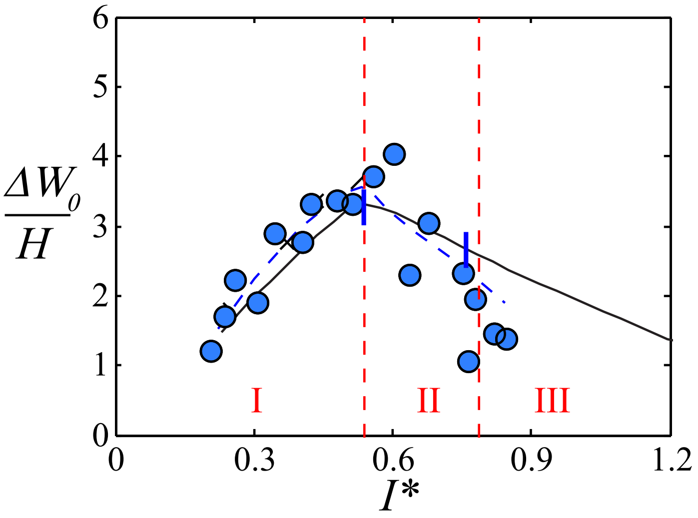

(b) Specimen-5

Figure 3.7: Variation of the relative mid-span displacement $\Delta W_0/H$ with non-dimensional impulse I^*. ● experimental data; - - analytical predictions by Shen and Jones (1992); – current analytical predictions; | critical impulse at mode transition by current analytical model.

which is considerably lower. In general, the predicted I^* at mode II→III transition agrees well with experimental data.

3.4 Response to non-impulsive loads

In the previous section, predictions by FE and the current analytical model are validated against experimental data for impulsive loads. Both models are now employed to investigate the dynamic response of elasto-plastic beams to non-impulsive loads. Two of the beams - specimens 3 and 5 - will be modelled here. Unless otherwise specified, a linearly decaying pressure pulse is always prescribed.

3.4.1 Mid-span deflection and critical impulse at mode transitions

Figure 3.8 plots the non-dimensional mid-span deflection W_0/H against I^* for pulse durations between $0.01 \leq t_d \leq 2$ ms. Note that $t_d = 0.01$ ms corresponds to impulsive loading - see Section 3.2.1. There is excellent agreement between the FE and analytical predictions. Current FE simulations show that beam failure always occurs at the supports regardless of pulse duration t_d which is the reason why failure criteria was established only for the supports in Section 2.2.3. The results in Fig 3.8 can be summarised as follows: (1) A broadly similar overall trend for the mid-span deflection with I^* for both impulsive and non-impulsive loads, i.e. W_0/H increases initially before reducing with I^*; (2) At any given I^*, the mode I deflection reduces with increasing t_d whilst the reverse occurs in mode II; (3) The mid-span deflection at mode I→II transition is insensitive to t_d; and, (4) Mode III deflection for non-impulsive loads are considerably higher than its corresponding impulsive counterpart at the same I^*.

Table 3.4 compares the predicted critical impulse by the analytical model and FE. The results show that I^* for mode I→II transition increases with pulse duration t_d. In a similar vein, this is also observed for the corresponding mode II→III transition. It is worth noting that for impulsive loads, the non-dimensional critical impulse I^* for mode II→III transition depends only on material properties (Jones, 1976 and Yu and Chen, 2000); by contrast, it is shown here that the critical I^* increases with the pulse duration for non-impulsive loadings.

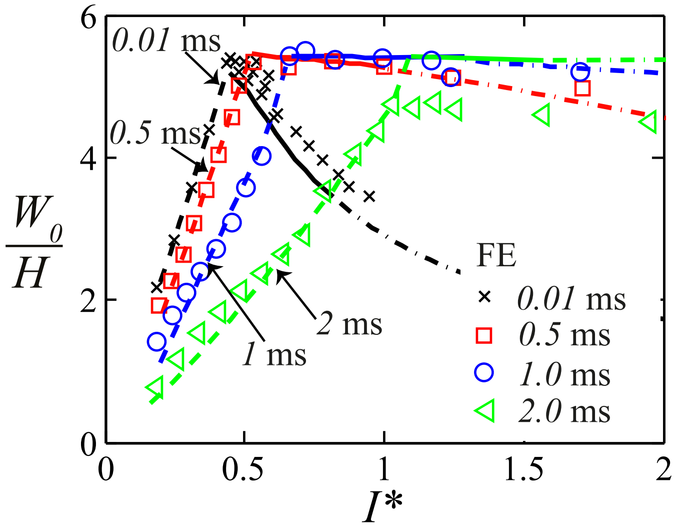

(a) Specimen-3 (0.203 m × 0.00635 m × 0.0254 m)

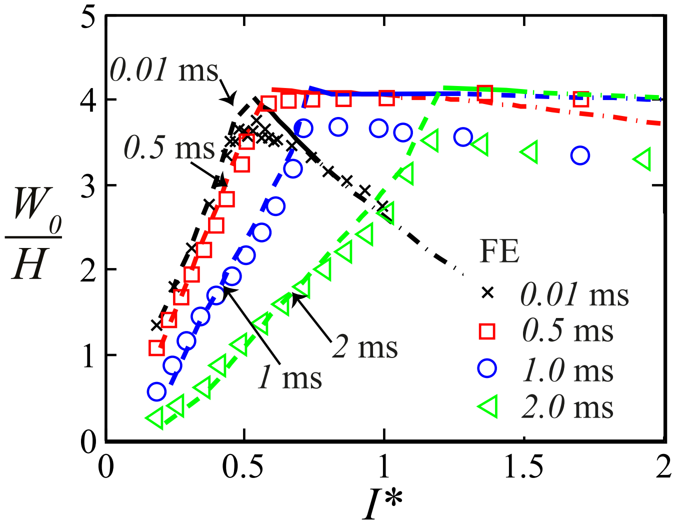

(b) Specimen-5 (0.203 m × 0.00947 m × 0.0254 m)

Figure 3.8: Variation of the non-dimensional mid-span deflection W_0/H against non-dimensional impulse I^* for a linearly decaying pressure with different pulse durations. Black lines (t_d = 0.01 ms) correspond to impulsive loads. Current analytical predictions: - - - mode I; — mode II; -.-.- mode III.

Table 3.4: Predicted critical impulse I^* by the analytical (and FE) model for different pulse duration t_d.

Specimen No	Mode	t_d 0.01 ms	t_d 0.5 ms	t_d 1.0 ms	t_d 2.0 ms
3	I → II	0.44 (0.43)	0.51 (0.50)	0.66 (0.64)	1.09 (1.03)
	II → III	0.82 (-)	0.99 (-)	1.27 (-)	1.56 (-)
5	I → II	0.54 (0.54)	0.60 (0.57)	0.74 (0.71)	1.21 (1.18)
	II → III	0.76 (-)	1.06 (-)	1.28 (-)	1.51 (-)

3.4.2 Partitioning of energy

Introducing a non-dimensional strain energy defined as the ratio of the total potential (strain) energy of the structural beam system to the work done by the external pressure loading E^T at the point of cessation of beam motion or at failure given by

$$\bar{E}^P = \frac{E^P(= E_S^b + E_S^m + E_S^s + E_B^b + E_B^m)}{E^T\Big(= \int_0^{t_3} p(t)[\int_0^L \dot{W}(x,t)\mathrm{d}x]\mathrm{d}t\Big)}. \tag{3.6}$$

Figure 3.9 plots the variation of $\bar{E}^P$ versus I^* for different pulse duration t_d where it shows an excellent agreement between the FE and analytical predictions. Notice that $\bar{E}^P$ remains at unity throughout mode I which implies that the external work is dissipated entirely through the various plastic work components by the structural beam system. Beyond the mode I→II transition, $\bar{E}^P$ drops dramatically suggesting that a finite amount of residual energy remains in the beam post failure. The effect of pulse duration t_d upon this residual energy (and momentum) will be further discussed in Section 3.4.3. For a given I^*, increasing the pulse duration t_d has the dramatic effect of increasing the non-dimensional strain energy of a beam failing in modes II or III. This is consistent with the results shown in Fig 3.8 since more non-dimensional potential (strain) energy is absorbed through larger mid-span deflection.

The components of plastic work absorbed at the *supports* through bending,

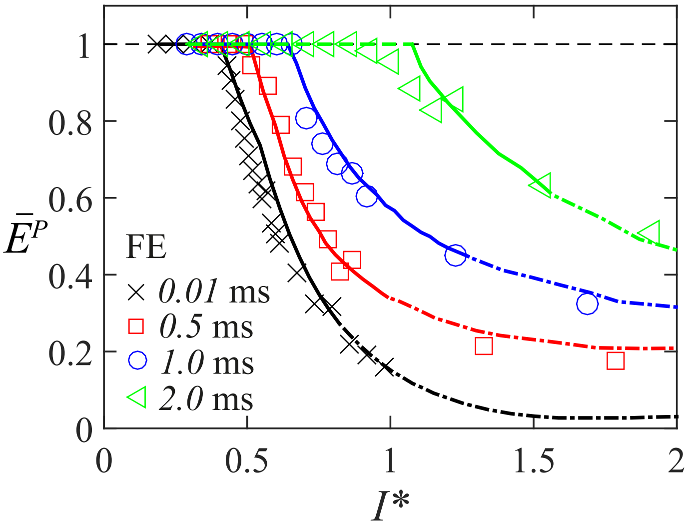

(a) Specimen-3, (0.203 m × 0.00635 m × 0.0254 m)

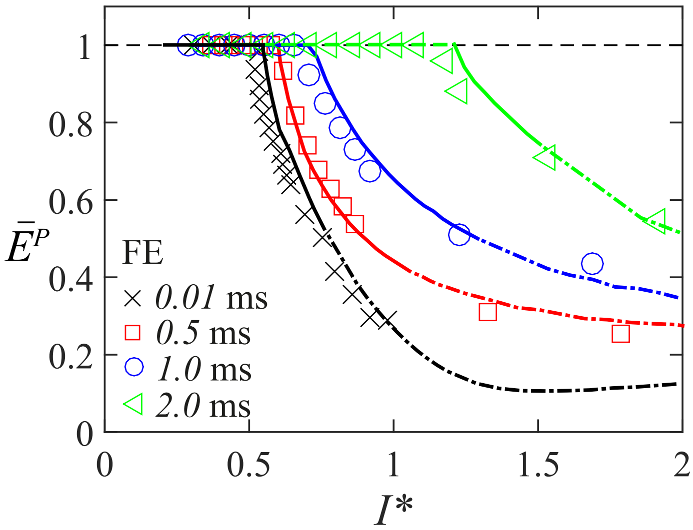

(b) Specimen-5, (0.203 m × 0.00947 m × 0.0254 m)

Figure 3.9: Non-dimensional strain energy $\bar{E}^P$ for the two specimens shown in Fig 3.8. Black lines ($t_d = 0.01$ ms) correspond to impulsive loads. - - denotes mode I; – denotes mode II; -.- denotes mode III.

membrane and shear deformation are non-dimensionalised as follows:

$$\bar{E}_S^b = \frac{E_S^b}{E_S^s + E_S^b + E_S^m}, \quad \bar{E}_S^m = \frac{E_S^m}{E_S^s + E_S^b + E_S^m}, \quad \text{and} \quad \bar{E}_S^s = \beta = \frac{E_S^s}{E_S^s + E_S^b + E_S^m} \tag{3.7}$$

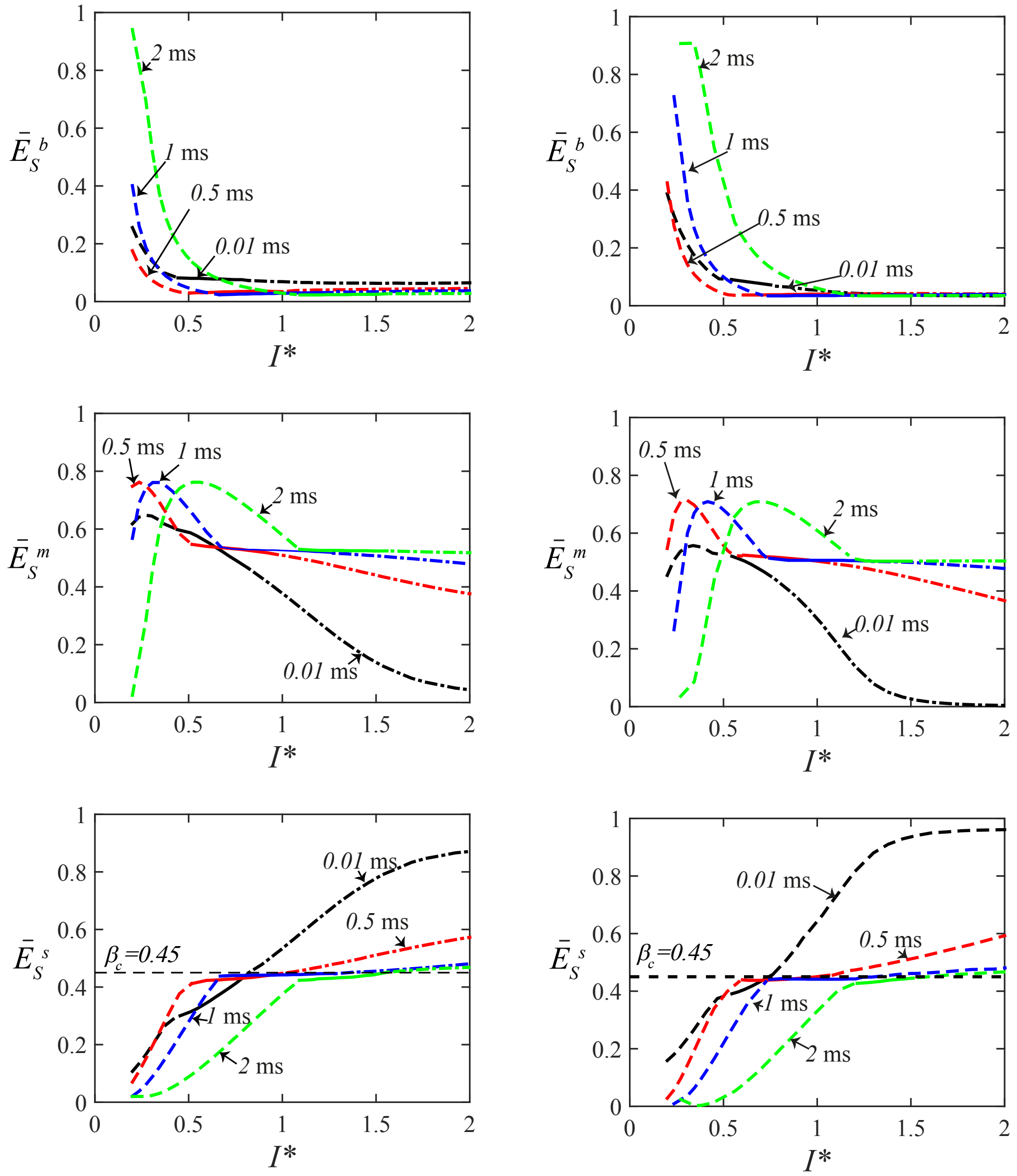

(a) Specimen-3 (0.203 m × 0.00635 m × 0.0254 m)

(b) Specimen-5 (0.203 m × 0.00947 m × 0.0254 m)

Figure 3.10: Components of the plastic work absorbed through bending, membrane and shear deformation at the *supports* for the specimens shown in Fig 3.8. Black lines ($t_d = 0.01$ ms) correspond to impulsive loads. - - denotes mode I; – denotes mode II; -.- denotes mode III.

where $\bar{E}_S^b + \bar{E}_S^m + \bar{E}_S^s = 1$. Figure 3.10 plots the 3 components of plastic work at the supports against I^* at the point of cessation of beam motion or at failure. The overall trend between the non-dimensional energy components and I^* are as follows: (1) $\bar{E}_S^b$ reduces monotonically with I^*; (2) $\bar{E}_S^m$ increases initially, reaching a peak value, before reducing with I^*; and, (3) $\bar{E}_S^s$ increases monotonically with I^*. In general, Figure 3.10 shows that failure at the supports - in mode II and III - under impulsive and non-impulsive loadings are primarily through a combination of membrane and shear deformations. It is worth noting the critical β value ($\beta_c = 0.45$) marking the transition from mode II→III is obtained based on impulsive load cases - see Shen and Jones (1992) and Yu and Chen (2000). A higher β_c value would require a higher critical I^* to induce mode II→III transition with a corresponding reduction in the mid-span deflection at the mode transition - see Fig 3.8.

Several studies (Li and Jones, 2000; Shen and Jones, 1992; Yu and Chen, 2000; Jones, 1976) have found that under impulsive loading, the mode II and III deformation is dominated by membrane and transverse shear, respectively. Beyond the mode I→II transition, Figure 3.10 shows a reduction in the non-dimensional shear strain energy $\bar{E}_S^s$ and an increase in the non-dimensional membrane energy $\bar{E}_S^m$ with t_d for a given I^*. The reduction in $\bar{E}_S^m$ (and increase in $\bar{E}_S^s$) becomes less evident with increasing pulse duration. Notwithstanding, the results above are consistent with the previous studies for impulsively loaded beams (Li and Jones, 2000; Shen and Jones, 1992; Yu and Chen, 2000): i.e., membrane and transverse shear play key roles when inducing mode II damage and the effects of bending is negligible in mode III damage.

3.4.3 Residual momentum and energy

The 'post-failure' residual momentum $\bar{I}_{ktr}$ and residual energy $\bar{E}_{ktr}$ of the two beams are plotted in Fig 3.11. Beyond the mode I→II transition, both $\bar{I}_{ktr}$ and $\bar{E}_{ktr}$ increase rapidly with I^*; this is particularly evident for impulsively-loaded beams. Shen and Jones (1992) found that the maximum loss of momentum for impulsively-loaded beams ($t_d = 0.01$ ms) occurs in the vicinity of the mode I→II transition and a rapid decrease in momentum loss by the beam occurs in mode

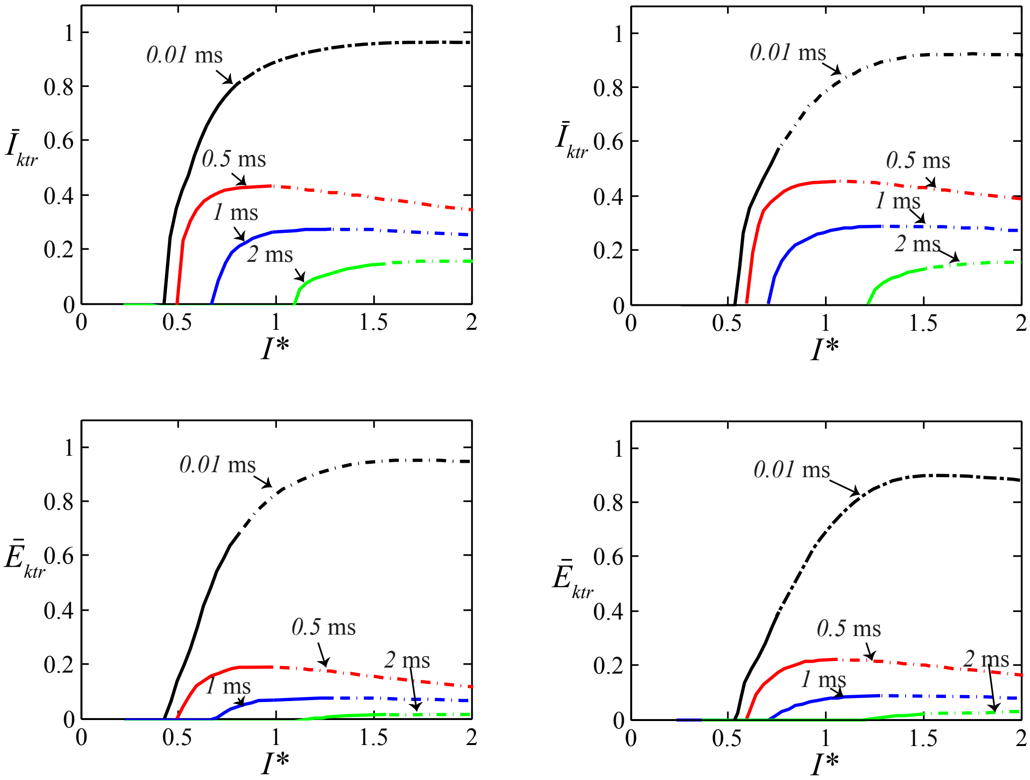

(a) Specimen-3
(0.203 m × 0.00635 m × 0.0254 m)

(b) Specimen-5
(0.203 m × 0.00947 m × 0.0254 m)

Figure 3.11: Non-dimensional residual momentum $\bar{I}_{ktr}$ and energy $\bar{E}_{ktr}$ for the two specimens shown in Fig 3.8. Black lines ($t_d = 0.01$ ms) correspond to impulsive loads. − denotes mode II; -.- denotes mode III.

II - this is consistent with the corresponding rise in residual momentum seen in Fig 3.11. Although a large impulse is generally needed to induce mode III failure by an impulsive load, a significant amount of residual kinetic energy and linear momentum remains in the beam which was also found in Jones (1976). For a given I^*, increasing the pulse duration t_d has the dramatic effect of reducing the residual momentum and energy of the beam failing in mode II and III. This is consistent with Fig 3.8 where the mid-span beam deflection W_0/H increases with t_d for a given I^*; hence, additional energy is absorbed through additional plastic work leading to a reduction in the residual momentum and energy.

3.4.4 Pulse shape

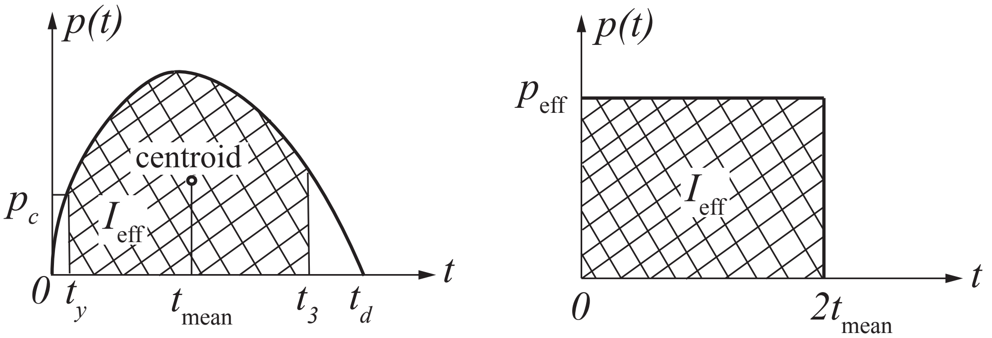

(a)

(b)

Figure 3.12: Youngdahl's equivalence parameters for a general pulse: (a) definitions for I_{eff} and t_{mean}; (b) an equivalent rectangular pulse.

All the previous analytical predictions were based on a linearly-decaying pressure pulse given by $p(t) = p_0(1 - t/t_d)$. Here, we will establish whether the approach of Youngdahl (1970, 1971) - see schematic in Fig 3.12 - may be used to eliminate the effects of pulse shape when investigating the dynamic response of elasto-plastic beams. Following Youngdahl (1970, 1971), an effective impulse (per unit length) is first obtained as follows:

$$I_{\text{eff}} = \int_{t_y}^{t_3} p(t)\mathrm{d}t, \tag{3.8}$$

where $p(t)$ is the actual pressure pulse, t_3 is time at the end of Phase III motion (see Chapter 2) and t_y corresponds to the time when the effective pressure (Eq. 3.9) equals the fully plastic collapse force per unit length of the beam, i.e. $p(t_y) = p_c = 4M_0/L^2$. From Eq. 3.8, an effective pressure may be defined as

$$p_{\text{eff}} = \frac{I_{\text{eff}}}{2t_{\text{mean}}} \tag{3.9}$$

where t_{mean} is the centroid of the effective pressure pulse in Fig 3.12a given by

$$t_{\text{mean}} = \frac{1}{I_{\text{eff}}} \int_{t_y}^{t_3} p(t)\mathrm{d}t. \tag{3.10}$$

It is worth noting that Youngdahl (1970, 1971) equivalence parameters were originally defined based on the rigid-perfectly plastic idealisation of dynamically loaded structures.

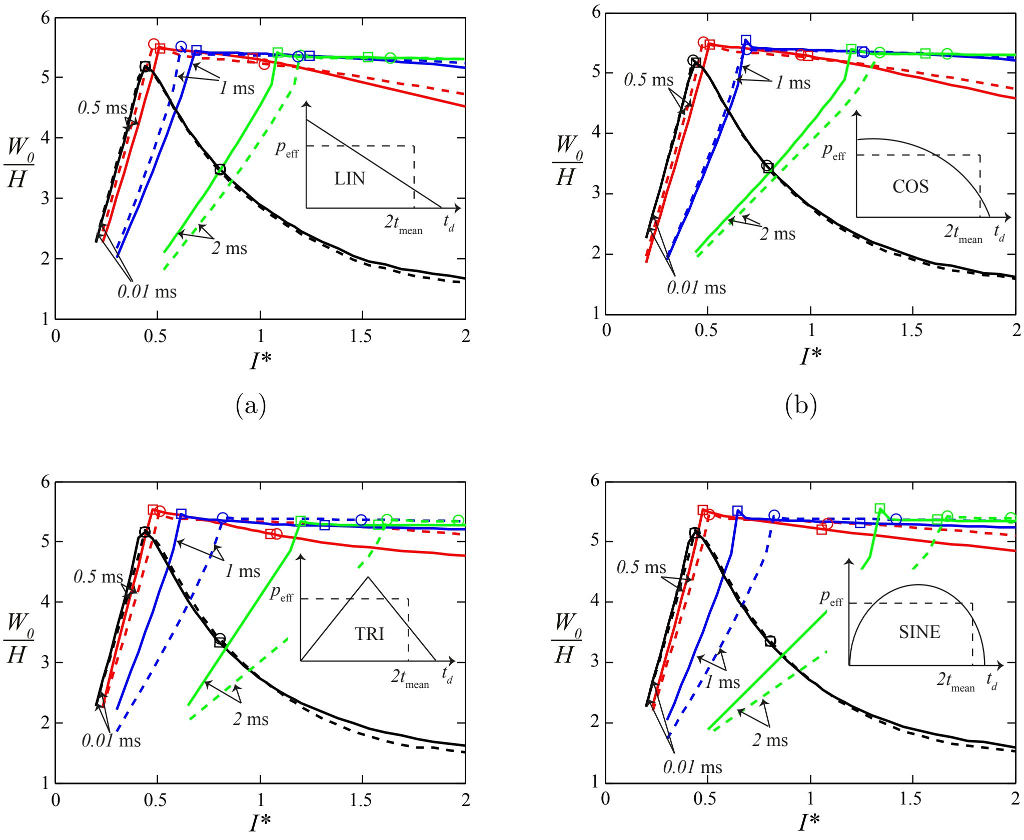

(a) (b)

(c) (d)

Figure 3.13: The predicted mid-span deflection at the cessation of beam motion (mode I) or at failure (mode II or III) for four different pressure pulses and their corresponding Youngdahl's equivalent. — analytical prediction by actual pressure pulse; – – – analytical predictions by Youngdahl's equivalent. Black lines ($t_d = 0.01$ ms) correspond to impulsive loads. □ and ○ are critical impulses predicted using the actual pulse and Youngdahl's equivalent.

A parametric study was carried out using different pulse shapes, viz. linearly-decaying (LIN), triangular (TRI), cosine (COS) and sine (SINE), of identical impulse per unit area ($\hat{I} = \int_0^{t_d} p(t)\mathrm{d}t/B$) impinging on a 0.203 m ($2L$) × 0.00635 m (H) × 0.0254 m (B) elasto-plastic beam. Figure 3.13 compares the predicted mid-span deflection at the cessation of beam motion (mode I) or at failure (mode II or III) of the aforementioned pulses to their corresponding Youngdahl's equivalent (Eqs. 3.9 and 3.10). The results show that Youngdahl's approach gives an excellent approximation of the mid-span deflection in all three modes for impulsive loadings ($t_d = 0.01$ ms). However, this is not generally the case if the loading is non-impulsive. For monotonically decaying pressure pulses (LIN and COS) that are non-impulsive - see Figs 3.13a and 3.13b - a reasonable agreement is observed up until $t_d = 1$ ms beyond which significant discrepancies arise. For non-monotonic pulses (TRI and SINE), the discrepancies between the actual pulse and its Youngdahl's equivalent increases dramatically with t_d. The discrepancies arise because Youngdahl's equivalence parameters were defined based on a rigid, perfectly-plastic idealisation of the loaded structures. Hence, the effective impulse I_{eff} in Eq. 3.8 does not account for contributions from the elastic response, i.e. it ignores $\int_0^{t_y} p(t)\mathrm{d}t$, which leads to an under-prediction of the mid-span deflection in mode I.

3.5 Conclusions

The response of elasto-plastic beams to impulsive and non-impulsive loadings were investigated in this chapter. Predictions by the current analytical and FE models were shown to be in good agreement with the experimental results of Menkes and Opat (1973). Excellent agreement between the predictions were also seen for elasto-plastic beams subjected to non-impulsive loads.

Key findings on the effects of pulse duration on the dynamic response of elasto-plastic beams can be summarised as follows: (i) Mode I deflection reduces with increasing pulse duration for a given dimensionless impulse I^* whilst the reverse occurs for the deflection in mode II; (ii) At the transition between mode I and II, the mid-span displacement is insensitive to pulse duration t_d; (iv) Mode III deflection under non-impulsive loads are considerably higher than its corresponding impulsive counterpart at the same I^*; (iii) An increase in the pulse duration

t_d delays the transitions (I→II and II→III) between deformation modes; (v) Increasing the pulse duration t_d leads to a reduction in the non-dimensional shear energy $\bar{E}_S^s$ but an increase in the non-dimensional membrane energy $\bar{E}_S^m$ at the same I^*; (vi) Increasing the pulse duration t_d decreases the residual momentum and energy of the beam in modes II and III.

It was also shown that Youngdahl (1970, 1971) approach is successful eliminating the dependence of the mid-span deflection of elasto-plastic beams to pulse shape effects for monotonically decaying, impulsive and non-impulsive, loadings. However, the same would under-predict the mode I mid-span deflection if the loading is non-impulsive and non-monotonically decaying (such as triangular and sine pulses).

Chapter 4

Fluid-structure interaction in deep underwater blasts

4.1 Introduction

The beneficial effects of FSI in reducing the impulse transmitted to a monolithic structure - although the momentum it acquires depend on its inertia - have been recognised for deep underwater explosions since Taylor (1941). In the acoustic range where nonlinear compressibility of the fluid medium is negligible, the transmitted impulse is proportional to a non-dimensional parameter (better known as the FSI index) which is independent of the blast intensity: a direct consequence of the linearity assumption since the reflected pressure profile scales linearly with its corresponding incident values. This 'peculiar' property has been extensively exploited to design sandwich panels that are better able to resist impulsive loads in comparison to monolithic plates of equivalent weight, leading to greater blast resistance: see Fleck and Deshpande (2004), Xue and Hutchinson (2004), Deshpande and Fleck (2005), Tilbrook et al. (2009), McShane et al. (2007), McShane et al. (2010) and Mori et al. (2007), to name a few.

Understanding how cavitation fronts (breaking and closing fronts) develop and evolve is paramount since the impulse imparted by blast waves to submerged structures are directly affected by it. Schiffer et al. (2012) modelled the 1D shock response of a rigid plate backed against a linear spring in contact with pressurised water on either, or both, side(s); their predictions were shown to be in good agreement with measurements from shock-tube experiments in Schiffer and Tagarielli (2013). Their results revealed that increasing hydrostatic pressure reduces the imparted impulse since it moves the point of incipient cavitation away from the structure. Furthermore, sensitivity analysis found that reducing plate mass does not always lead to a reduction in the transmitted impulse whilst increasing the supporting stiffness always will.

More recently, experiments carried out by Schiffer and Tagarielli (2015) showed that a local cavitation zone may arise due to flexural wave propagation in the plate, leading to a double-cavitation event. However, our current state of knowledge on FSI for monolithic structures remains grounded in results based on a rigid free-standing 'structure' (more precisely, a rigid body undergoing an unconstrained rectilinear motion); this was recently extended to elastic 'structures' with the introduction of a linear spring backing against the rigid plate. However, little is known of how large deformation (beyond linear-elasticity), the fixing conditions at the supports and structural *failure* of monolithic structures (exemplified by the complete detachment of a structure from its supports) affect previously known results; in particular, their implications on the energy and momentum transfer to an actual deforming structure. In this chapter, the topic of fluid-structure interaction (FSI) in deep underwater blasts will be re-visited for an elasto-plastic monolithic beam system, developed in Chapter 2, to elucidate the aforementioned. The analytical predictions will be shown to be in excellent agreement with results from 3D finite element simulations.

4.2 Coupling of fluid and structure

Consider a rightward-propagating planar wave that travels at a constant speed c_w(=1498 m/s) in a fluid of density ρ_w(=1000 kg/m^3), and impinging normally on the structural beam system shown schematically in Fig 4.1. It is convenient to define a spatial coordinate Z in the un-deformed configuration with $Z = 0$ corresponding to the location of the fluid and structure interface, i.e. $Z = z+H/2$. Assuming that the blast wave is exponentially decaying with a peak pressure p_s

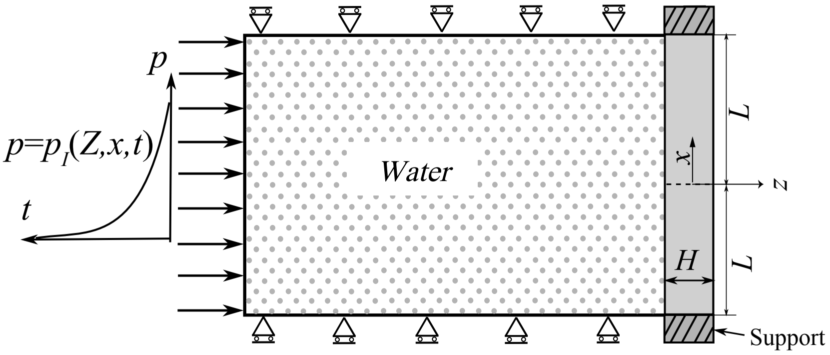

Figure 4.1: Schematic of an exponentially decaying wave propagating to the right towards a clamped elasto-plastic beam system.

and time constant t_i, then the incident pressure wave at any arbitrary point (of coordinate Z and x) at the time t may be expressed as (Taylor, 1941)

$$p_I(Z,t) = p_s e^{-(t-Z/c_w)/t_i}. \tag{4.1}$$

The pulse duration for the incident pressure wave is assumed to be infinitely large, i.e. $t_d = \infty$. If the target structure is rigid and fixed in space, then the reflected wave would be

$$p_{R1}(Z,t) = p_s e^{-(t+Z/c_w)/t_i} \tag{4.2}$$

corresponding to a perfect reflection of the incident wave in the negative Z direction. Since the beam is not rigid, the impingement of the incident pressure wave on this interface sets the beam in motion, i.e. the beam accquires a velocity field $\dot{W}(x,t)$. Compatibility dictates that the wetted surface of beam and the fluid particles at its interface possess the same velocity $\dot{W}(x,t)$, provided cavitation is absent (everywhere) at the fluid and structure interface. The beam motion results in a rarefaction wave (travelling in negative Z-direction) of magnitude

$$p_{R2}(Z,x,t) = -\rho_w c_w \dot{W}(x, t+Z/c_w). \tag{4.3}$$

It merits comment that the reflection of planar waves off a curved interface would render the exact formulation of the fluid pressure field too complicated to quantify. Following Schiffer and Tagarielli (2014), it is assumed here that the reflected waves remain planar and travel in the negative Z-direction, without affecting the pressure and particle velocity fields perpendicular to the incident angle. Thus, the net water pressure $p(Z, x, t)$ due to the incident and reflected waves is given by

$$p(Z, x, t) = p_I + p_{R1} + p_{R2} = p_s \left[e^{-(t - Z/c_w)/t_i} + e^{-(t + Z/c_w)/t_i} \right] - \rho_w c_w \dot{W}(x, t + Z/c_w). \quad (4.4)$$

The interface pressure (at $Z = 0$) is, therefore,

$$p_{\mathrm{Int}}(x, t) = p(Z = 0, x, t) = 2p_s e^{-t/t_i} - \rho_w c_w \dot{W}(x, t). \quad (4.5)$$

Substituting $p_{\mathrm{Int}}(x, t)$ into Eq. 2.28 and rearranging gives the governing ordinary differential equations describing the beam motion as follows:

$$\sum_{j=1}^{n} M_{ij} \ddot{w}_j + \frac{\partial V}{\partial w_i} = B \int_0^L p_{\mathrm{Int}}(x, t) \phi_i(x) \mathrm{d}x, \quad i = 1, 2, ..., n. \quad (4.6)$$

4.2.1 Limitations of the present FSI model

The tensile term (p_{R2} in Eq. 4.3) may, under certain circumstances, cause the fluid pressure to drop below zero at some point in time within the fluid domain, giving rise to a cavitation event. Following cavitation, the pressure field in the fluid is given by a superposition of two breaking fronts, one travelling towards the structure (positive Z direction) and the other away (negative); this generates an expanding pool of cavitated liquid (Kennard, 1943). Schiffer et al. (2012) identified two cavitation types (or régimes) for underwater blast loading of rigid-plate supported by a linear spring that depends on the fluid conditions in the layer between the structure and the expanding cavitation zone. *Type I* cavitation occurs if a breaking front (travelling in the positive Z direction), arrests before reaching the fluid-structure interface, reverses its motion and becomes a closing front. *Type II* cavitation occurs if the breaking front (travelling in positive Z direction) reaches the fluid-structure interface and causes cavitation at the interface. In the present study, *Type II* cavitation will occur if the condition

(Schiffer et al., 2012)

$$p_{\mathrm{Int}}(x,t) = 0 \tag{4.7}$$

is met. Since Schiffer et al. (2012) showed that the structure might acquire greater transmitted impulse in *Type I* than in *Type II*, the former would be of greater concern since the objective of this work is to evaluate the limits of structural performance for a given underwater blast loading.

In a *Type I* cavitation, several authors (Schiffer et al., 2012; Schiffer and Tagarielli, 2014, 2015) found that the pressure wave (rarefaction p_{R2} and reflected p_{R1}) emanating from the fluid-structure interface approaches the closing front and eventually reflects back towards the fluid-structure interface as a positive pressure pulse. It was noted by Schiffer et al. (2012) that this positive pressure pulse acts continuously on their rigid plate which reduces to zero after a finite duration. As a consequence, it must contribute to the impulse transmitted to the structure and in cases where the mass and stiffness of the structure are high, the maximum transmitted impulse can even exceed twice the incident impulse $I_i = p_s t_i$. However, detailed three-dimensional (3D) finite element simulations (to be presented later in Section 4.4) will show that for elasto-plastic beams deforming in any modes of deformation, the contribution of the reflection wave (from the closing front) during *Type I* cavitation does not significantly affects the structural performance in terms of the maximum mid-span deflection, maximum momentum, maximum transmitted impulse, maximum kinetic energy and maximum transmitted energy. Therefore, it is reasonable to neglect the influence of the reflection wave from the closing front in the current analytical model.

4.3 Finite element (FE) model

Three-dimensional (3D) FE calculations were performed using the commercially software ABAQUS/ Explicit®. The FE model, shown schematically in Fig 4.2, consists of a water column $L_w \times L \times B$ above the supported beam. Only one-half of the beam and water column are modelled since reflective symmetry exists on the plane bounded by $x = 0$, $-B/2 \leq y \leq B/2$ and $-H/2 - L_w \leq$

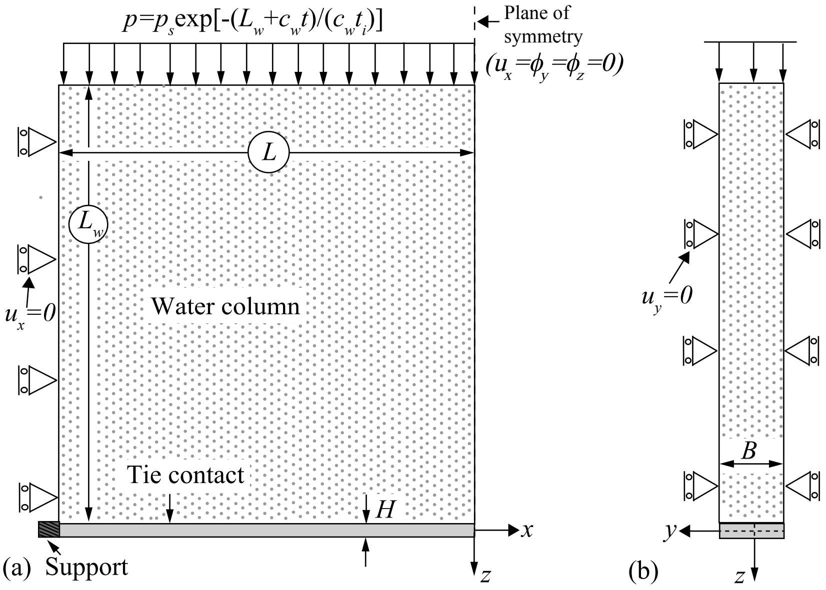

Figure 4.2: Schematic of clamped beam subjected to an exponentially decaying pressure pulse in FE: (a) front view and (b) side view.

$z \leq H/2$. The elasto-plastic beam is supported by a modified boundary condition, as described previously in Section 3.2.1. Horizontal displacement u_x for the left boundary of the water column ($u_x = 0$ at $x = -L$, $-B/2 \leq y \leq B/2$, $-H/2 - L_w \leq z \leq -H/2$) is constrained as does the vertical displacement u_y on the front ($u_y = 0$ at $-L \leq x \leq 0$, $y = B/2$, $-H/2 - L_w \leq z \leq -H/2$) and back ($u_y = 0$ at $-L \leq x \leq 0$, $y = -B/2$, $-H/2 - L_w \leq z \leq -H/2$) boundary of the water column - see Fig 4.2. An exponentially decaying pressure pulse, given by Eq. 4.1, is applied to the top of the water column. Tie constraints are applied between the wetted edge of the beam and fluid.

The beam modelled in this chapter has dimension of 0.5 m (L) × 0.1 m (H) × 0.1 m (B). The length of water column L_w is sufficient long to ensure the reflected wave from the top boundary does not reach the structure over the duration of the calculation (Schiffer and Tagarielli, 2014, 2015). In the present study, $L_w/c_w t_i = 3$ is used to ensure that the water column is semi-infinite. Both the beam and water column are discretised using the 8-noded solid elements (C3D8R) with reduced integration and hour-glass control. In order to capture necking localisation, progressive damage and ductile fracture with acceptable fidelity, twelve elements are used through the beam thickness (H). Results of convergence studies, presented previously in Fig 3.3, has shown this to be sufficient. All C3D8R elements - used to discretise the water column and beam - are cubic with a size of 0.00833 m; consequently, the nodes of the water and solid meshes are coincident at the fluid-structure interface.

Details of the material properties and damage criterion of the elasto-plastic beam were given previously in Section 3.2.2. The water is modelled as an acoustic medium with density $\rho_w = 1000$ kg/m^3, wave speed $c_w = 1498$ m/s and bulk modulus $E_w = 2.244$ GPa. It is assumed to be linear elastic under compression, with zero tensile strength and zero shear modulus. A Mie-Gruneisen equation of state with a linear Hugoniot relation is used to model the linear elastic ratio between applied pressure $p(Z,t)$ and volumetric strain ϵ_V given by

$$p(Z,t) = \begin{cases} -E_w\epsilon_V = -c_w^2\rho_w\epsilon_V, & \epsilon_V < 0 \\ 0, \quad \epsilon_V \geq 0 \end{cases} . \tag{4.8}$$

Note that when $\epsilon_V \geq 0$, the pressure becomes zero and this leads to an onset of cavitation (Liang et al., 2007; McShane et al., 2007, 2010).

4.4 Comparison of analytical and FE predictions

To assess the fidelity of the analytical model, predictions for the average interface pressure, mid-span deflection, impulse and energy transfer will be compared to those from FE. The temporal history of the transmitted impulse per unit area $I^T(t)$, momentum per unit area $I^K(t)$, transmitted energy per unit area $E^T(t)$ and kinetic energy per unit area $E^K(t)$ of the beam are defined, respectively, as

$$I^T(t) = \int_0^t \tilde{p}_{\text{Int}}(t)\mathrm{d}t, \quad I^K(t) = \frac{\rho H}{L}\int_0^L \dot{W}(x,t)\mathrm{d}x,$$
$$E^T(t) = \frac{1}{BL}\int_0^L p_{\text{Int}}(x,t)W(x,t)\mathrm{d}x, \quad E^K(t) = \frac{\rho H}{2L^2}\int_0^L \dot{W}^2(x,t)\mathrm{d}x. \tag{4.9}$$

Note that the average interface pressure is given by

$$\tilde{p}_{\text{Int}}(t) = \frac{1}{L}\int_0^L p_{\text{Int}}(x,t)\mathrm{d}x. \tag{4.10}$$

Time t is measured from the instant when the incident pressure wave arrives at the fluid and structure interface. The impulse and energy components in Eq. 4.9 are normalised by the incident impulse per unit area I_i and incident energy per unit area E_i given by (Taylor, 1941)

$$I_i = p_s t_i \quad \text{and} \quad E_i = p_s^2 t_i/\rho_w c_w. \tag{4.11}$$

Unless otherwise specified, a time constant $t_i = 2$ ms has been used for all calculations in this chapter.

Figures 4.3a, 4.3b and 4.3c compare the analytical and FE predictions for mode I, II and III deformations, respectively. Pressure contour plots predicted by FE (to be presented later in Fig 4.4) confirm that a *Type I* cavitation event (i.e. the breaking front travelling in the positive Z-direction, always arrests before it reaches the fluid-structure interface and inverts its motion as a closing front) occurs in all the cases shown in Fig 4.3. Cavitation occurs at $t_c/t_i = 0.5$, $t_c/t_i = 0.47$ and $t_c/t_i = 0.45$ in Figs 4.3a, 4.3b and 4.3c, respectively. For beams deforming in mode I, Fig 4.3a shows that its non-dimensional average interface pressure $\tilde{p}_{\text{Int}}/p_s$ initially decreases before attaining a peak value at time $t = t_3$ (when the beam reaches its maximum mid-span deflection); this is followed by a monotonic reduction in interface pressure. Beyond $t > t_3$, the FE model predicts that $\tilde{p}_{\text{Int}}/p_s$ remains positive until $t/t_i = 5.9$ - this is in agreement with Schiffer et al. (2012). The analytical model under-predicts the maximum transmitted impulse in mode I by up to 13.4% since it neglects the additional loading from the reflected wave arising from the closing front. Complete detachment occurs shortly after cavitation in Figs 4.3b and 4.3c which explains why it is acceptable to neglect the effects of the reflected wave from the closing front in the subsequent structural response. In general, the predicted interface pressure, mid-span deflection, impulse and energy exchange are in good agreement with those from FE for all three modes of deformation.

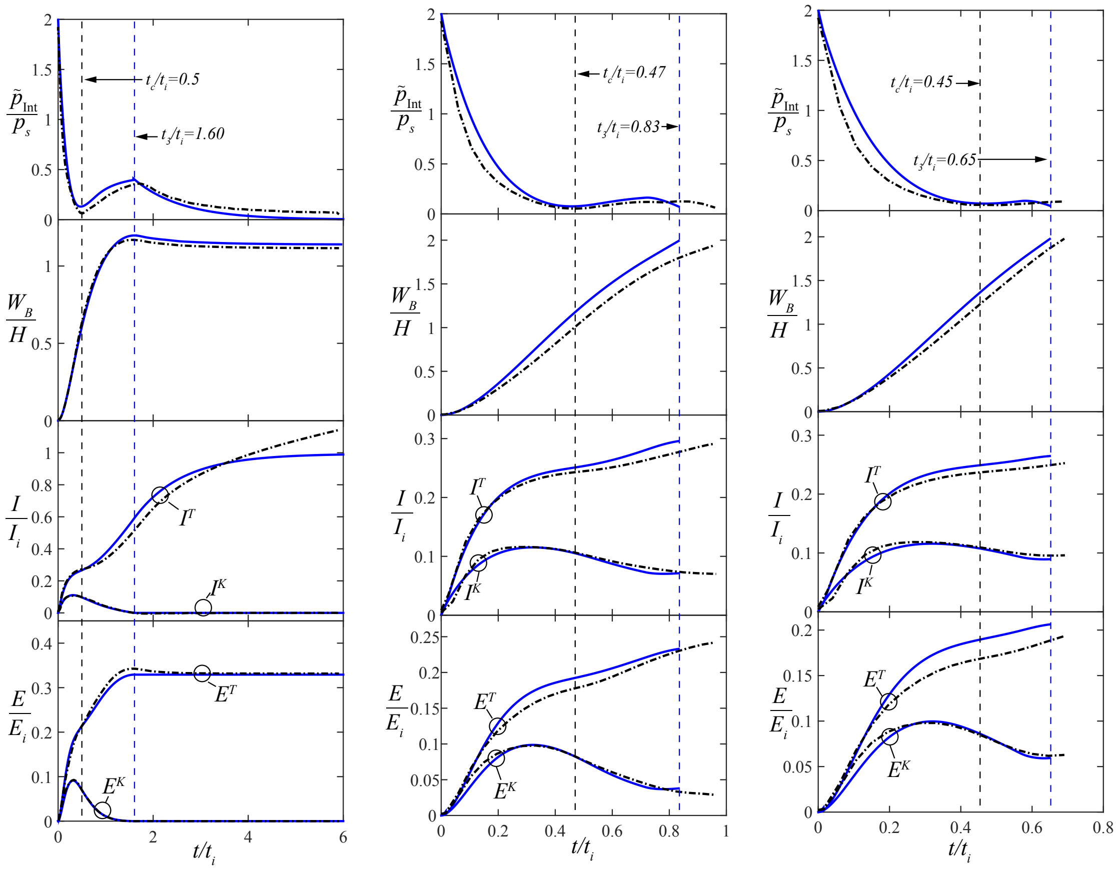

(a) Mode I (b) Mode II (c) Mode III

Figure 4.3: Analytical and FE prediction of the non-dimensional interface pressure, mid-span deflection, impulse transfer and energy exchange for 0.5 m (L) × 0.1 m (H) × 0.1 m (B) beam deforming in different modes subjected to three different exponentially decaying pressure pulses of identical time constant $t_i = 2$ ms and a peak pressure of (a) $p_s = 50$ MPa, (b) $p_s = 100$ MPa and (c) $p_s = 120$ MPa. — current analytical predictions; -.- current FE predictions. t_c and t_3 denote the time when cavitation first occurs and when the beam reaches maximum deflection, respectively.

The impulse and energy transferred to the beam, plotted in Fig 4.3, can be summarised as follows: (1) In mode I, the average interface pressure beyond $t > t_3$ does not further contribute to the transmitted energy E^T. This is because the beam now responds in an elastic manner with deflection which decreases slightly before reaching a plateau; (2) In modes II and III, both the transmitted impulse I^T and transmitted energy E^T reach a maximum at $t = t_3$ following complete detachment from the supports; (3) The maximum momentum I^K and kinetic energy E^K are reached before the onset of cavitation at $t = t_c$ for all three modes, this agrees with analytical predictions by Schiffer et al. (2012); (4) The maximum transmitted impulse is significantly higher in mode I than in modes II and III because a considerable amount of impulse is transmitted to the beam during elastic rebound; and, (5) The maximum transmitted impulse and energy are higher in mode II than III since t_3 for mode III is smaller than mode II.

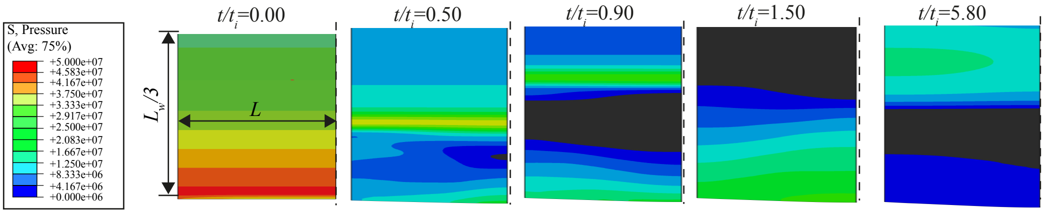

(a) Mode I

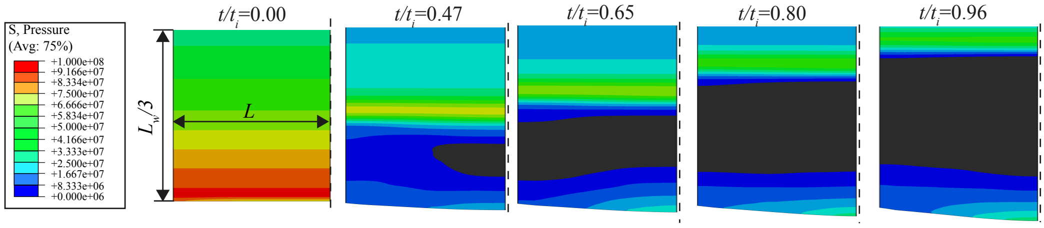

(b) Mode II

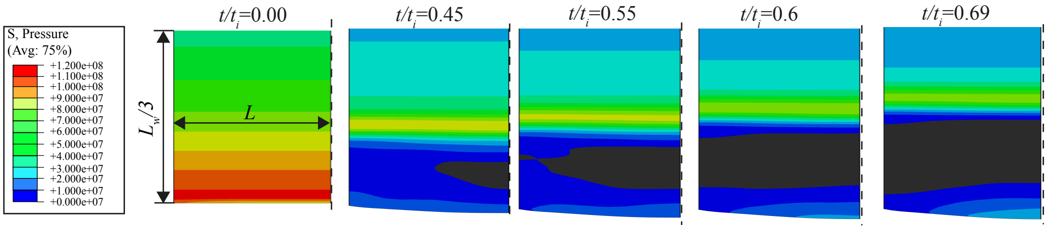

(c) Mode III

Figure 4.4: FE predictions of fluid pressure field at five selected times corresponding to the cases shown in Figs 4.3a, 4.3b and 4.3c, respectively. Black denotes cavitated water.

To gain an insight into the cavitation process, pressure contour maps predicted by FE are shown in Fig 4.4 for five selected time frames (corresponding to the elasto-plastic beam and loading parameters of Fig 4.3). Cavitation first occurs at $t_c/t_i = 0.50$ (mode I), $t_c/t_i = 0.47$ (mode II) and $t_c/t_i = 0.45$ (mode III). This is caused by the tensile wave (Eq. 4.3) which is generated as a consequence of the rapid motion of the beam and is in line with experimental observations made by Schiffer and Tagarielli (2015) for circular plates. All the cases shown in Fig 4.4 correspond to *Type I* cavitation since the breaking front arrests and inverts its motion as a closing front before reaching the fluid and structure interface.

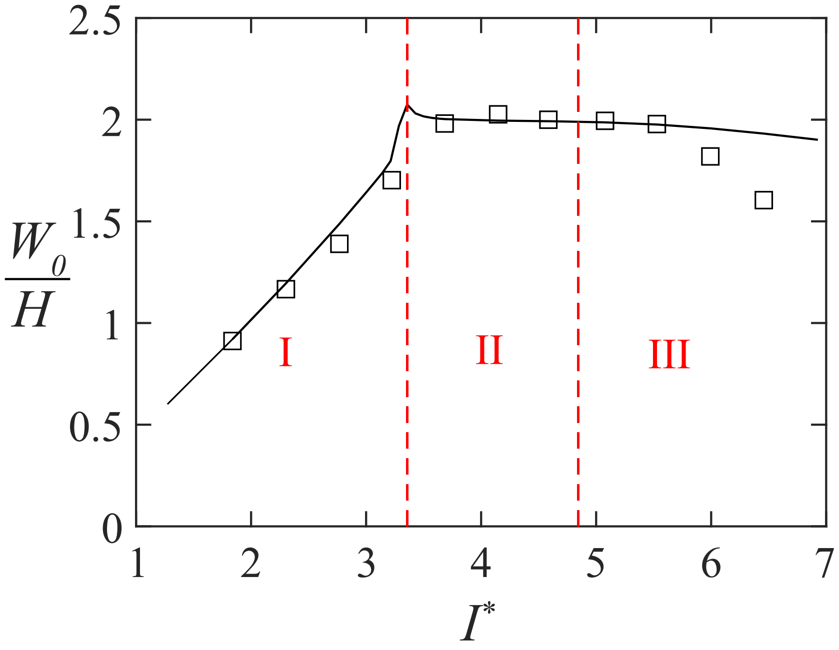

Figure 4.5: Variations of the non-dimensional mid-span deflection W_0/H with non-dimensional impulse I^*. I, II and III indicate the three distinct damage modes predicted by the current analytical model. — current analytical model; □ current FE predictions.

Predictions by FE and the current analytical model are now compared for a range of incident impulses, with a focus on the maximum mid-span deflection, transmitted impulse and energy. The maximum non-dimensional transmitted impulse $\bar{I}^T$, momentum $\bar{I}^K$, transmitted energy $\bar{E}^T$ and kinetic energy $\bar{E}^K$ of the elasto-plastic beam are defined as follows:

$$\bar{I}^T = \max_{0 \le t/t_i < \infty} [I^T(t/t_i)/I_i], \quad \bar{I}^K = \max_{0 \le t/t_i < \infty} [I^K(t/t_i)/I_i],$$
$$\bar{E}^T = \max_{0 \le t/t_i < \infty} [E^T(t/t_i)/E_i], \quad \bar{E}^K = \max_{0 \le t/t_i < \infty} [E^K(t/t_i)/E_i]. \quad (4.12)$$

Figure 4.5 shows an excellent agreement for the maximum mid-span deflection W_0/H, at either the point of cessation of motion or failure (if complete detachment from the supports had occurred), for all three modes. Note that the non-dimensional impulse I^* is given by Eq. 3.3. Both the current FE and analytical models correctly predict a reduction in W_0/H with increasing I^* in modes II and III - this trend is also observed in Fig 3.7. Figure 4.6 compares the non-dimensional impulse ($\bar{I}^T$ and $\bar{I}^K$) and energy ($\bar{E}^T$ and $\bar{E}^K$) terms with the corresponding FE predictions. In general, the analytical predictions agree well with its FE counterpart despite the under-prediction of $\bar{I}^T$ - by up to 13.4% - in mode I. Again, this discrepancy arises because the analytical model neglects the additional impulse transmitted by the reflection wave from the closing front. Key features of the results shown in Fig 4.6 are as follows: (1) There is a sharp decrease in $\bar{I}^T$ following a transition from mode I→II because a significant portion of impulse is transmitted to the beam during elastic rebound in mode I; (2) Both the maximum transmitted impulse $\bar{I}^T$ and energy $\bar{E}^T$ reduce monotonically with I^* in modes II and III since the time it takes for complete detachment to occur reduces with I^*; and (3) The maximum momentum $\bar{I}^K$ and kinetic energy $\bar{E}^K$ of the beam are relatively insensitive to I^*.

4.5 Effects of FSI on 'elasto-plastic' and 'rigid free-standing' beams

In this section, the analytical model is employed to investigate the effects of FSI for a *Type I* cavitation event. Parametric studies were performed to evaluate the sensitivity of the maximum impulse ($\bar{I}^T$) and energy ($\bar{E}^T$) transfer to aspect ratio L/H and β_w ($\triangleq \rho_w c_w t_i/\rho H$ - Taylor's FSI index). Results from

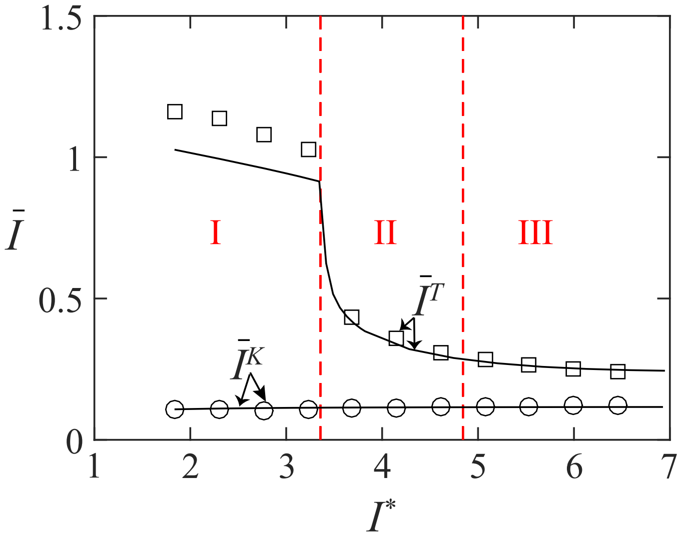

(a)

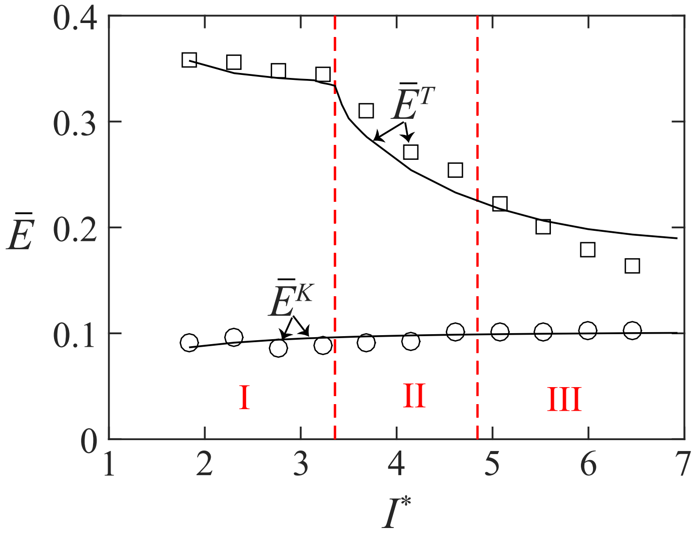

(b)

Figure 4.6: Variations of the non-dimensional maximum impulse and energy acquired with non-dimensional impulse I^*. I, II and III indicate the three distinct damage modes predicted by the current analytical model. — current analytical model; □ and ○ current FE predictions.

rigid free-standing beams of an equivalent mass per unit area are also included for comparison where the maximum transmitted impulse and energy - superscript F

denotes free-standing - are, respectively, given by (Taylor, 1941)

$$\bar{I}^F = 2\beta_w^{-(\beta_w/\beta_w - 1)} \tag{4.13}$$

and

$$\bar{E}^F = 2\frac{(1 - e^{-\beta_w})^2}{\beta_w}. \tag{4.14}$$

In the parametric studies to be presented, it is worth noting the following: (1) the non-dimensional maximum transmitted impulse $\bar{I}^F$ and energy $\bar{E}^F$ of rigid free-standing beams are independent of peak incident pressure p_s and aspect ratio L/H but depends only on β_w; (2) both the 'elasto-plastic' and 'rigid, free-standing' beams have identical mass per unit area given by β_w; and, (3) cavitation always occurs at the fluid and structure interface for free-standing beams at time $t_c = t_i \ln(\beta_w)/(\beta_w - 1)$ whilst it does not for elasto-plastic beams (*Type I* cavitation); hence, the fluid-structure interaction time for an elasto-plastic beam is always considerably longer compared to a free-standing one of the same mass per unit area.

4.5.1 Mode I

The solid blue lines in Figs 4.7a and 4.8a denote the non-dimensional maximum transmitted impulse ($\bar{I}^T$ and $\bar{I}^F$) and the broken black lines denote the non-dimensional maximum transmitted energy ($\bar{E}^T$ and $\bar{E}^F$). A peak incident overpressure of $p_s = 30$ MPa is used throughout so that the elasto-plastic beams always deform in mode I. Figure 4.7a plots the variation of the non-dimensional maximum impulse and energy terms as a function of L/H (for a constant $\beta_w = 21.7$). For elasto-plastic beams, $\bar{I}^T$ reduces monotonically with L/H while $\bar{E}^T$ does not. The reason is evident by comparing two beams of different L/H, denoted by ① and ② in Fig 4.7b. The beam with a higher L/H, i.e. beam ②, has less average interface pressure $\tilde{p}_{\text{Int}}/p_s$ but higher mid-span deflection W_B, leading to a smaller $\bar{I}^T$ and non-monotonic decreasing $\bar{E}^T$. Figure 4.8a plots the maximum non-dimensional impulse and energy to FSI index β_w with a constant $L/H = 10$. It shows that $\bar{I}^T$ increases monotonically with increasing β_w (less mass per unit area) but $\bar{E}^T$ does not. Again, the reason is that the average

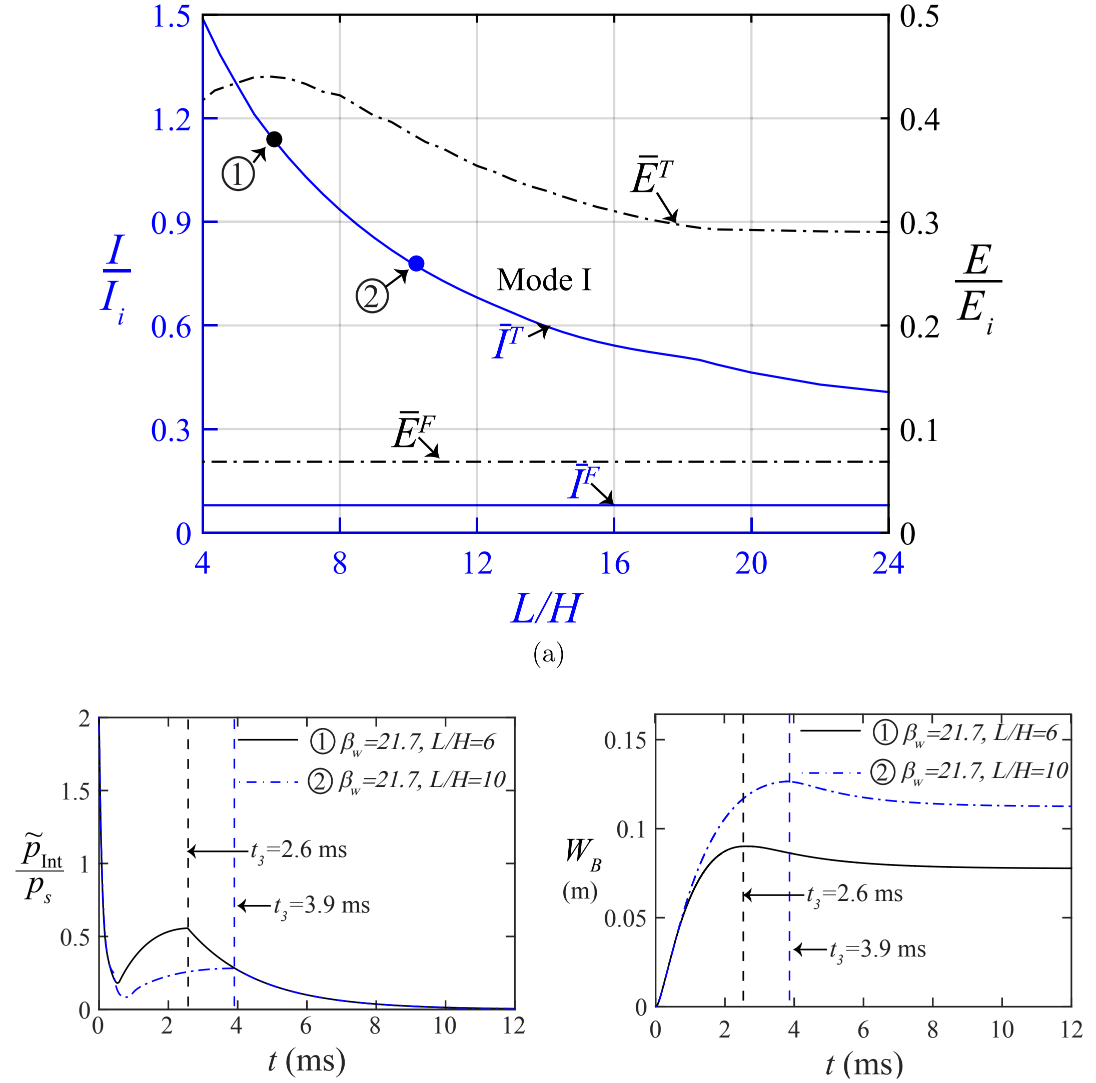

(a)

(b)

Figure 4.7: (a) Analytical prediction of non-dimensional maximum impulse (— corresponds to $\bar{I}^T$ and $\bar{I}^F$) and energy (–.– corresponds to $\bar{E}^T$ and $\bar{E}^F$) for elasto-plastic beams of identical cross-section, $H = B = 0.05$ ($\beta_w = 21.7$), deforming in mode I; and (b) Comparison of the normalised temporal average interface pressure $\tilde{p}_{\text{Int}}(t)/p_s$ and temporal mid-span deflection $W_B(t)$ for beams ① and ② in Fig 4.7a. Beam ① is 0.3 m (L) × 0.05 m (H) × 0.05m (B); beam ② is 0.5 m (L) × 0.05 m (H) × 0.05 m (B).

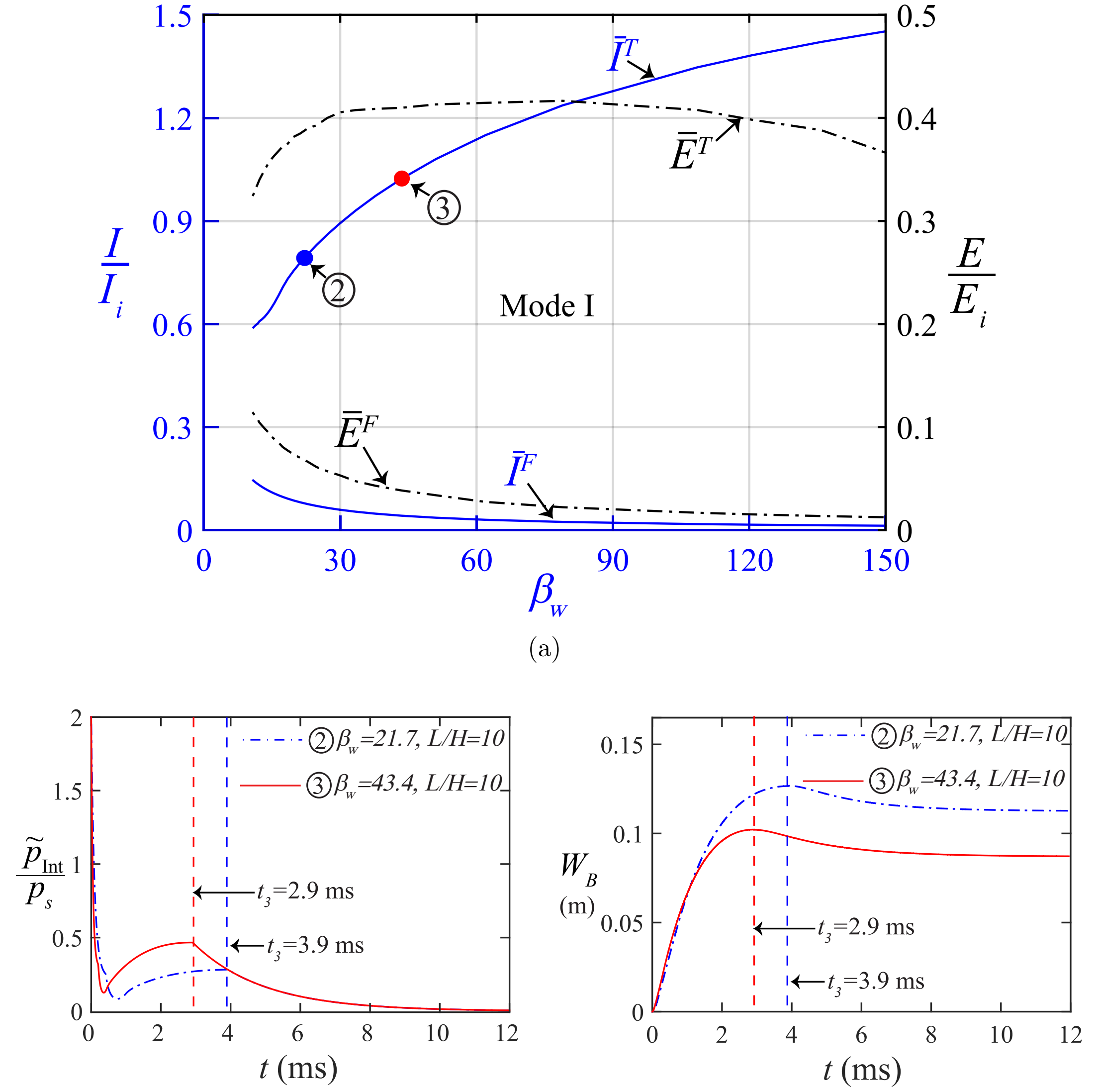

(a)

(b)

Figure 4.8: (a) Analytical prediction of maximum impulse (— corresponds to $\bar{I}^T$ and $\bar{I}^F$) and energy (–.– corresponds to $\bar{E}^T$ and $\bar{E}^F$) for elasto-plastic beams with identical aspect ratio $L/H = 10$ deforming in mode I; and (b) Comparison of analytical normalised temporal average interface pressure $\tilde{p}_{\text{Int}}(t)/p_s$ and temporal mid-span deflection $W_B(t)$ for beams ② and ③ in Fig 4.8a. Beam ② is 0.5 m (L) × 0.05 m (H) × 0.05 m (B) ($\beta_w = 21.7$); beam ③ is 0.25 m (L) × 0.025 m (H)× 0.025 m (B) ($\beta_w = 43.4$).

interface pressure $\tilde{p}_{\mathrm{Int}}/p_s$ is higher but the mid-span deflection W_B is lower for beam with a higher β_w (less mass per unit area) - compare beam ③ to ② in Fig 4.8b. It is worth noting that in both Figs 4.7a and 4.8a, the elasto-plastic beams have significantly higher non-dimensional maximum transmitted impulse and energy compared to free-standing beams because, as alluded to earlier, the fluid-structure interaction time for elasto-plastic beams are significantly longer.

4.5.2 Mode II

Variations of the maximum non-dimensional impulse and energy terms against L/H and β_w for a peak incident overpressure of $p_s = 100$ MPa are shown in Figs 4.9 and 4.10 respectively. Note that all the elasto-plastic beams deform in mode II. Figure 4.9a plots the maximum non-dimensional impulse and energy terms, against the aspect ratio L/H with $\beta_w = 108.4$. Both $\bar{I}^T$ and $\bar{E}^T$ do not reduce monotonically with L/H. This is because as L/H increases - comparing ② to ① in Fig 4.9b - ② has a lower average interface pressure $\tilde{p}_{\mathrm{Int}}(t)/p_s$ and, consequently, takes longer to reach its maximum mid-span deflection and for complete detachment to occur.

Figure 4.10a shows the effect of mass per unit area, or β_w, on the non-dimensional impulse and energy terms for a fixed aspect ratio $L/H = 16$. It shows that both $\bar{I}^T$ and $\bar{E}^T$ reduce monotonically with β_w (or less mass per unit area). As opposed to Fig 4.9 increasing β_w - compare ② and ③ in Fig 4.9 - leads to a reduction in the average interface pressure $\tilde{p}_{\mathrm{Int}}(t)/p_s$ and a shorter time to reach maximum mid-span beam deflection and for complete detachment to occur. Although non-dimensional maximum transmitted impulse and energy for elasto-plastic beams in mode II are significantly less compared to those in mode I (see Fig 4.6 for an example), they are still considerably greater than those of free-standing beams, i.e. $\bar{I}^T > \bar{I}^F$ and $\bar{E}^T > \bar{E}^F$ as seen in both Figs 4.9 and 4.10.

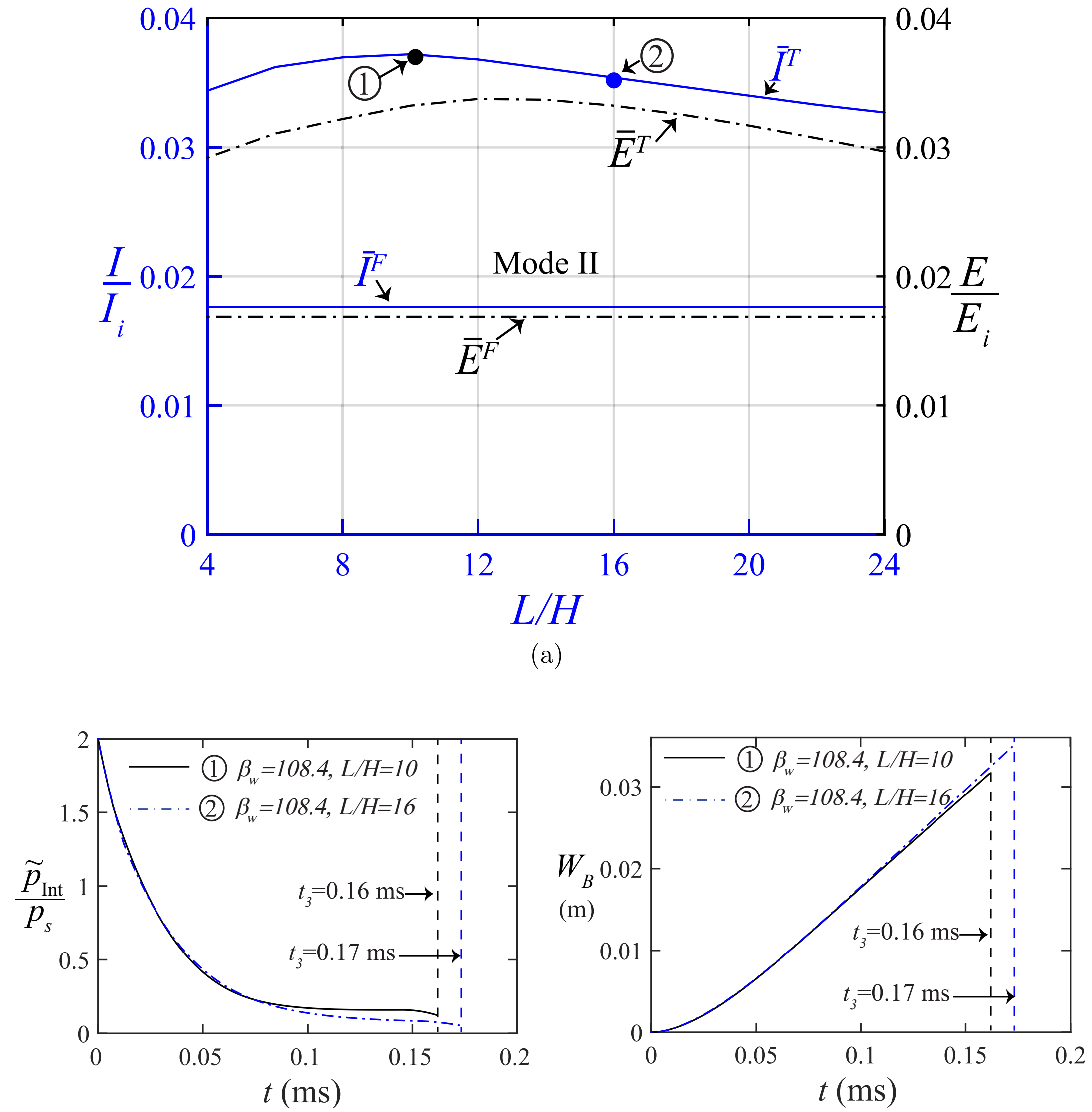

(a)

(b)

Figure 4.9: (a) Analytical prediction of non-dimensional maximum impulse (— corresponds to $\bar{I}^T$ and $\bar{I}^F$) and energy (–.– corresponds to $\bar{E}^T$ and $\bar{E}^F$) dissipation for elasto-plasitc beams in mode II with same beam cross-section, $H = B = 0.01$ m ($\beta_w = 108.4$) and (b) Comparison of analytical normalised temporal average interface pressure $\tilde{p}_{\text{Int}}(t)/p_s$ and temporal mid-span deflection $W_B(t)$ for beam ① and ② in Fig 4.9a. Beam ① has 0.10 m (L) × 0.01 m (H) × 0.01 m (B) ($\beta_w = 108.4$); beam ② has 0.16 m (L) × 0.01 m (H) × 0.01 m (B) ($\beta_w = 108.4$).

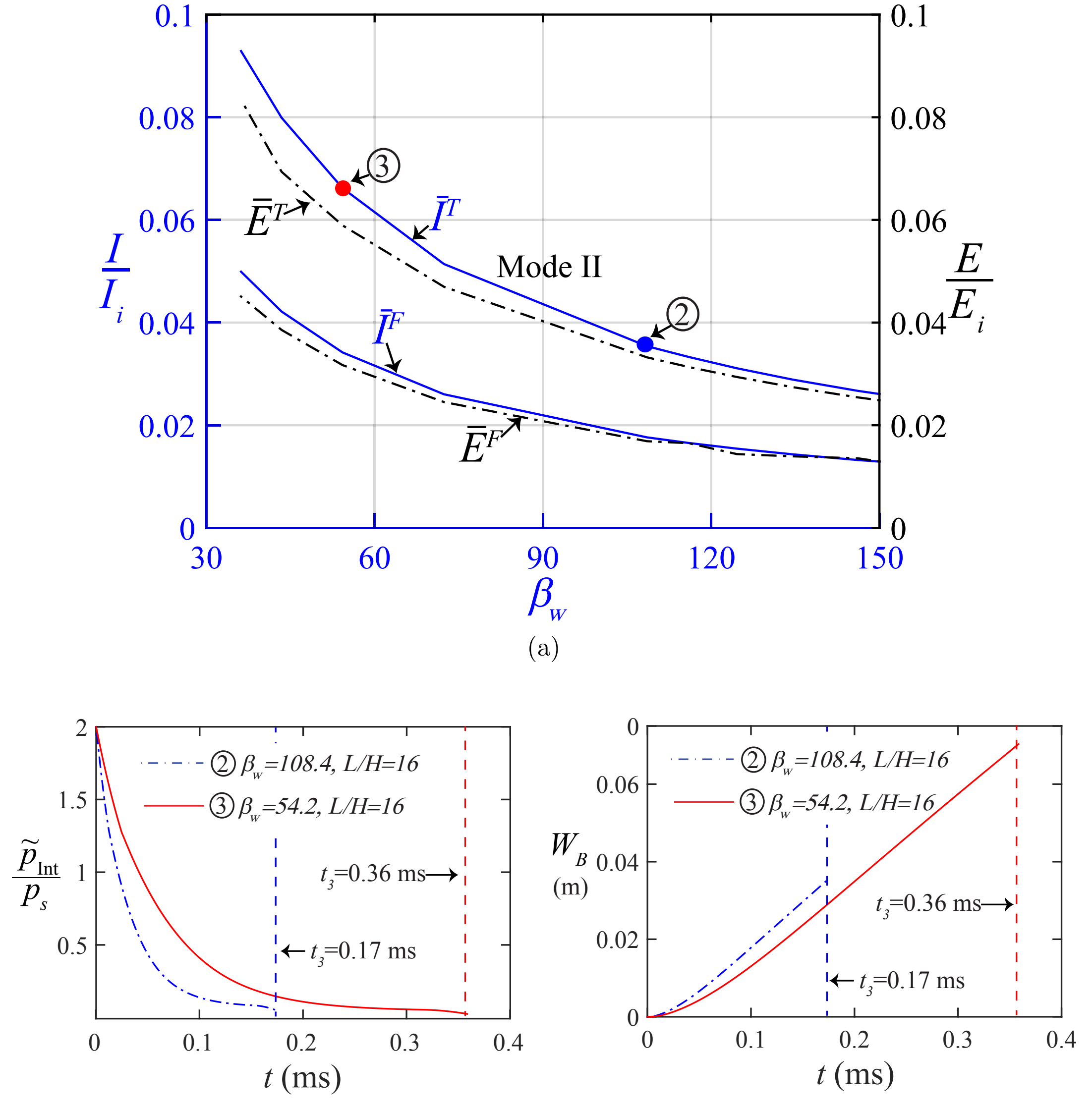

(a)

(b)

Figure 4.10: (a) Analytical prediction of non-dimensional maximum impulse (— corresponds to $\bar{I}^T$ and $\bar{I}^F$) and energy (–.– corresponds to $\bar{E}^T$ and $\bar{E}^F$) dissipation for elasto-plastic beams in mode II with the same aspect ratio $L/H = 16$; and (b) Comparison of analytical normalised temporal average interface pressure $\tilde{p}_{\text{Int}}(t)/p_s$ and temporal mid-span deflection $W_B(t)$ for beam ② and ③ in Fig 4.9a. Beam ② is 0.16 m $(L) \times 0.01$ m $(H) \times 0.01$ m (B) $(\beta_w = 108.4)$; and beam ③ is 0.32 m $(L) \times 0.02$ m $(H) \times 0.02$ m (B) $(\beta_w = 54.2)$.

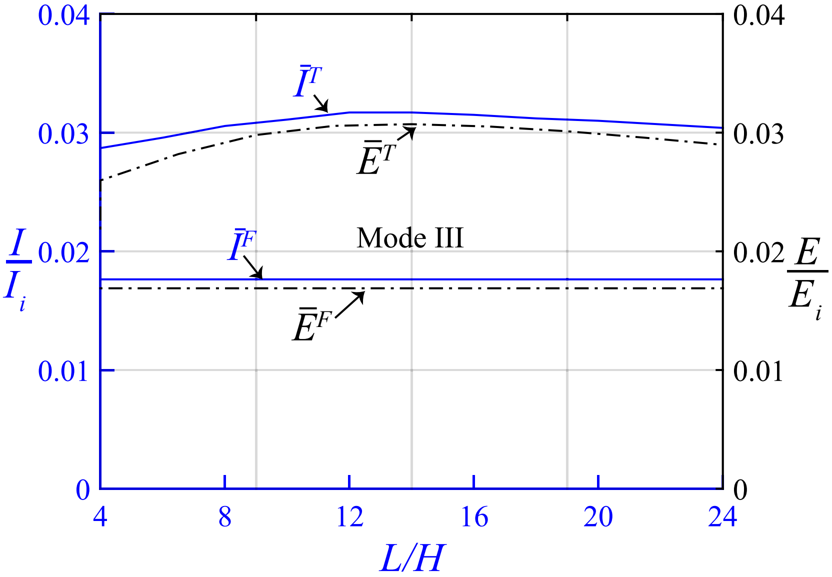

(a)

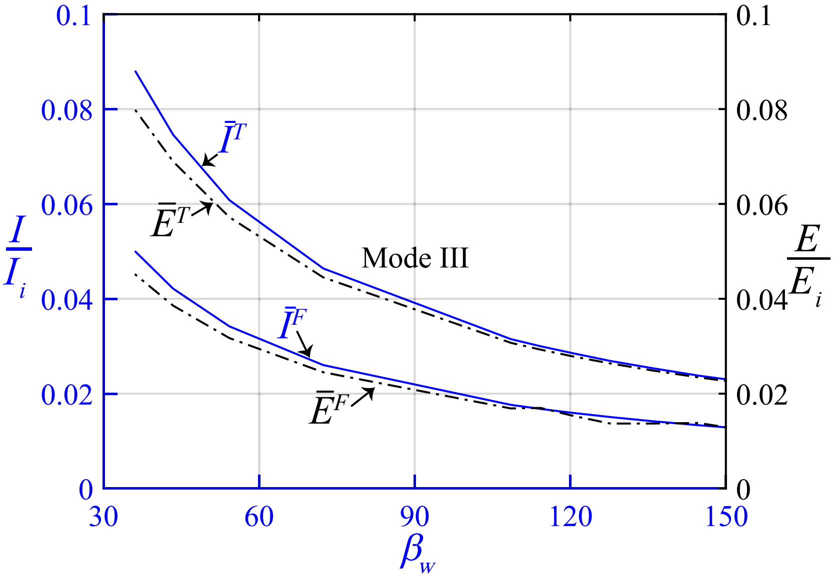

(b)

Figure 4.11: Analytical predictions of the non-dimensional maximum impulse (— corresponds to $\bar{I}^T$ and $\bar{I}^F$) and energy (–.– corresponds to $\bar{E}^T$ and $\bar{E}^F$) dissipation for two sets of elasto-plastic beams deforming in mode III: (a) of the same cross-section, $H = B = 0.01$ m ($\beta_w = 108.4$) and (b) the same aspect ratio, $L/H = 16$.

4.5.3 Mode III

Figure 4.11 plots the non-dimensional maximum impulse and energy for beams deforming in mode III ($p_s = 150$ MPa). Note that the ratio of the plastic work absorbed through shearing deformation to the total plastic work done has reached the critical ratio of $\beta_c = 0.45$ in all cases. The results in Fig 4.11 are broadly similar to Figs 4.9a and 4.10a, despite a slight decrease in $\bar{I}^T$ and $\bar{E}^T$ due to the fact that the time it takes for complete detachment to occur is less in mode III than in mode II - compare Figs 4.10a and 4.11b for an example. Notwithstanding, the effects of L/H and β_w on maximum impulse and energy transfer in mode III are broadly the same as that in Figs 4.9a and 4.10a for mode II. It is evident from both figures that far greater impulse and energy were transmitted to the elasto-plastic beams than the free-standing counterparts; this is also the case for modes I and II shown in Figs 4.7a, 4.8a, 4.9a and 4.10a.

4.6 Conclusions

The dynamic response of elasto-plastic beam subjected to underwater blast is studied. The analytical model from Chapter 2 is used to predict beam deformation, interface pressure history, impulse and energy transfer in a *Type I* cavitation event where they were found to be in excellent agreement with 3D FE simulations. It was found that increasing non-dimensional impulse I^* leads to the following: (1) a decrease in the maximum mid-span deflection for modes II and III; (2) a sharp reduction in the maximum transmitted impulse following a transition from mode I→II; and (3) monotonic reduction in both the maximum transmitted impulse and energy in modes II and III.

The effects of aspect ratio L/H and FSI index β_w were investigated for elasto-plastic beams deforming in different modes. Key findings can be summarised as follows: (1) In mode I, an increase in aspect ratio L/H or decrease in FSI index β_w always leads to a reduction in the maximum impulse transmitted; and (2) In modes II and III, increasing FSI index β_w always leads to less maximum transmitted impulse.

The effects of boundary on FSI were also studied for the elasto-plastic where it was shown, as to be expected, that a significantly higher impulse and energy are transmitted to the fully clamped deformable beams, deforming in all three modes, as opposed to the free-standing counterparts.

Chapter 5

Fluid-structure interaction in air blasts

5.1 Introduction

Kambouchev et al. (2006, 2007) extended Taylor's linear theory of fluid-structure interaction (FSI) in water to intense planar air blasts. Formulae for the momentum transfer to a freestanding plate were developed and calibrated by accurate numerical simulations. They found that transmitted impulse can be substantially reduced due to FSI effect for light free-standing plates. This beneficial influence of FSI in potentially mitigating the effect of blast has recently been explored as a basis for the design of sandwich structures with increased blast resistance: see Dharmasena et al. (2010, 2011), Ebrahimi and Vaziri (2013), Feng et al. (2007), Main and Gazonas (2008), Vaziri and Hutchinson (2007), Vaziri et al. (2007), Wadley et al. (2010, 2013) and Zhu et al. (2010). However, the effect of boundary (support) condition is omitted in their analysis, and as a result, the FSI effect is only significant at large displacement which limits its practical use.

Several studies attempted to investigate the effects of FSI for a fully clamped structures. For example, Subramaniam et al. (2009) investigated the blast pressure wave interaction with an elastic structure using a numerical approach, which considers FSI within an Arbitrary Lagrange Euler (ALE) framework. They found that the general assumption of rigid reflection (ignoring FSI effect) leads to a significant overestimation of displacements. And the error in the maximum displacement predicted by ignoring FSI effect is directly proportional to the ratio of the structure velocity to the speed of shock wave. However, the findings by Subramaniam et al. (2009) apply only to elastic structures.

In this chapter, the FSI between intense air blasts and an elasto-plastic monolithic beam system (developed in Chapter 2), will be investigated. The objective is to elucidate how large deformation, the fixing conditions at the supports and structural failure affect previously-known results; in particular, their implications on the energy and momentum transfer from the blast wave.

5.2 Formulation of the numerical approach

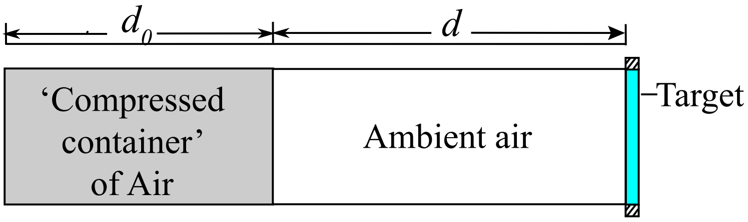

Figure 5.1: Schematic of FSI model in air.

Consider an 'air-column' of two parts, viz. 'compressed container' of adiabatic air and quiescent ambient air, and an elasto-plastic beam located at its right end (see Fig 5.1). The problem of interest concerns the dynamic response of the elasto-plastic beam subjected to the shock wave traveling in this compressible medium. At time $t = 0$ the 'compressed container' of air in the interval $0 \leq Z \leq d_0$ is prescribed with an initial velocity distribution of

$$v(Z) = v_0 e^{-(Z/d_0)^2} \tag{5.1}$$

where Z is the Lagrangian coordinate with $Z = 0$ denotes fluid-structure interface, d_0 is the length of the compressed air container and v_0 is the peak velocity. It follows immediately that the compressed air has a density distribution $\rho(Z)$

and a finite initial energy per unit area ΔE_0 given by Hutchinson (2009)

$$\begin{gathered}\frac{p(Z)}{p_a}=\left[\frac{\rho(Z)}{\rho_a}\right]^{\gamma_a}=\left[1+\frac{\gamma_a-1}{2}(\frac{v(Z)}{c_a})^2\right]^{\gamma_a/(\gamma_a-1)} \quad \text{and} \\ \Delta E_0=\frac{p_a d_0}{\gamma_a-1}\Big[\Big(1+\frac{\gamma_a-1}{2}(\frac{v_0}{c_a})^2\Big)^{\gamma_a/(\gamma_a-1)}-\Big(1+\frac{\gamma_a-1}{2}(\frac{v_0}{c_a})^2\Big)^{1/(\gamma_a-1)}\Big]\end{gathered} \tag{5.2}$$

where $\gamma_a(=1.4)$ is the ratio of specific heats, $p_a(=104761$ Pa) is the pressure, $\rho_a(=1.225$ kg/m^3) is the air density, $c_a(=346$ m/s) is speed of sound in air and the subscript 'a' denotes ambient conditions.

The equations governing the fluid motion (both compressed container of air and ambient air) are expressed in the Lagrangian framework and consist of the following:

1. The kinematic relation for the material velocity v and acceleration a are

   $$v=\frac{\partial x_e}{\partial t} \quad \text{and} \quad a=\frac{\partial v}{\partial t} \tag{5.3}$$

   where Eulerian coordinate x_e, velocity v and acceleration a of a fluid particle are functions of Lagrangian coordinate Z and time t.

2. The momentum conservation equation is given by

   $$\rho_0 a=-\frac{\partial p}{\partial Z} \tag{5.4}$$

   where ρ_0 is the initial density of the particle with Lagrangian coordinate Z.

3. Adding a viscous dissipation term Θ, the equation of state is modified as (Neumann and Richtmyer, 1950)

   $$p=(\gamma_a-1)\rho_0\frac{e}{F}-\Theta \tag{5.5}$$

   where e is the internal energy, $F=\partial x_e/\partial Z$ is the deformation gradient and the viscous term Θ is required to stabilise the numerical scheme

$$\Theta = \begin{cases} -\rho_a(K_1\dot{d}\Delta)^2 - \rho_a c_a K_2|\dot{d}|\Delta, & \dot{d} < 0 \\ 0, & \dot{d} \geq 0 \end{cases} \tag{5.6}$$

where $\dot{d} = (1/F)\partial F/\partial t$ is the rate of deformation, K_1 and K_2 are artificial viscosity coefficients and Δ is width of the shock wave which is of the order of grid spacing for numerical stability.

4. The energy conservation equation is given by

$$\frac{\partial e}{\partial t} = \left[(1-\gamma_a)e + \frac{\Theta}{\rho_c}\right] \tag{5.7}$$

where ρ_c is the current density of the air particle.

The staggered method is used to account for the fluid-structure coupling in time domain (Blom, 1998; Blom and Leyland, 1997). The interaction between the shock wave and the elasto-plastic beam is accounted for by enforcing the congruence conditions of velocity and displacement at the fluid-structure interface, i.e. the interface velocity and displacement are equal for both the fluid and the structure. Following Subramaniam et al. (2009) and Teich and Gebbeken (2013), it is assumed here that displacement at the mid-span of the beam represents that of the structural beam system in the one-dimensional air domain. Starting at a current time step, when the state of the fluid and structure are known, the fluid-structure system is integrated in time to obtain the solutions at the next time step as:

1. The current displacement at the fluid-structure interface is implemented in the fluid solver (Eqs. 5.3, 5.4, 5.5 and 5.7) to calculate interface overpressure p_{Int} for the next time step.

2. The mid-span displacement of the beam at the next time step is updated by solving the equation of motion of the beam under interface overpressure

$p_{\mathrm{Int}}(t) = p(Z = d + d_0, t) - p_a$ obtained from step 1, given as

$$\sum_{j=1}^{n} M_{ij}\ddot{w}_j + \frac{\partial V}{\partial w_i} = B p_{\mathrm{Int}}(t) \int_0^L \phi_i(x)\mathrm{d}x, \quad i = 1, 2, ..., n. \tag{5.8}$$

Governing equations (Eqs. 5.3, 5.4, 5.5 and 5.7) with initial condition (Eqs. 5.1 and 5.2) and artificial viscosity (Eq. 5.6) are solved using the widely used von Neumann-Richtmyer algorithm which is based on a finite difference discretisation of the governing equations (Neumann and Richtmyer, 1950). The details of the finite difference method are summarised in Appendix A.

5.3 Verification of the numerical method

The case of the normal reflection of uniform shocks on a fixed boundary provides a good basis for verification of the proposed numerical method. One of the basic implications of gas compressibility is the non-linear dependence of the pressure reflected from a fixed rigid wall on the magnitude of the incident shock pressure. The peak reflected overpressure can be expressed in the form of (Anderson, 2001)

$$p_r = C_R p_s \tag{5.9}$$

where the reflected coefficient C_R is given by the well-known Rankine-Hugoniot relationship

$$C_R = \frac{8p_s + 14p_a}{p_s + 7p_a} \tag{5.10}$$

which for small p_s/p_a, $C_R \simeq 2$; while, for $p_s/p_a \gg 1$, $C_R \to 8$.

The incident $p_I(t)$ and reflected $p_R(t)$ overpressure-time history following wave interaction with a reflective, clamped, rigid wall at different standoff are compared in Figs 5.2a and 5.2b for two different blast intensities. It can be seen that the non-linear compressibility of air causes the peak of the evolving pulse to decrease, with a corresponding increase in pulse duration, with distance travelled. Figure 5.3 compares the numerical normalised peak reflected overpressure p_r/p_s (extracted from Figs 5.2a and 5.2b at different standoff distance d/d_0) with the values of the

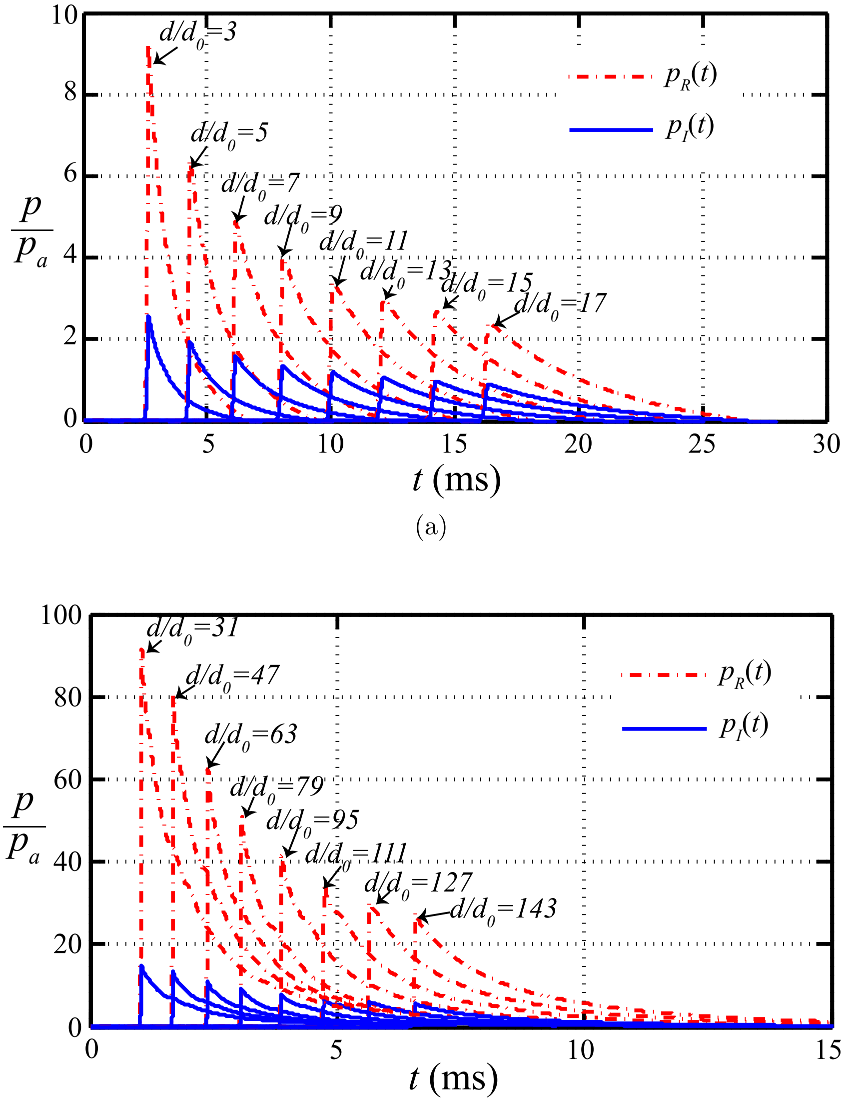

(a)

(b)

Figure 5.2: Incident $p_I(t)$ and reflected $p_R(t)$ overpressure-time histories upon interaction with a reflective, clamped, rigid wall at different standoff: (a) 'weak' shock wave with $v_0/c_a = 1.7$, $d_0 = 0.5$ m ; (b) 'strong' shock wave with $v_0/c_a = 5.1$, $d_0 = 0.05$ m.

reflected coefficients C_R given by Eq. 5.10. As it can be observed in the plot, the numerical results are in excellent agreement with the Rankine-Hugoniot theory for a wide range of shock intensities.

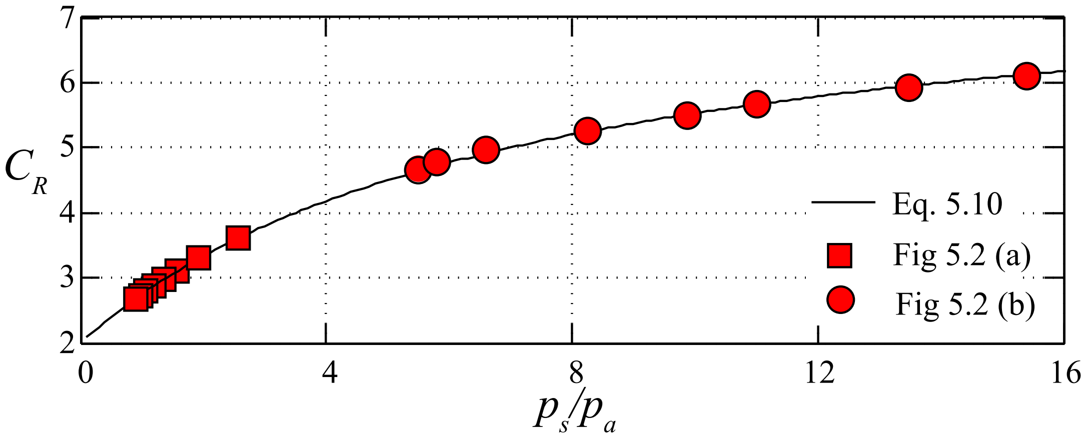

Figure 5.3: Reflected coefficient C_R for normal reflection of uniform shocks on a fixed boundary for both 'weak' and 'strong' shock wave in Fig 5.2.

5.4 Dynamic response with FSI

This section studies the dynamic response of elasto-plastic beams subjected to air shock waves in different modes of deformation. The definition of the time history of transmitted impulse per unit area $I^T(t)$ and transmitted energy per unit area $E^T(t)$ of the beam are given previously in Eq. 4.9. They are normalised by the incident impulse I_i and energy E_i respectively, given by (Kambouchev et al., 2007)

$$I_i = \int_0^{t_d} p_s \varphi(t) dt = p_s t_i \quad \text{and} \tag{5.11}$$

$$E_i = p_s^2 t_i / \rho_a c_a \tag{5.12}$$

where t_i is the decay constant of the incident wave and t_d is the pulse duration. Note that time t is defined at the time when the pressure wave is arrived at the interface $Z = 0$.

Figure 5.4 shows the dynamic response of an elasto-plastic beam of 0.17 m (L) $\times$ 0.01 m (H) $\times$ 0.01 m (B) subjected to an intense shock wave in air. The shock wave is created with the following parameters so that the beam develop mode I deformation: $d_0 = 0.05$ m, $d/d_0 = 79$ and v_0/c_a=5.1. The dynamic response of the beam without considering FSI effect was also included for comparison, which is obtained by prescribing the reflected overpressure history - from a fixed rigid

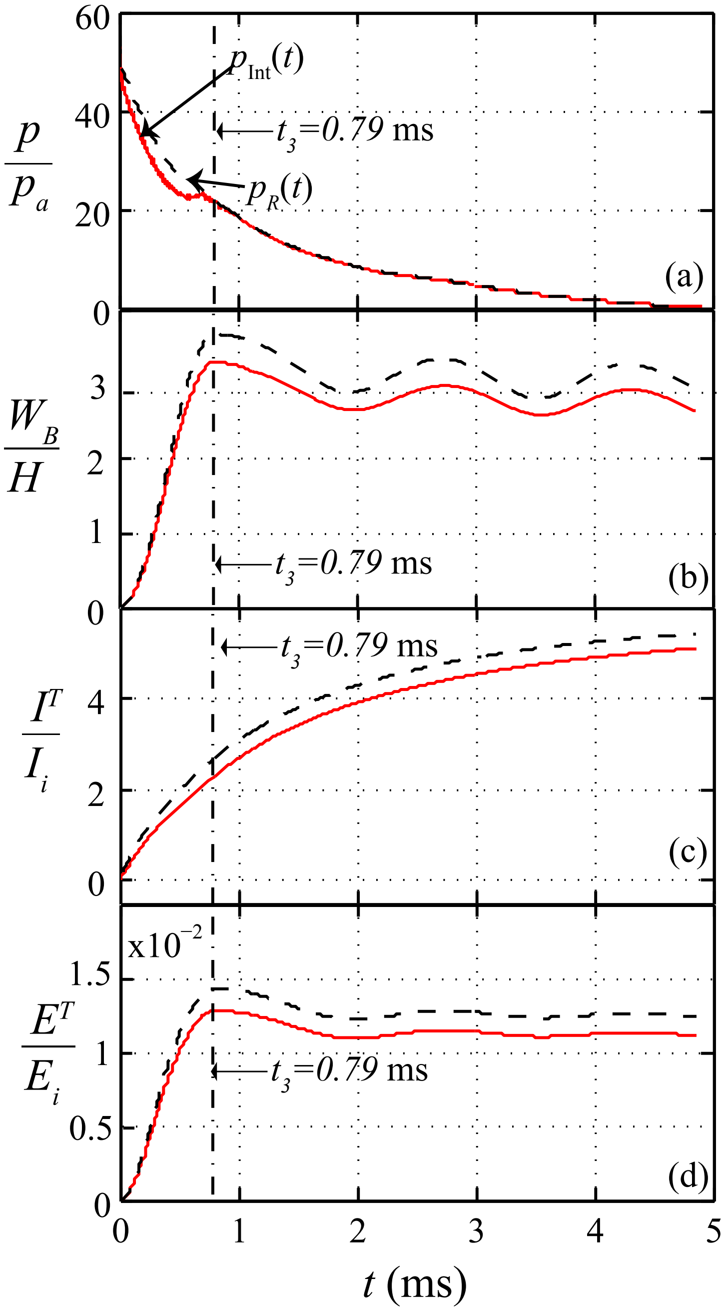

Figure 5.4: Dynamic response of elasto-plastic beams of 0.17 m (L) × 0.01 m (H) × 0.01 m (B) subjected to air shock wave (with d_0 = 0.05 m, d/d_0 = 63 and $v_0/c_a = 5.1$) during mode I deformation. - - denotes without FSI; — denotes with FSI.

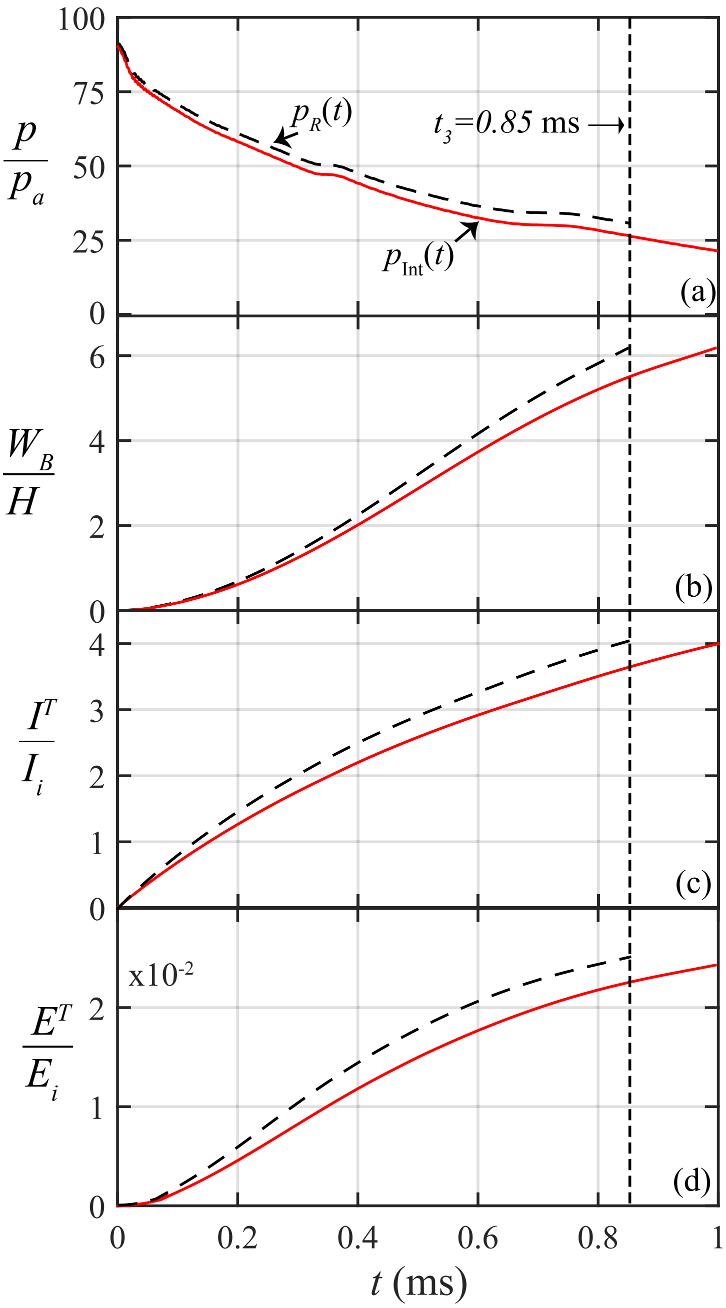

Figure 5.5: Dynamic response of elasto-plastic beams of 0.2 m (L) × 0.01 m (H) × 0.01 m (B) subjected to air shock wave (with d_0 = 0.05 m, d/d_0 = 31 and v_0/c_a = 5.1) during mode II deformation. - - denotes without FSI; — denotes with FSI.

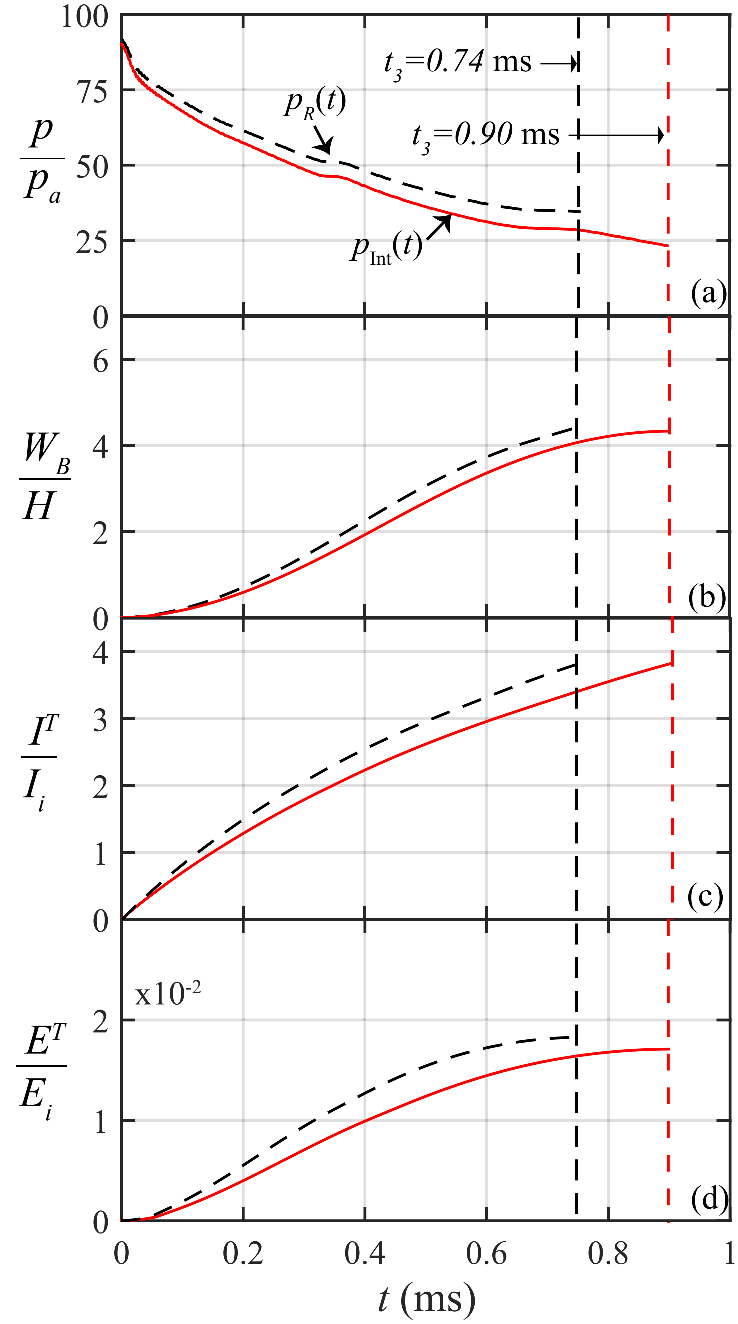

Figure 5.6: Dynamic response of elasto-plastic beams of 0.16 m (L) × 0.01 m (H) × 0.01 m (B) subjected to air shock wave (with $d_0 = 0.05$ m, $d/d_0 = 31$ and $v_0/c_a = 5.1$) during mode III deformation. - - denotes without FSI; — denotes with FSI.

surface - to the beam. Figure 5.4a shows that the interface overpressure $p_{\text{Int}}(t)$ is smaller compared to the reflected overpressure history $p_R(t)$ during $t \leq t_3$ (i.e. before the beam reaches maximum mid-span deflection); however beyond $t > t_3$, there is no significant differences between the two pressure history (with and without considering FSI). The deficiency during $t \leq t_3$ is due to the alleviation of interface overpressure by the rapid motion of the elasto-plastic beam. As a result of this FSI effect, the prediction of maximum mid-span deflection, maximum transmitted impulse and maximum transmitted energy are less compared to those without considering FSI, as seen in Figs 5.4b, 5.4c and 5.4d.

Figures 5.5 and 5.6 show the dynamic response of elasto-plastic beam during mode II and III deformation respectively. In both figures, the interface overpressure $p_{\text{Int}}(t)$ is lower compared to the reflected overpressure history $p_R(t)$. Again, the deficiency is a result of the relieving of interface overpressure by the beam motion prior to failure. This leads to a over-prediction of the temporal mid-span deflection $W_B(t)/H$, transmitted impulse $I^T(t)/I_i$ and energy $E^T(t)/E_i$ compared to those with FSI effect; these observations are in line with Fig 5.4. However, it is surprising to note that the peak value of the aforementioned predictions when considering FSI effect are similar to those without FSI effect. This is because when considering FSI effect, the time for complete detachment to occur is higher, which results in a longer loading duration compared to that ignoring FSI effect.

5.5 Importance of FSI

From the results in the previous section a relevant question which needs to be addressed is: for an incident blast pressure wave, when does FSI effect become important and to what extent ? Results in the last section show that FSI effect is evident to reduce maximum mid-span deflection, maximum transmitted impulse and maximum transmitted energy during mode I deformation, but not significant during mode II and III deformation. Therefore, the numerical model is now used to study the aforementioned problem only in mode I deformation. The difference between predictions with and without FSI effect, e.g. maximum mid-span deflection, is often viewed as an indicator of the error in predicted structural

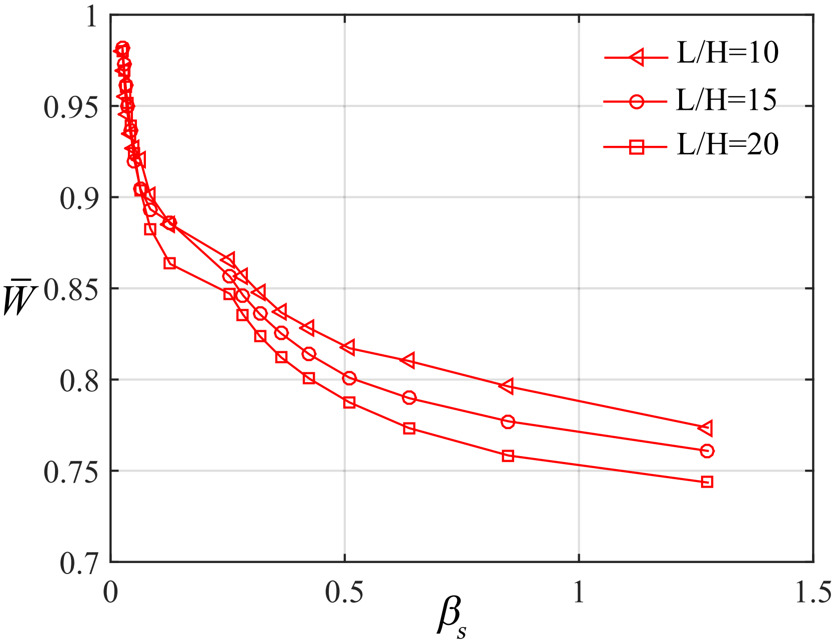

Figure 5.7: Variation of displacement ratio $\bar{W}$ and FSI index β_s in mode I.

response on ignoring FSI (Subramaniam et al., 2009). Here, it is defined the displacement ratio as $\bar{W} = W_0^{\text{FSI}}/W_0^{\text{NO FSI}}$ to measure the error (i.e. $1 - \bar{W}$) of ignoring FSI. The reflected overpressure history $p_R(t)$, obtained from a separate simulation, is prescribed to the elasto-plastic beams to obtain $W_0^{\text{NO FSI}}$.

Figures 5.8, 5.9 and 5.7 show the variation of displacement ratio $\bar{W}$ as a function of velocity ratio $v_{\max}/U_s$, time ratio t_3/t_d and FSI index by Kambouchev et al. (2006), $\beta_s = \rho_s U_s t_i/\rho H$ (given previously in Eq. 1.29), respectively. The shock wave is generated by the following parameters so that all the beams develop mode I deformation: $v_0/c_a = 5.6$, $d_0 = 0.05$ m and $d/d_0 = 79$. Note that the extreme cases of $v_{\max}/U_s = 0$ and $\beta_s = 0$ refer to the FSI with an elasto-plastic beam of infinite weight where the error of ignoring FSI is zero (Subramaniam et al., 2009), while the extreme case of $t_3/t_d = \infty$ refers to impulsive loading where FSI effect is negligible.

Figure 5.8 shows that with increasing velocity ratio $v_{\max}/U_s$, displacement ratio $\bar{W}$ reduces. The implication is that the margin by which the displacement obtained by ignoring the FSI effect would over predict the actual displacement

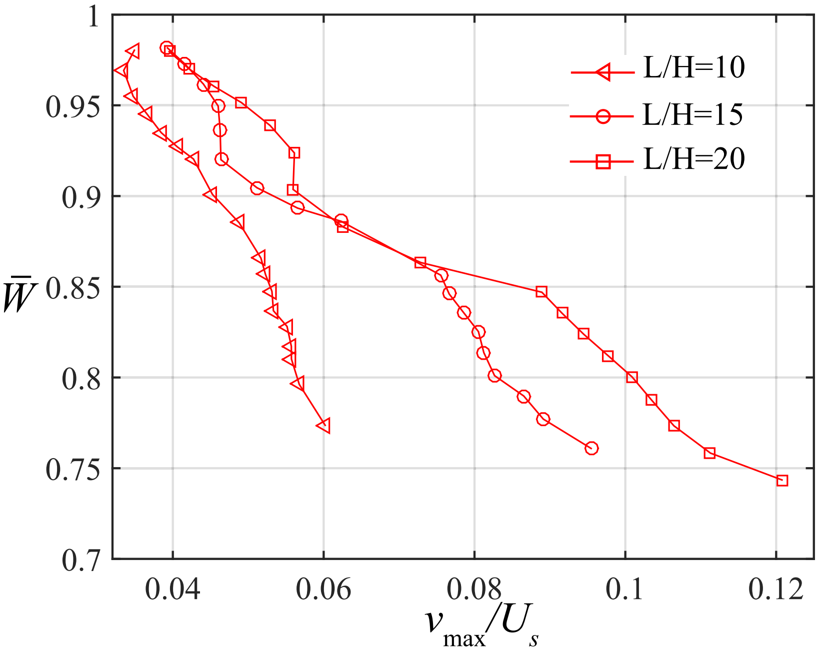

Figure 5.8: Variation of displacement ratio $\bar{W}$ and velocity ratio $v_{\max}/U_s$ in mode I.

increases as the maximum mid-span velocity increases relative to the velocity of the shock front. Figure 5.9 shows that as the time when the maximum mid-span deflection is reached increases relative to the duration of the incident wave (or becomes more 'non-impulsive'), the error in predicting structural response increases when FSI is not considered. Figure 5.7 shows that the error of ignoring FSI (or $1-\bar{W}$) increases with increasing FSI index β_s - this is consistent with the findings based on rigid, free-standing structures where FSI effect on mitigating the effect of the blast can be achieved by reducing the mass per unit area of the structure (Kambouchev et al., 2006, 2007).

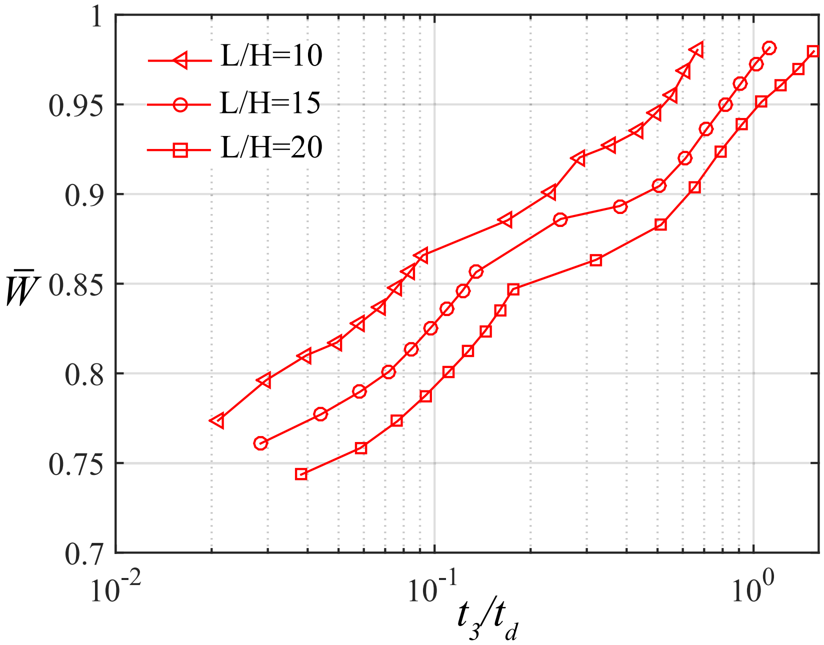

Figure 5.9: Variation of displacement ratio $\bar{W}$ and time ratio t_3/t_d in mode I.

5.6 Effects of FSI on 'elasto-plastic' and 'rigid free-standing' beams

In this section, the numerical model is employed to investigate the effects of FSI on the elasto-plastic beam system at different modes of deformation. Parametric studies were performed to evaluate the sensitivity of the maximum impulse ($\bar{I}^T$) and energy ($\bar{E}^T$) transfer to aspect ratio L/H and β_s ($\triangleq \rho_s U_s t_i/\rho H$ - Kambouchev's FSI index). $\bar{I}^T$ and $\bar{E}^T$ are given in Eq. 4.12. Results from rigid free-standing beams of an equivalent mass per unit area are also included for comparison where the maximum transmitted impulse and energy - superscript F denotes free-standing - are, respectively, given by (Kambouchev et al, 2007)

$$\bar{I}^F = \lambda_R^{\beta_s(1+\beta_s)} \beta_s^{\beta_s/(1-\beta_s)} \tag{5.13}$$

and

$$\bar{E}^F = \lambda_R^{2\beta_s(1+\beta_s)} \frac{(1-e^{-\beta_s})^2}{2\beta_s}. \tag{5.14}$$

where non-dimensional parameter λ_R is given by Eq. 1.33.

5.6.1 Mode I

The solid red lines in Figs 5.10a and 5.10b denote the non-dimensional maximum transmitted impulse ($\bar{I}^T$ and $\bar{I}^F$) and the broken black lines denote the non-dimensional maximum transmitted energy ($\bar{E}^T$ and $\bar{E}^F$). The following initial conditions are used throughout so that all the elasto-plastic beams develop mode I deformation: $d_0 = 0.05$ m, $d/d_0 = 79$ and v_0/c_a=5.1. Figures 5.10a and 5.10b present the variation of the maximum non-dimensional impulse and energy terms, as a function of L/H (for a constant $\beta_s = 0.084$) and as a function of β_s (for a constant $L/H = 17$), respectively. It can be seen that $\bar{I}^T$ reduces monotonically with increasing L/H or β_s. The reason is that increasing L/H or β_s leads to higher motion of the elasto-plastic beam, resulting in greater alleviation of interface overpressure. In both Figs 5.10a and 5.10b, more impulse are transmitted to the elasto-plastic beams, i.e. $\bar{I}^T > \bar{I}^F$; because the alleviation of interface overpressure is greater for free-standing beams due to higher velocity. However, free-standing beams have significantly higher maximum transmitted energy, i.e. $\bar{E}^F > \bar{E}^T$; because the free-standing beams have significantly higher displacements.

5.6.2 Mode II and III

Variations of maximum non-dimensional impulse and energy terms against L/H and β_s for beams (with $d_0 = 0.05$ m, $d/d_0 = 31$ and v_0/c_a=5.1) are shown in Figs 5.11a and 5.11b respectively, where the elasto-plastic beams develop mode II, and even mode III deformation. Note that in mode III the ratio of the plastic work absorbed through shearing deformation to the total plastic work done reaches the critical ratio of $\beta_c = 0.45$. It is evident that mode III tends to occur for elasto-plastic beams with low L/H and high β_s. This is because decreasing L/H or increasing β_s leads to a smaller mid-span deflection, which, in turn, results in a smaller proportion of plastic work absorbed through membrane deformation to the total plastic work done. Therefore the plastic work absorbed through shearing

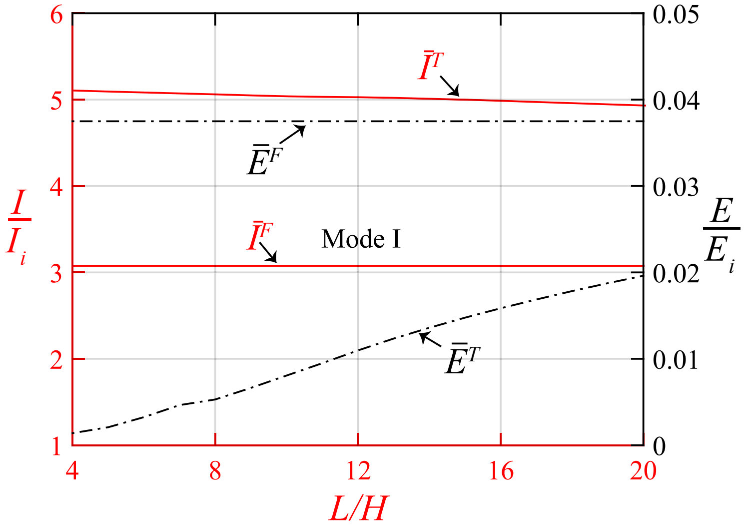

(a)

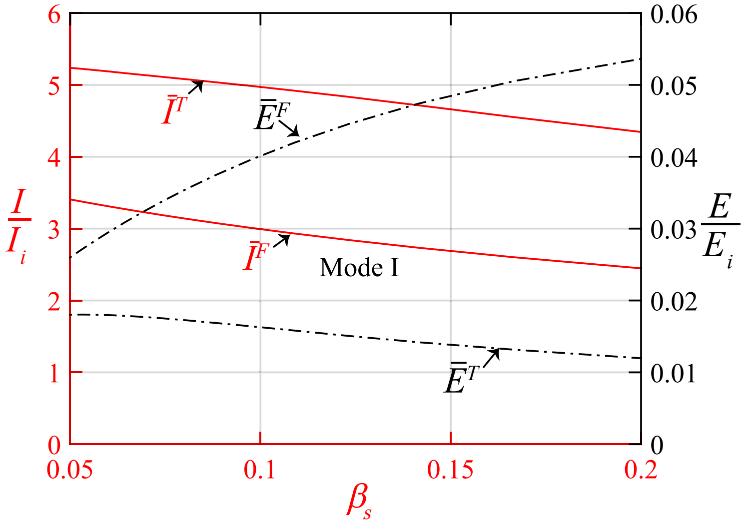

(b)

Figure 5.10: Numerical prediction of non-dimensional maximum impulse (— corresponds to $\bar{I}^T$ and $\bar{I}^F$) and energy (–.– corresponds to $\bar{E}^T$ and $\bar{E}^F$) dissipation for two sets of beams: (a) same beam cross-section, $H = B = 0.05$ m ($\beta_s = 0.084$) and (b) same aspect ratio, $L/H = 17$.

deformation to the total plastic work done β is more significant, since plastic work absorbed through bending is negligible in mode III (see Fig 3.9).

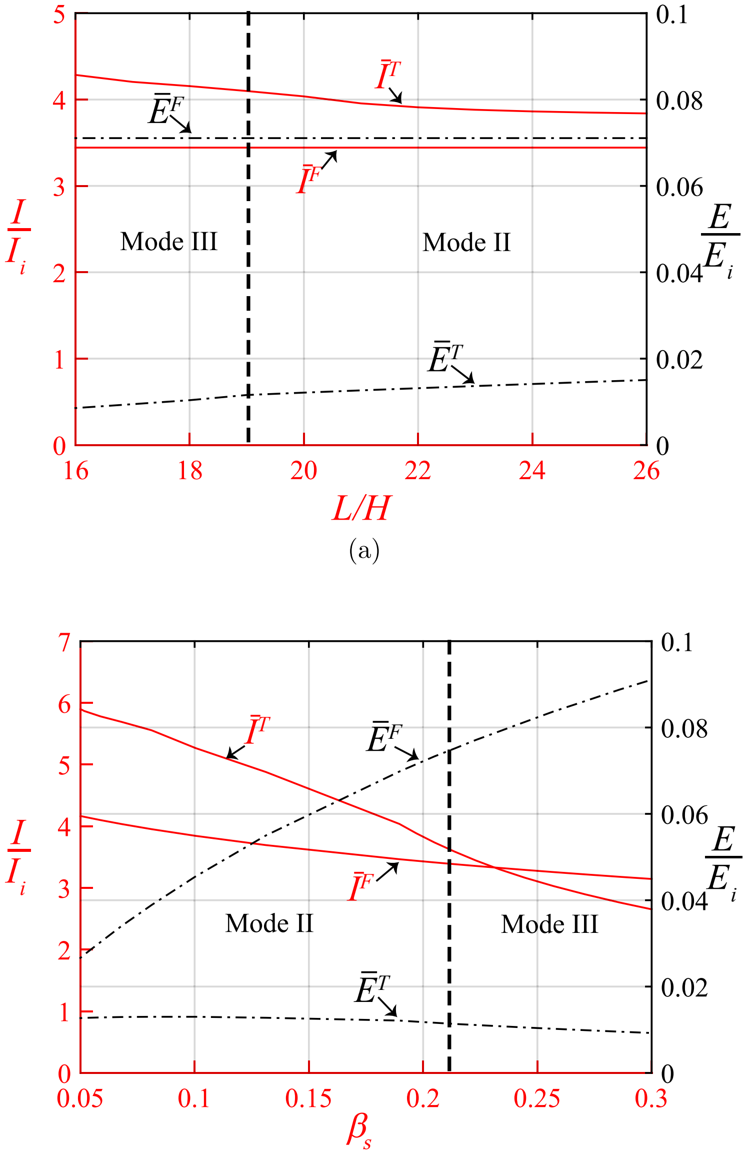

(a)

(b)

Figure 5.11: Numerical prediction of non-dimensional maximum impulse (— corresponds to $\bar{I}^T$ and $\bar{I}^F$) and energy (–.– corresponds to $\bar{E}^T$ and $\bar{E}^F$) dissipation for two sets of beams: (a) same beam cross-section, $H = B = 0.01$ m ($\beta_s = 0.189$) and (b) same aspect ratio, $L/H = 20$.

It can be seen in Figs 5.11a and 5.11b that $\bar{I}^T$ drops with increasing L/H or β_s, because the time for complete detachment to occur is shorter for beams with higher L/H or β_s. In both Figs 5.11a and 5.11b, all the elasto-plastic beams in mode II and III have greater maximum transmitted impulse and less maximum transmitted energy compared to free-standing beams, i.e. $\bar{I}^T > \bar{I}^F$ and $\bar{E}^T < \bar{E}^F$, apart from a range of β_s in mode III where $\bar{I}^T < \bar{I}^F$ - this is because complete detachment for elasto-plastic beams occur even earlier than interface overpressure for free-standing beams drop to zero.

5.7 Comparison between structural performance in underwater explosion and in air blast

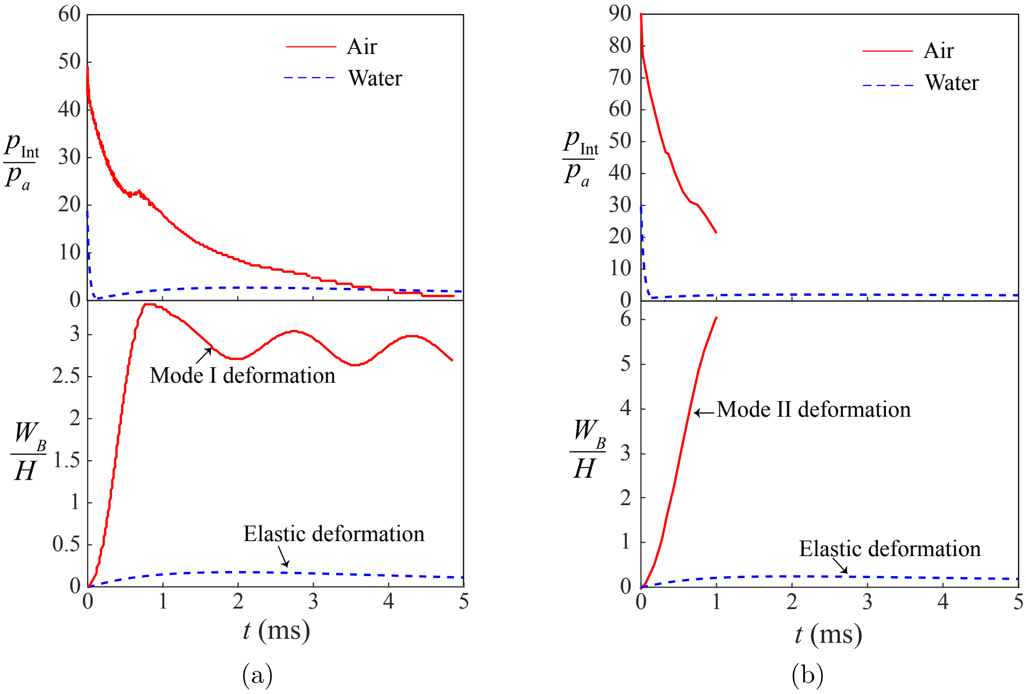

(a) (b)

Figure 5.12: Predictions of temporal interface pressure and mid-span deflection of elasto-plastic beam subjected to a shock wave in air and water. The results for air blast were shown previously in Figs 5.4 and 5.5.

Which medium, air or water, is more effective in mitigating the effects of blast loading for elasto-plastic structure is an important issue. A comparison of structural performance under a blast wave of same intensity (i.e. same peak incident overpressure p_s and decay constant t_i) in underwater explosion and air blast is made to elucidate the aforementioned. Figure 5.12 compares the predictions of interface pressure and mid-span deflection of an elasto-plastic beam subjected to an incident shock wave in both air and water. The incident overpressure in Figs 5.12a and 5.12b can be characterised by $p_s = 1.00$ MPa and $t_i = 1.14$ ms, and $p_s = 1.55$ MPa and $t_i = 0.74$ ms respectively. It can be seen in both figures that: (1) the peak interface overpressure in air is significantly higher than that in water which is due to the non-linear compressibility effect of air; and (2) the interface pressure $p_{\mathrm{Int}}(t)/p_a$ in water drops more dramatically than that in air, as a result of greater alleviation of interface pressure due to the significantly higher bulk modulus of water. Both contribute to the significantly less mid-span deflection in water compared that in air, i.e the elasto-plastic beam can develop mode I and even mode II deformation in air, but only elastic deformation in water. This demonstrates the superiority of water over air to mitigate the effect of blast wave on elasto-plastic structures when subjected to the same incident wave.

However, it is notable that the effect of standoff distance is omitted from the analysis above purposely, in an attempt to highlight the difference of two mediums on the effect of mitigation of blast effect due to FSI. Clearly, increasing standoff distance leads to attenuation of peak overpressure and longer pulse duration (see Figs 5.2a and 5.2b for examples) in compressible medium (air), whereas the shock wave travels without losing either peak overpressure, pulse duration, or pulse shape in incompressible medium (water) - this is exactly the case when detonating the same explosion in both mediums. In such case, the incident wave imparted on the structure will be different (unlike the analysis above) in the two mediums, i.e. the peak overpressure is significantly higher and pulse duration is less in underwater explosion than those in air blasts. As a result, the structure might be more vulnerable in underwater explosion - than in air blast - despite its superior capacity of mitigating blast effect (as seen in Figs 5.12a and 5.12b); this has also been noted by Xue and Hutchinson (2004) for sandwich structures.

5.8 Conclusion

The dynamic response of elasto-plastic beam subjected to intense air blast has been analysed. Numerical model has been developed to predict mid-span displacement, interface overpressure history, impulse and energy transfer during FSI at all modes of deformation. It was found that the over-prediction in the structural response when ignoring FSI increases as a result of the following: (1) a higher ratio of the maximum mid-span velocity $v_{\max}$ relative to the shock speed U_s - in line with Subramaniam et al. (2009); (2) a lower ratio of the time when the maximum mid-span deflection is reached t_3 relative to the pulse duration t_d; and (3) reducing mass per unit area of the beam.

The effects of aspect ratio L/H and FSI index β_s were investigated for elasto-plastic beams deforming in different modes. Key findings can be summarised as follows: (1) during mode I deformation, increasing L/H or β_s lead to maximum less transmitted impulse; and (2) during mode II and III deformation, an increase of L/H or β_s results in a reduction in maximum transmitted impulse.

The effects of boundary on FSI were also studied for the elasto-plastic. It was found that the elasto-plastic beams, in general, have significantly higher maximum transmitted impulse but lower maximum transmitted energy than the free-standing counterparts at any mode of deformation, apart from some cases where the elasto-plastic beams deform in mode III, the maximum transmitted impulse are less than those of the free-standing beams.

Which medium, compressible (air) or incompressible (water), is more effective in mitigating the effects of a blast wave for elasto-plastic structure is investigated. It was found that the structure - when subjected to the same incident wave in both mediums - is less likely to develop large inelastic deformation and complete detachment at the support for underwater blast loadings compared to air blasts. However, if the effects of standoff distance is taken into consideration, the above finding may reverse, since in air blast the incident shock wave attenuates as it propagates whilst it does not in underwater explosions.

Chapter 6

Blast response of rectangular plates

6.1 Introduction

The mode of deformation in a fully clamped monolithic beam under impulsive loading depends on the non-dimensional impulse I^* $(:=\hat{I}/H\sqrt{\sigma_Y \rho})$, where $\hat{I} = \int_0^{t_d} p(t)/B\mathrm{d}t$, and is classed as either mode I (large inelastic deformation) or mode II (tensile-tearing and deformation) or mode III (shear-band localisation) - see Menkes and Opat (1973). Olson et al. (1993), too, observed similar modes in fully clamped, square mild-steel plates. Further experiments by Nurick and Shave (1996) suggested that the mode II deformation may be sub-divided into three distinct régimes of mode II* (through-thickness tearing along the supports), mode IIa (complete detachment from supports with maximum central deflection *increasing* with impulse) or mode IIb (complete detachment from supports with maximum central deflection *decreasing* with impulse). Similar mode I and II (II*, IIa, IIb) deformations were also observed in rectangular plates where aspect ratio $\gamma = 1.2$ (Ramajeyathilagam and Vendhan, 2004).

Nearly all the available experimental data in the literature (Nurick and Shave, 1996; Olson et al., 1993; Rudrapatna et al., 1999), with the notable exception of those by Ramajeyathilagam and Vendhan (2004), were performed with square plates. However, it remains unclear how the aspect ratio γ $(:= a/b$ - see Fig 6.1a) of rectangular plates affect its mode of deformation if γ >1. In a similar vein, little is known of how the fixing conditions at the supports affect the tearing mechanism in the plate which, in turn, has an effect upon the plate performance. The aforementioned issues are addressed in this chapter which will present the results of a detailed numerical study to elucidate how combinations of blast impulse and aspect ratio affect the deformation mode and how limits to deformation, caused by necking localisation and/or ductile fracture at the supports, affect the overall performance of rectangular plates to impulsive loadings. The numerical results are validated against experimental data for square mild-steel and aluminium plates where they will be found to be in good agreement.

6.2 Finite element modelling

6.2.1 Mesh, loading and boundary conditions

Finite element analysis were performed using ABAQUS/Explicit (2012). All plates modelled have length $2a$, width $2b$ ($a > b$) and thickness H if their aspect ratio $\gamma > 1$. If $\gamma = 1$, the plates have equal length of $2a$ on all sides. Only a quarter of the solid plate is modelled since reflective symmetry exists on two planes, as seen in Fig 6.1. Eight 8-node brick elements (C3D8R) with reduced integration and hour-glass control were employed through the thickness of each plate. All brick elements have equal dimension of 0.0002 m on all sides; hence, a typical 0.089 m × 0.089 m × 0.0016 m plate tested by Menkes and Opat (1973) would comprise of 255792 (168 × 168 × 8) elements in its corresponding FE model. Results of convergence studies, to be presented later in Fig 6.2, confirm that this is sufficient to simulate ductile and shear damage with acceptable fidelity.

Xue and Hutchinson (2003, 2004) have shown that the impulsive blast response of a structure is sensitive to the response time T needed to attain maximum deflection for a zero-period impulse. This time scale determines whether it is acceptable to idealise a finite-period loading as a zero-period impulse, i.e. the plate acquires an instantaneous initial velocity of $V_0 = \hat{I}/m$, where $\hat{I}$ is the impulse per unit area and $m = \rho H$ is mass per unit area of the plate. The response time of the square plate in the experiments of Nurick and Shave (1996), with dimensions 0.089 m × 0.089 m × 0.0016 m and material properties given in Table 6.2, is found numerically to be 120 μs. Since the typical blast duration is $t_d = 15$ μs in Nurick and Shave (1996), the loading imparted by the blast pulse may be idealised as a zero-period, *uniform-momentum* impulse (since $t_d/T = 0.125 \ll 1$) so the plate acquires an instantaneous velocity. In a similar vein, since the response time of the rectangular plates are also of the same order of magnitude as the square plates in Nurick and Shave (1996), assuming that the blast duration remains at $t_d \approx 15$ μs, the zero-period idealisation would remain equally valid.

Figure 6.1a gives the standard fully clamped boundary condition (BC) used by existing numerical studies for plates (Nurick and Shave, 1996; Ramajeyathilagam and Vendan, 2004; Rudrapatna et al., 1999, 2000). To accurately model progressive ductile fracture along the boundary of the plate, a modified BC given in Fig 6.1b is used here - this is similar to that employed in Chapter 3 for beams. The efficacy of the modified BC is further demonstrated in Section 6.3 by the excellent agreement between the predicted maximum plate deflection by the FE model and the experimental results given by Nurick and Shave (1996) and Olson et al. (1993).

Table 6.1: Number of elements in each direction of the uniform-mesh for Part 1

Mesh	Number of elements in z-direction	Number of elements in x- and in y-directions
1	1	21
2	2	42
3	3	63
4	4	84
5	5	105
6	6	126
7	7	147
8	8	168
9	9	189
10	10	210

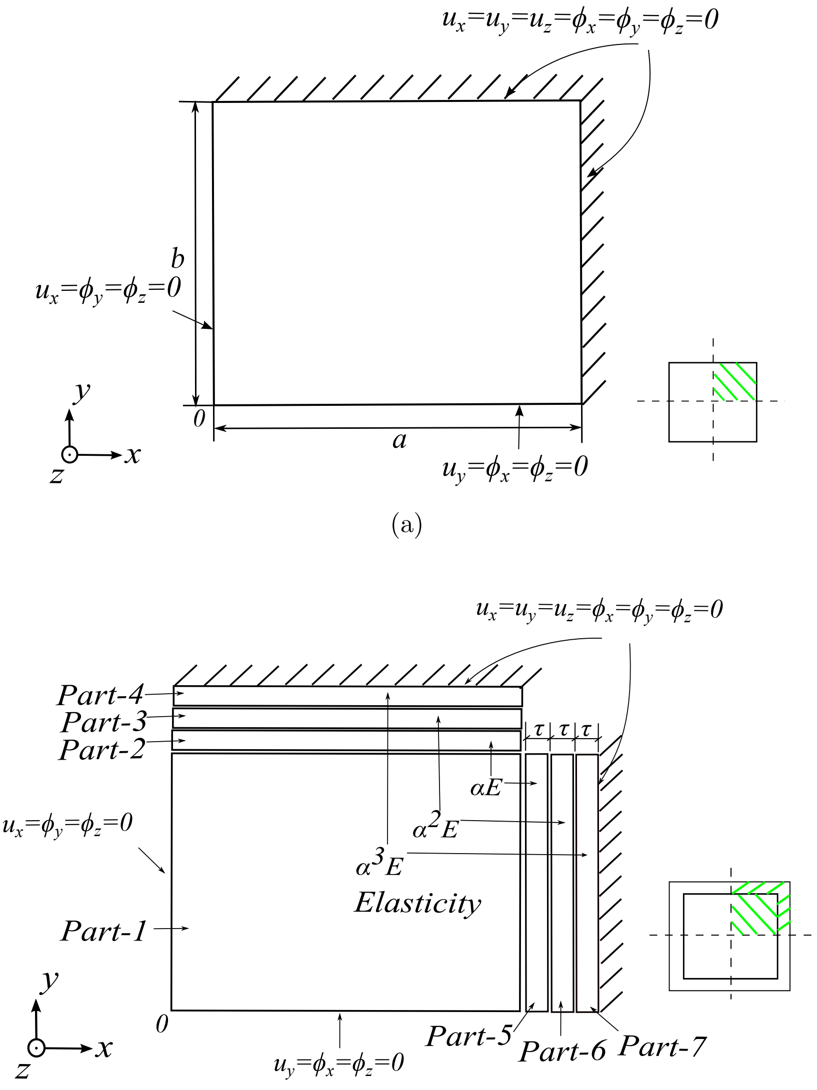

(a)

(b)

Figure 6.1: (a) fully clamped and (b) modified boundary conditions adopted in the FE model. u and ϕ refers to displacement and rotational degree of freedoms, respectively. $a > b$ for rectangular and $b = a$ for square plates.

Three additional parts (parts 2-4 and parts 5-7) are added to each side of the original solid plate (part-1) to form an extended boundary as shown in Fig 6.1b. Note that the standard fully clamped BC of Fig 6.1a are imposed on parts 4 and 7. All the additional parts have equal width τ and identical material properties as the solid plate, apart from a gradation of their elastic modulus E, by a factor α. Symmetric BCs are applied, just like to the solid plate. The parameters $\tau = H/6$ and $\alpha = 10$ are obtained by calibration to the experimental data at Nurick and Shave (1996).

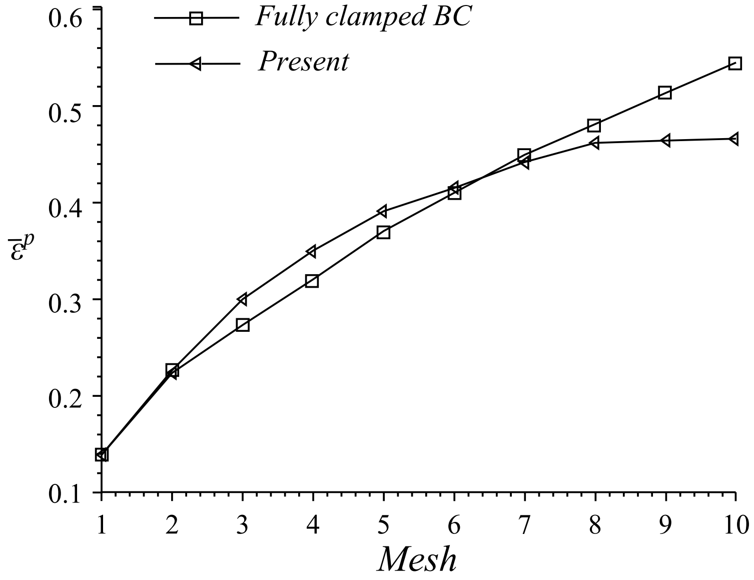

Figure 6.2: Predicted maximum equivalent plastic strain $\overline{\epsilon}^p$ at $(x = a, y = 0)$ and $(x = 0, y = b)$. Results are for square mild-steel plate of dimensions 0.089 m × 0.089 m × 0.0016 m subjected to a non-dimensional impulse of $I^* = 0.632$ (or $\hat{I} = 1378$ Ns/m^2). The mild steel properties of Nurick and Shave (1996) is used, see Table 6.2. 'Present' refers to predictions using the modified boundary condition in Fig 6.1b.

Figure 6.2 plots the predicted maximum equivalent plastic strain $\overline{\epsilon}^p$ for different mesh density used in part-1. The number of elements along each direction of the uniform-mesh is listed in Table 6.1. For a square plate with fully clamped boundary condition, the maximum values for $\overline{\epsilon}^p$ are found at $(x = a, y = 0)$ and $(x = 0, y = b)$ where tearing is expected to initiate from either, or both, locations. It is evident that $\overline{\epsilon}^p$ does not converge for the standard BCs shown in Fig 6.1a. Instead, convergence is achieved with the modified BCs. Figure 6.2 shows that mesh size No.8 gives sufficiently accurate results and is used here.

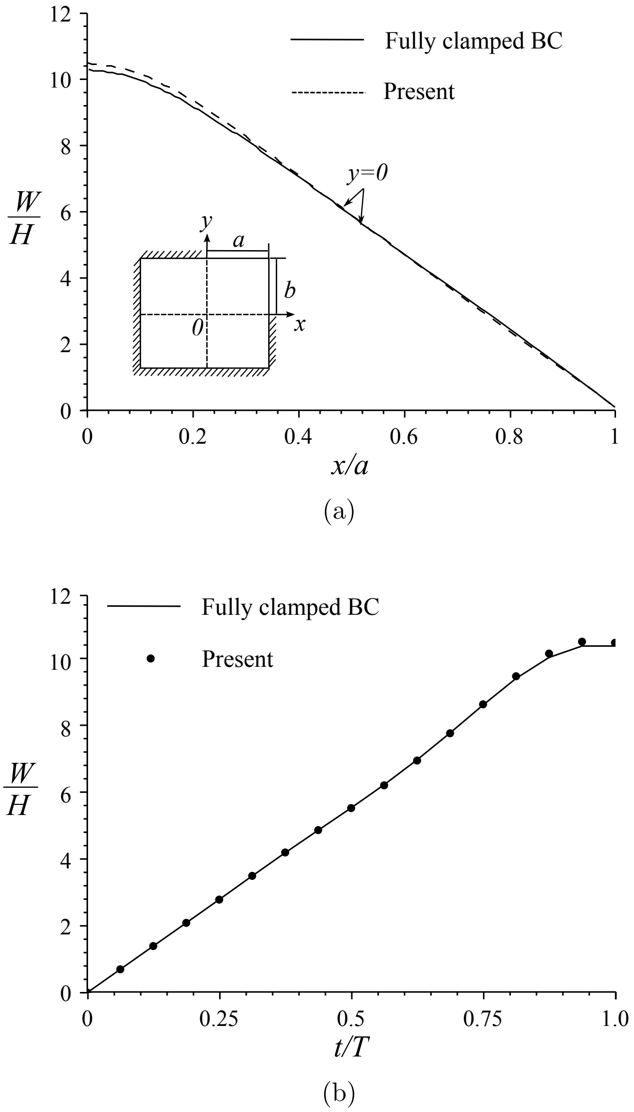

Figure 6.3: (a) Deflection profile along the x-axis (the same for y-axis due to symmetry) and (b) time-history of the central deflection of the plate. Results are for square mild-steel plate of dimensions 0.089 m × 0.089 m × 0.0016 m and subjected to a non-dimensional impulse of $I^* = 0.632$ (or $\hat{I} = 1378$ Ns/m^2). The mild steel properties of Nurick and Shave (1996) is used, see Table 6.2. ‘Present’ refers to predictions using the modified boundary condition in Fig 6.1b.

Figure 6.3a shows that the differences between the predicted deflection profiles by the two BCs are negligibly small. Similarly, for the time-history of their central deflections as shown in Fig 6.3b. In general, W_0/H are unaffected by the presence of stress singularities at the boundary; therefore, evaluation of performances, based on maximum transverse deflection of the plates, lead to identical conclusions for either BCs provided necking localisation and ductile fracture had not intervened.

6.2.2 Materials and damage models

Two plate materials are modelled in this study, aluminium (6061-T6) and mild-steel. Table 6.2 lists the properties of the respective plate material. Notice that the static yield strength of mild-steel in Olson et al. (1993) is slightly higher than that by Nurick and Shave (1996).

Table 6.2: Properties of plate material used in the FE model.

	ρ (kg/m^3)	E (GPa)	σ_Y (MPa)	σ_U (MPa)	ν	D_q (s^{-1})	q
Al 6061-T6[1]	2760	69	283	320	1/3	-	-
Mild steel[2]	7830	197	237	312	1/3	40.4	5
Mild steel[3]	7830	197	292	312	1/3	40.4	5

[1](Jones et al., 1970), [2](Nurick and Shave, 1996) and [3](Olson et al., 1993).

The material description adopted is based on the conventional J_2 plasticity constitutive relation with linear isotropic hardening. Material strain rate sensitivity is accounted for through a dynamic flow stress, evaluated at a uniaxial plastic strain rate $\dot{\epsilon}^p$, by adopting the Cowper-Symonds constitutive relation by Jones (1989)

$$\sigma_\mathrm{d} = \sigma_Y \Big(1 + |\frac{\dot{\epsilon}^p}{D_q}|^{1/q}\Big). \tag{6.1}$$

Both D_q and q are material parameters given in Table 6.2. The aluminium plates are assumed to be rate-insensitive.

Failure of solid plates subjected to impulsive loading can be attributed to two competing bulk material failure mechanisms, viz. ductile fracture and/or shear band localisation (Jones et al., 1970; Olson et al., 1993; Nurick and Shave, 1996). The progressive damage model for ductile materials in ABAQUS/Explicit (2012) is used here. The criteria for initiation of ductile (ω_d) and shear (ω_s) damage in the FE model are given by

$$\omega_d = \int \frac{d\bar{\epsilon}^p}{\bar{\epsilon}^p_d(\eta, \dot{\bar{\epsilon}}^p)} = 1 \quad \text{and} \quad \omega_s = \int \frac{d\bar{\epsilon}^p}{\bar{\epsilon}^p_s(\theta_s, \dot{\bar{\epsilon}}^p)} = 1 \tag{6.2}$$

where ω_d and ω_s are state variables that increases monotonically with the incremental change in equivalent plastic strain. Here, the equivalent plastic strains $\bar{\epsilon}^p_d$ (at the onset of ductile damage) and $\bar{\epsilon}^p_s$ (at the onset of shear damage) are assumed, respectively, to be a function of stress triaxiality η and strain rate $\dot{\bar{\epsilon}}^p$; and, a function of the shear stress ratio θ_s and strain rate $\dot{\bar{\epsilon}}^p$. When the criteria in Eq. 6.2 are met, the damage variable D would increase according to (ABAQUS/Explicit, 2012)

$$\dot{D} = \frac{\dot{\bar{u}}^p}{\bar{u}^p_f} \tag{6.3}$$

where $\bar{u}^p_f$ is the effective plastic displacement at failure; $\dot{\bar{u}}^p = L_e \dot{\bar{\epsilon}}^p$ and $L_e = 2 \times 10^{-4}$ m is the characteristic length of the first-order element used in the present FE model. Any element where their material stiffness is fully degraded, i.e. $D = 1$, is deleted from the mesh. Table 6.3 lists the parameters used in the damage models. Note that the parameters for both ductile and shear damage are obtained by calibration to the experimental data of Nurick and Shave (1996).

Table 6.3: Material parameters used by the damage model

Damage model	$\bar{\epsilon}^p_d$ or $\bar{\epsilon}^p_s$	$\bar{u}^p_f$
Ductile	0.2	0.00011
Shear	0.2	0.00008

6.3 Validation

In this section, the FE predictions are validated against experimental data for square mild-steel (Olson et al., 1993; Nurick and Shave, 1996) and rectangular aluminium plates (Jones, 1970). Note that the blast loadings may also be idealised as zero-period impulses. The aluminium plates used by Jones et al. (1970) have dimensions 0.1286 m× 0.0763 m × H m, with a range of thickness H. The square mild-steel plate specimens in the experiments by Olson et al. (1993) and Nurick and Shave (1996) have dimensions of 0.089 m × 0.089 m × 0.0016 m. The properties for the two different mild steel and one aluminium plate are listed in Table 6.2. Only the mode I central deflection are available in Jones et al. (1970) whilst data on all three modes of deformation are provided by Olson et al. (1993) and Nurick and Shave (1996).

6.3.1 Maximum transverse plate displacement - mode I

Figure 6.4a shows that the modified BC appears to better predict the central deflection of the thicker plate specimens ($H = 6.2$ mm). This is because relaxation of the in-plane and out-of-plane degrees of freedom at the plate boundary, gives a somewhat larger W_0/H than the standard BC would otherwise allow. Failure to account for material strain rate sensitivity would lead to over-prediction of W_0/H with I^* as shown in Fig 6.4b. In general, there is a good agreement between experiment data and the current FE predictions.

Figure 6.5 plots the deflection profile along $y = 0$ for a square mild steel plate subjected to a non-dimensional impulse $I^* = 0.86$. Its central deflection is well predicted by the current FE model. This lends further support to the contention that replacing the standard BC with the modified one in Fig 6.1b has hardly any effect upon the central deflection of the plate. Note, however, that discrepancies in the deflection profiles are observed away from $x = 0$. As $x \to a$, the modified BC give a better prediction of the deformed plate profile compared to the standard one, again, because the former relaxes the in-plane and out-of-plane degree of freedom along the boundary.

The predicted central deflection is compared to the experimental data in Nurick and Shave (1996) where there is a good agreement, see Fig 6.6. Furthermore, the FE model successfully predicts a reduction in W_0/H with increasing I^* for a plate deforming in mode IIb. The observed discrepancy between FE predictions and experimental data for mode IIb is because the former records the

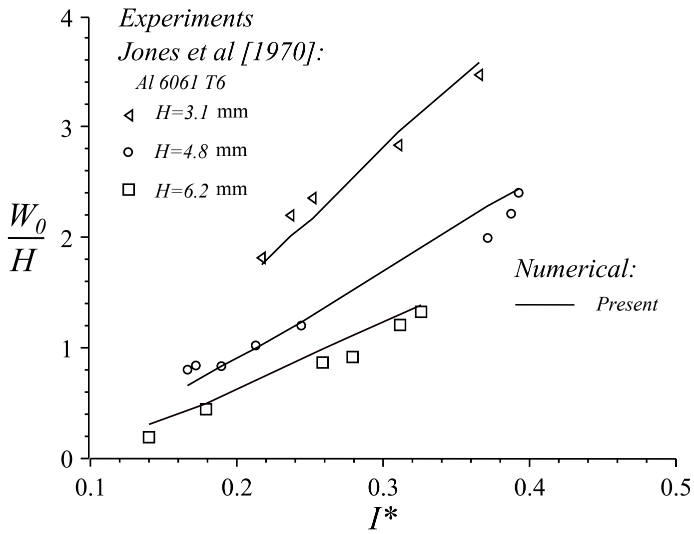

(a)

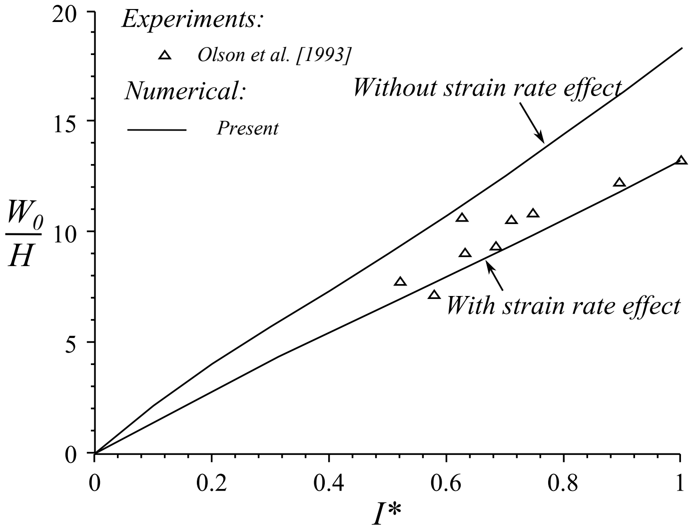

(b)

Figure 6.4: Comparison of the mode I central deflection for (a) aluminium plate by Jones et al. (1970) and (b) mild steel plate by Olson et al. (1993) with FE predictions at different levels of I^*. The aluminium and mild-steel plates has aspect ratios of $\gamma = 1.685$ and $\gamma = 1$, respectively.

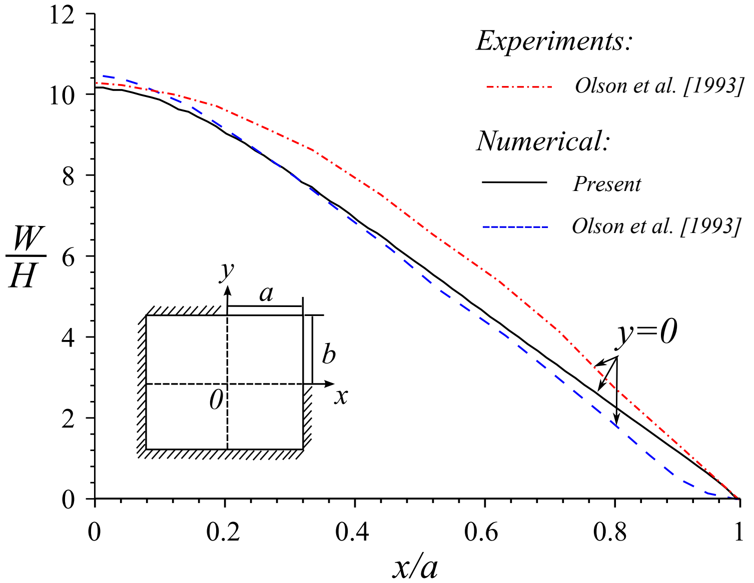

Figure 6.5: Deflection profile of a mild steel plate ($\gamma = 1$) subjected to an impulsive load of $\hat{I} = 1872$ Ns/m^2 (or $I^* = 0.86$). The mild steel properties of Olson et al. (1993) is used, see Table 6.2.

central deflection of the plate just before it completely detaches from the supports unlike in the latter.

Nurick and Shave (1996) reported that, for mode II*, the plate tears away from the supports resulting in ‘pulling-in’ of the mid-side of the plate. This ‘pulling-in’ distance increases initially with I^* but reduces when the maximum plate deflection is reached. The general trend of the 'pull-in' distance with I^* is well predicted by the current FE model in Fig 6.7. The observed discrepancies are due to the same reason given previously for Fig 6.6.

6.3.2 Critical impulses corresponding to mode transitions - mode I→IIa and IIb→III

A non-dimensional parameter Ψ is introduced to quantify the area fraction of plate that has become detached from the supports as follows

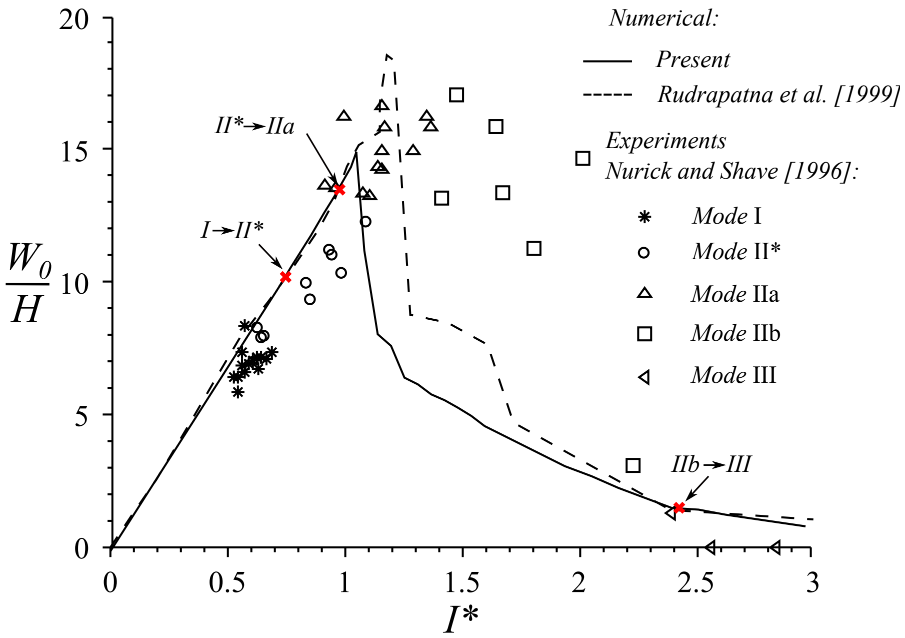

Figure 6.6: Comparison of the numerical central (maximum) deflection with the experimental data at different levels of I^*. Each red cross indicates a transition in deformation mode predicted by the current FE model. All mild steel plates have aspect ratio of $\gamma = 1$. The mild steel properties of Nurick and Shave (1996) is used, see Table 6.2.

$$\Psi = \frac{Area\ of\ detached\ plate\ periphery\ from\ supports}{Total\ area\ of\ plate\ periphery\ attached\ to\ supports\ [= 2Ha\ or\ 2Hb)]}. \tag{6.4}$$

Since the mesh is uniform, the numerator of Eq. 6.4 is easily calculated by multiplying the total number of deleted elements to the surface area of the side of an 8-node brick element which is attached to the supports. For a square plate, Ψ is identical on all sides due to symmetry. If $\Psi = 0$, no elements are deleted, i.e. the plate deforms in mode I. Conversely, if $\Psi = 1$, all elements along the plate periphery are deleted.

Figure 6.8 gives the time-history of Ψ at different values of I^* for a typical square mild-steel plate by Nurick and Shave (1996). The FE model predicts

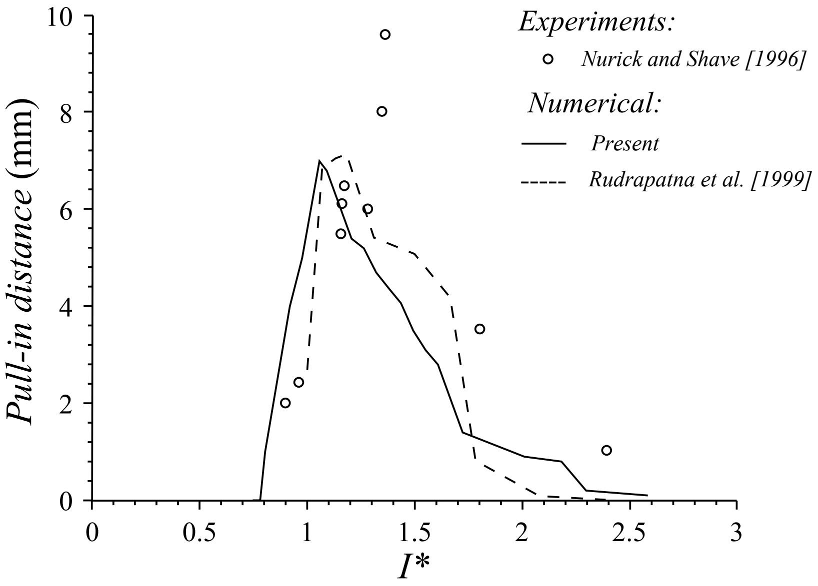

Figure 6.7: Side pull-in distance versus impulse for mild-steel plates ($\gamma = 1$). The mild steel properties of Nurick and Shave (1996) is used, see Table 6.2.

that an element is first deleted at $I^* = 0.69$ (it would *not* be possible to verify this experimentally) and through-thickness tearing occurs at a higher impulse of $I^* = 0.75$. Complete detachment from the supports occurs whenever $I^* \geq 0.98$, i.e. the critical impulse at mode II*→ IIa transition is $I^* = 0.98$. With increasing I^*, complete detachment occurs at increasingly earlier times of t/T as expected. Notice that Ψ is always less than unity even for high levels of impulse due to crack branching away from the boundary into the plate's interior. This will become clearer in Section 6.4.1.

A procedure to determine the critical impulse corresponding to mode IIb → III transition is now described. Figure 6.9a shows the time history of three typical stress triaxiality curves $\eta_{ave}(\bar{t})$; they are obtained by averaging the stress triaxiality of all the elements in the shaded region as shown. The width of $0.025b$ is chosen so that it covers the region of the plate where the cracks may conceivably propagate. Note that beyond $\bar{t}_0$, the non-dimensional time corresponding to $\eta_{ave} = 0$, the plate is completely detached from its supports. Conversely, if I^* is insufficient to cause complete detachment, then η_{ave} is always greater than zero.

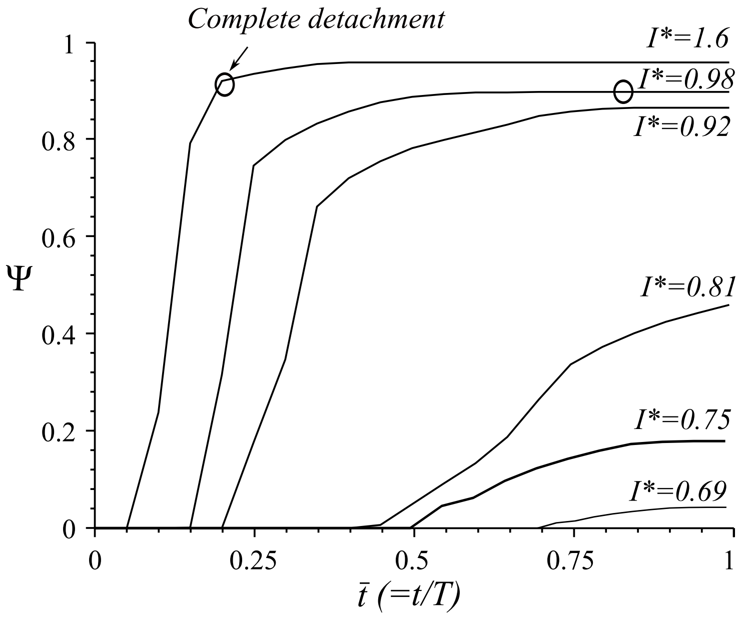

Figure 6.8: Time history of Ψ for different levels of I^*. ○ indicates the instant when plate is completely detached from its supports. Results shown are for a square mild-steel plate with a response time of $T = 120$ μs. The mild steel properties of Nurick and Shave (1996) is used, see Table 6.2.

At each impulse level, the time-averaged value of the function $\eta_{ave}(\bar{t})$, defined as

$$\bar{\eta} = \frac{\displaystyle\int_0^{\bar{t}_0} \eta_{ave}(\bar{t})\ \mathrm{d}\bar{t}}{\bar{t}_0} \tag{6.5}$$

This is obtained for the two different damage models, viz. ductile and shear, applied separately to give the curves shown in Fig 6.9b. A unique cross-over point can be identified which determines the transition from mode IIb → III. Beyond this cross-over point, only the shear damage model is used; otherwise, the ductile damage model is applied in a maximum sense. Using this proposed criterion, Table 6.4 compares the numerical critical impulses (and transitional velocities) with their experimental counterpart from literature. The predictions by FE are in good agreement with the experimental data given by Nurick and Shave (1996) and Olson et al. (1993). The predicted critical impulse is sensitive

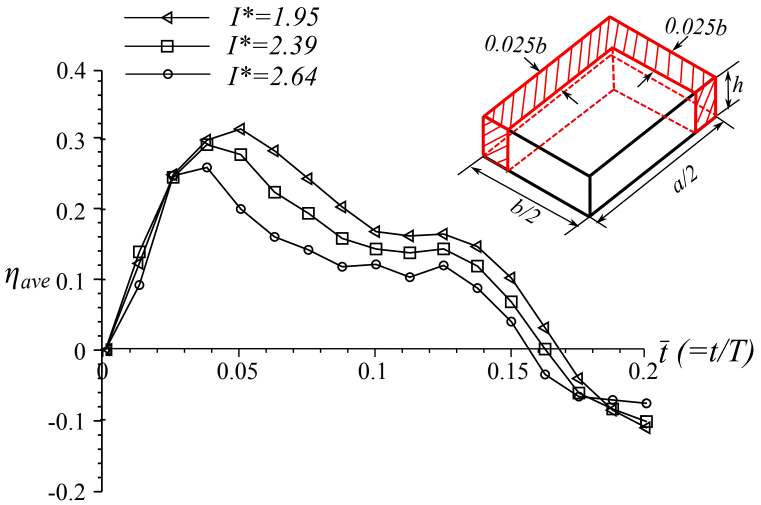

(a)

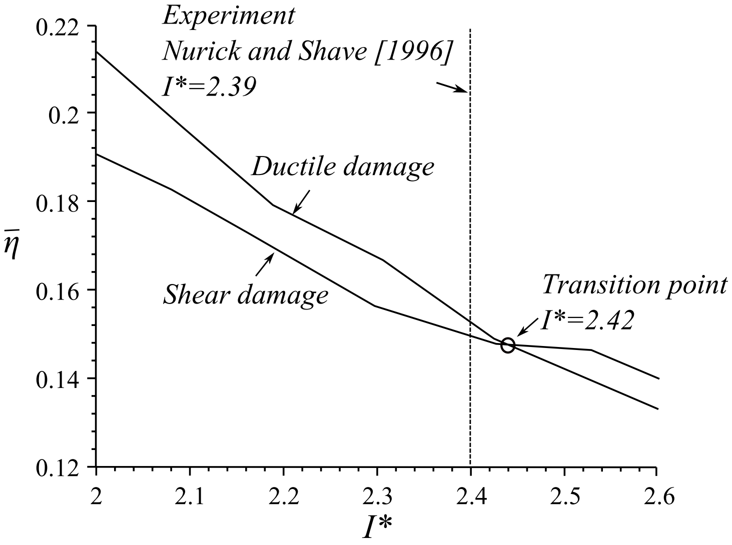

(b)

Figure 6.9: (a) Time history of stress triaxiality, η_{ave}, averaged over all elements in the shaded region, and (b) Comparison of the time-averaged stress triaxiality $\bar{\eta}$ for a plate using the ductile and shear damage model. Results shown are for a square mild-steel plate with a response time of $T = 120$ μs. The mild steel properties of Nurick and Shave (1996) is used, see Table 6.2.

to the parameters α and τ of the modified BC (Fig 6.1b). Since the FE model is calibrated to experimental data where the plate remains attached to the supports, the predicted critical impulse for mode IIa → IIb transition is much lower than that observed experimentally.

Table 6.4: Critical impulses I^* (and velocities V_0, m/s) corresponding to mode transitions.

Mode	Current FE	FE[1]	Experiments[2]	Experiments[3]
I → II*	0.75 (130.0)	0.97 (168.8)	0.62 (108.8)	-
II* → IIa	0.98 (172.0)	1.02 (177.5)	0.98 (171.3)	1.11 (193.5)
IIa → IIb	1.05 (184.0)	1.27 (221.0)	1.48 (257.0)	1.45 (251.9)
IIb → III	2.42 (421.0)	2.32 (404.7)	2.39 (416.2)	-

[1] (Rudrapatna et al., 1999) , [2] (Nurick and Shave, 1996) and [3] (Olson et al., 1993).

6.4 Predicted impulsive response

The fully validated FE model of the previous section is now employed to compute the zero-period impulsive response of rectangular plates with aspect ratio ranging between $2 \leq \gamma \leq 5$. All rectangular mild-steel plates modelled have the same total mass as the square ones (m_p = 0.0992 kg) used in Nurick and Shave (1996). Likewise, for their material properties listed in Table 6.2. The results for square mild-steel plates of Nurick and Shave (1996) are also included for comparison.

6.4.1 Deformation modes

Figure 6.10 shows that the current FE model successfully captures the different modes of impulsive response observed in a typical rectangular plate ($\gamma = 1.2$). Comparison is made here to the 'post-test' specimens of Ramajeyathilagam and Vendhan (2004) where a set of clear photographs are available, instead of with those given by Nurick and Shave (1996) and Olson et al. (1993). The zero-period, *uniform-momentum* idealisation is also valid in the work of Ramajeyathilagam

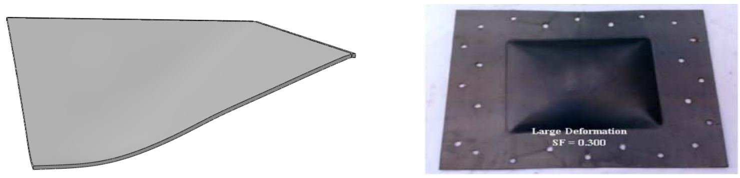

(a) Mode I ($I^* = 0.57$)

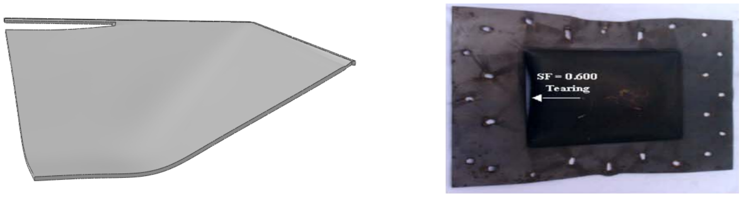

(b) Mode II* ($I^* = 0.98$)

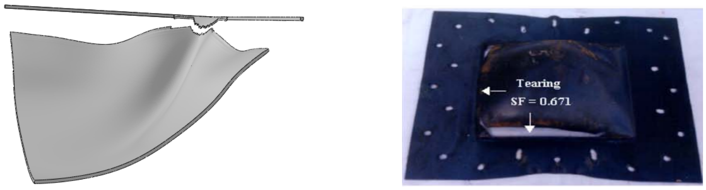

(c) Mode IIa ($I^* = 1.15$)

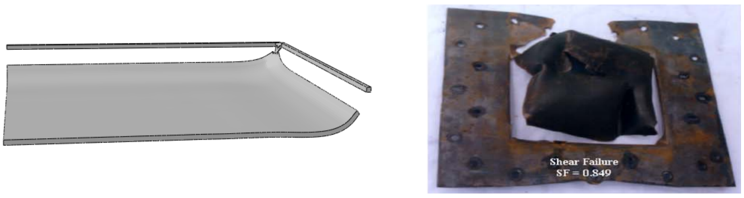

(d) Mode III ($I^* = 2.01$)

Figure 6.10: Comparison of predicted deformation modes (left column) for rectangular mild-steel plates ($\gamma = 1.2$) to the 'post-test' specimens (right column) of Ramajeyathilagam and Vendhan (2004). Note that the former shows a quarter of the rectangular plate due to symmetry. Properties of the mild-steel plates by Ramajeyathilagam and Vendhan (2004) are as follows: $\rho = 7860$ kg/m^3, $E = 210$ GPa, $\sigma_Y = 300$MPa. (Acknowledgement: Photographs - right column - were reproduced from Ramajeyathilagam and Vendhan (2004)).

and Vendhan (2004). For rectangular plates deforming in modes IIa and IIb, a crack propagates along each side of the plate boundary. At some point, their

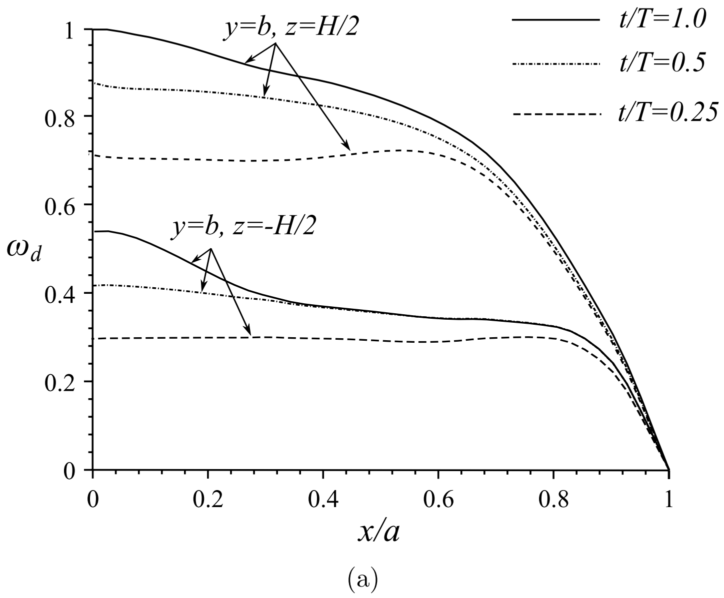

(a)

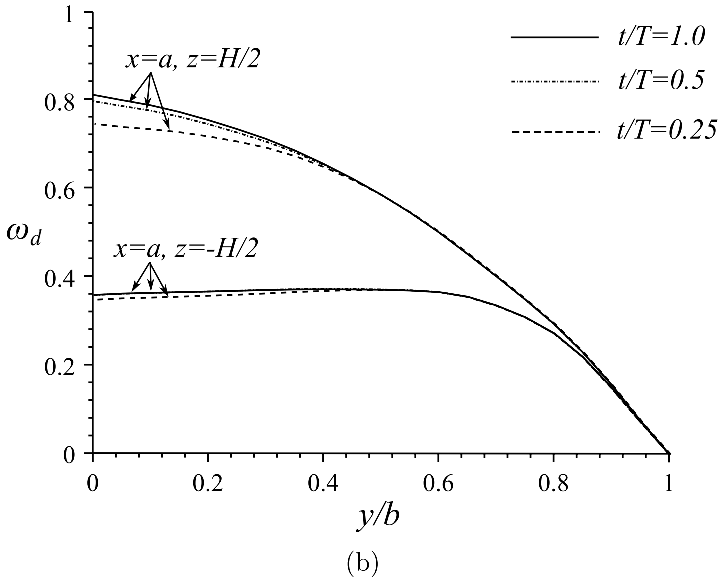

(b)

Figure 6.11: Ductile damage state variable ω_d for a rectangular plate with aspect ratio $\gamma = 2$ subjected to an impulse $I^* = 0.55$. The plate is deforming in mode I. The mild steel properties of Nurick and Shave (1996) is used, see Table 6.2.

crack paths are deflected inwards, circumventing the corner of the plate. When the two crack paths meet, complete plate detachment occurs. It is not entirely clear why the crack path deviates from the plate boundary as it approaches the corner although this occurs irrespective of the value of the aspect ratio. This is the reason why Ψ is always less than unity in Fig 6.8 regardless of the value of I^*.

Figure 6.11 shows the distribution of the state variable ω_d for a typical rectangular plate ($\gamma = 2$) subjected to a non-dimensional impulse $I^* = 0.55$. When $\omega_d = 1$, the material stiffness at that point begins to degrade in accordance to Eq. 6.3. It is noteworthy that ductile damage, by nucleation, growth and coalescence of voids, initiates well before the transition from mode I → II*. Current simulations showed that the first element to be deleted, i.e. the material point where its stiffness is fully degraded, always occurs at ($x = 0$, $y = b$, $z = H/2$), on the surface incident to the blast irrespective of I^*. It is, therefore, surprising to see in Fig 6.10b (right-side image) that tearing appears to initiate on the shorter side of the plate by Ramajeyathilagam and Vendhan (2004). This experimental anomaly must be due to material and/or geometric imperfections since it was, also, predicted that tearing must initiate at the mid-point of the longer side by the total and/or effective strain theory of Ramajeyathilagam and Vendhan (2004).

6.4.2 Types of mode II response

The mode II response of a plate was previously categorised as mode II* (through-thickness tearing at the supports), mode IIa (complete detachment from supports where central deflection *increases* with I^*) and mode IIb (complete detachment from supports where central deflection *decreases* with I^*) by Nurick and Shave (1996). However, the current FE simulations showed that non-through-thickness tearing typically precedes mode II*. In light of this, it is advantageous to re-classify the mode II response into three distinct types according to the magnitude of the non-dimensional impulse I^*, viz. Type 1 (non-through-thickness tearing), Type 2 (through-thickness tearing) and Type 3 (complete detachment from supports).

Figure 6.12 shows the equivalent plastic strain contour for a rectangular plate ($\gamma = 2$) subjected to different levels of impulse. At $I^* = 0.78$, Figure 6.12a shows that non-through-thickness tearing occurs along the supports, referred to

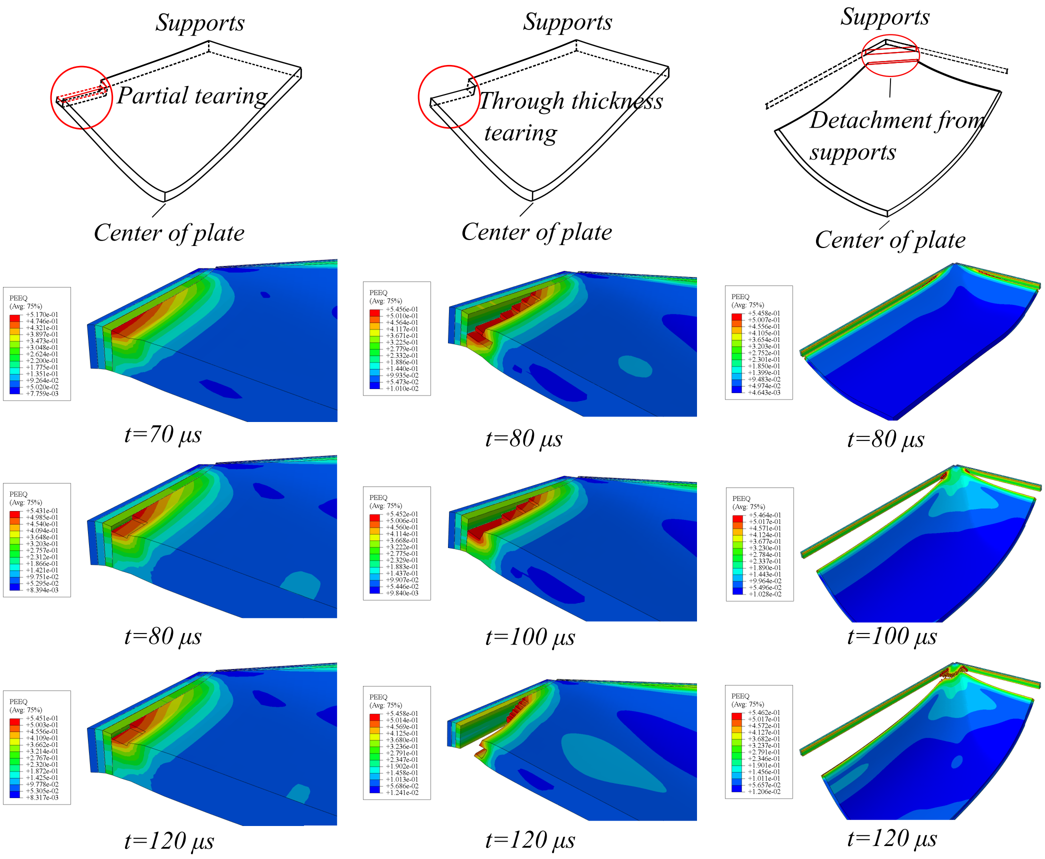

(a) Type 1 ($I^* = 0.78$) (b) Type 2 ($I^* = 0.85$) (c) Type 3 ($I^* = 1.04$)

Figure 6.12: Time evolution of the equivalent plastic strain contour in a rectangular mild steel plate ($\gamma = 2$) and the three types of mode II response predicted by the current FE model. Material properties are listed in Table 6.2. The mild-steel properties of Nurick and Shave (1996) is used.

as a Type 1 response hereinafter. By contrast, Type 2 response entails through-thickness tearing of the plate at the supports as depicted in Fig 6.12b. Figure 6.12c shows a typical Type 3 response where I^* is sufficiently large for complete detachment of the plate to occur. Notice the plate remnant at the corner of the supports caused by the deviation of the crack paths (Fig 6.12c) which is also evident in the experimental results shown in Fig 6.10c.

6.4.3 Failure maps

To ensure that comparison is made between plates of equal total mass and thickness, the aspect ratio (defined as the ratio of the longer to shorter side) is varied by choosing the longer and shorter sides of the plate to have length of $a\sqrt{\gamma}$ and $a/\sqrt{\gamma}$, respectively, where $a(= 0.0445$ m) is the half length of the square plate by Nurick and Shave (1996). In this manner, the plate thickness ($H = 1.6$ mm) and plate mass ($m_p = 0.0992$ kg) remain equal between plates of different aspect ratio γ. Figures 6.13 shows how the non-dimensional central deflection W_0/H varies with I^* for different aspect ratios ranging from $1 \leq \gamma \leq 5$. The overall trend of the central deflection with I^* is broadly similar to a square plate. For a plate deforming in modes I or II (Type 1 and 2), its central deflection reduces with increasing γ at a given I^*. By contrast, W_0/H is insensitive to γ. The increasing-decreasing trend of W_0/H with I^* is clearly evident in the mode II (Type 3) response. The FE results predict that the critical impulse at mode I$\rightarrow$ II (Type1) transition increases with aspect ratio γ, as seen in Fig 6.13. By contrast, the transition at mode II (Type 3) $\rightarrow$ III is insensitive to plate geometry but depends only on material properties.

Figure 6.15 shows a deformation map, constructed from the data in Fig 6.13. The contours of dotted line join constant value of W_0/H within that particular mode of deformation. This gives a map which is really useful to designers. Any pair of values of I^* and γ now locates a point on the map. From the map, one can determine the deformation mode and read off the mid-point deflection of the plate (by interpolation using two known values if required). Alternatively, it allows a designer to determine the critical impulse I^* delineating different modes of deformation, and the corresponding central deflection of the plate , at a

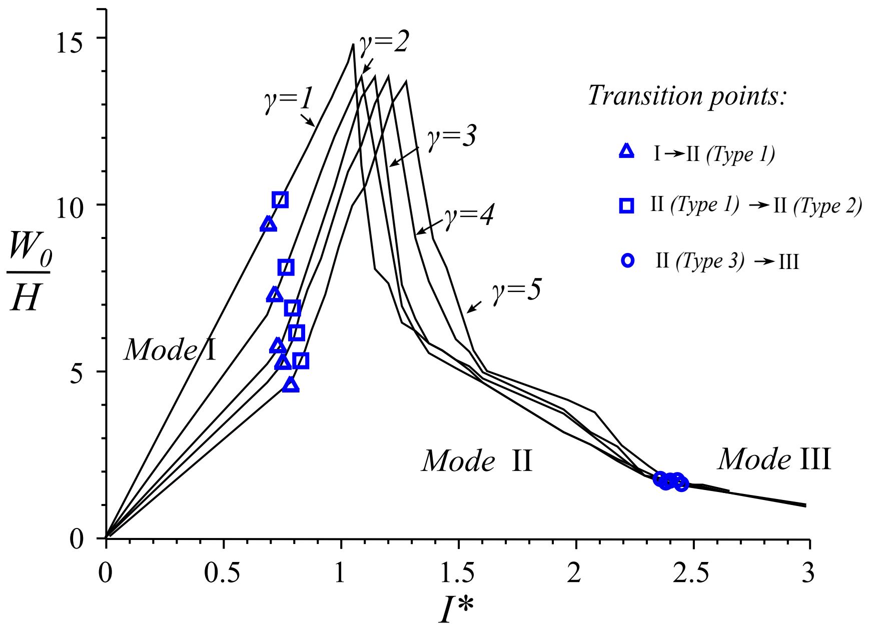

Figure 6.13: Variation of the maximum mid-point deflection with non-dimensional impulse I^* for rectangular plates with different aspect ratio. All the plates shown have the same thickness $H = 1.6$ mm and a total mass of $m_p = 0.0992$ kg. The mild steel properties of Nurick and Shave (1996) is used, see Table 6.2.

given aspect ratio γ. Note that the map assumes zero-period impulsive load (i.e. $t_d/T = 0$). For the corresponding finite-period loading case (i.e. $t_d/T \neq 0$), one would expect a lower central deflection at the same I^* and the boundaries in the deformation map of Fig 6.15 will change. This is explored in the next section for the case of a square plate.

Previously in Fig 6.15, the mass per unit area $\hat{m}_p(=\rho H)$ of all the plates were kept constant at $\hat{m}_p = 12.53$ kg/m^2. Let this be increased by a factor $k > 1$, from H to kH. To keep the same mass of $m_p = 0.0992$ kg between plates, its longer and shorter sides must be reduced accordingly to $a/\sqrt{k}$ and $b/\sqrt{k}$, respectively. The effects of plate thickness (or mass per unit area $\hat{m}_p$) upon the deformation mode are explored in this manner. Figure 6.14a shows how the boundaries, delineating the different modes, shift with the factor k. At a given γ,

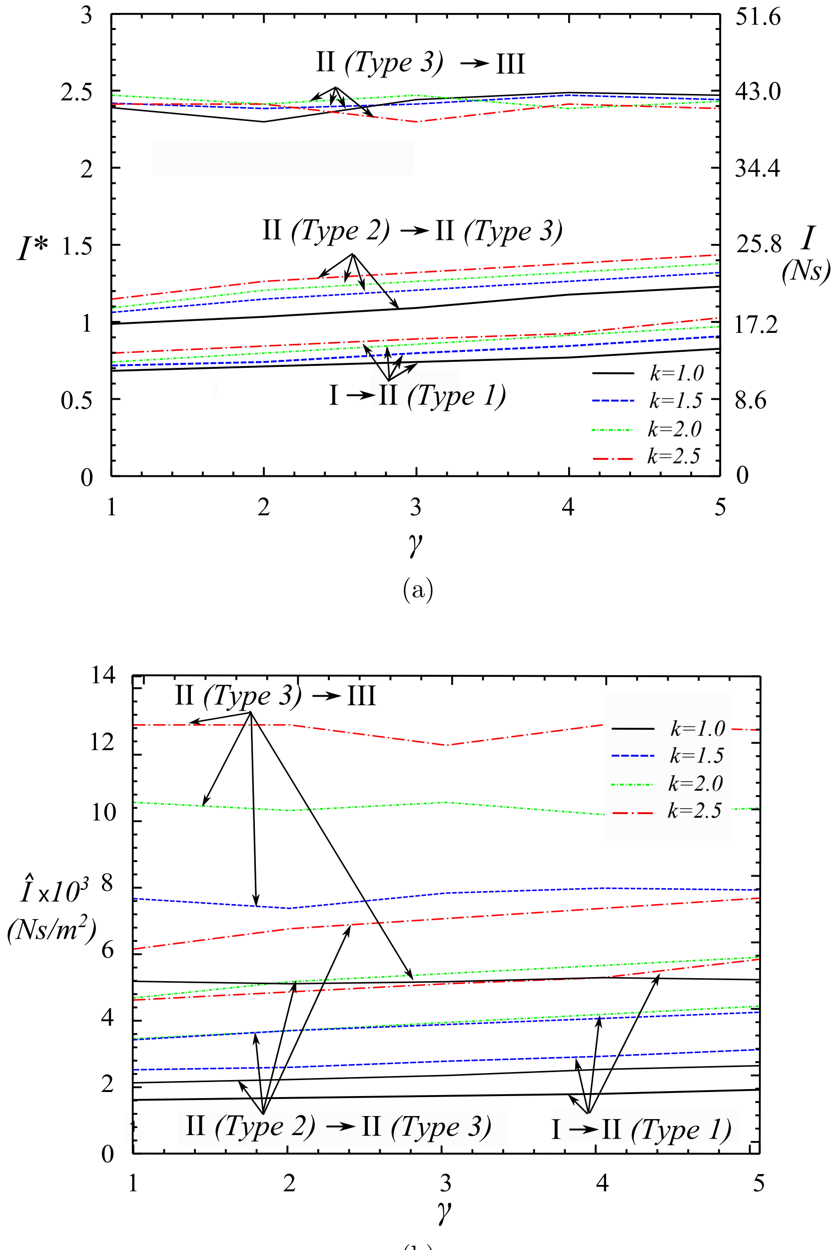

(a)

(b)

Figure 6.14: Deformation maps showing the changing boundaries according to different plate thickness H. The mild steel properties of Nurick and Shave (1996) is used, see Table 6.2.

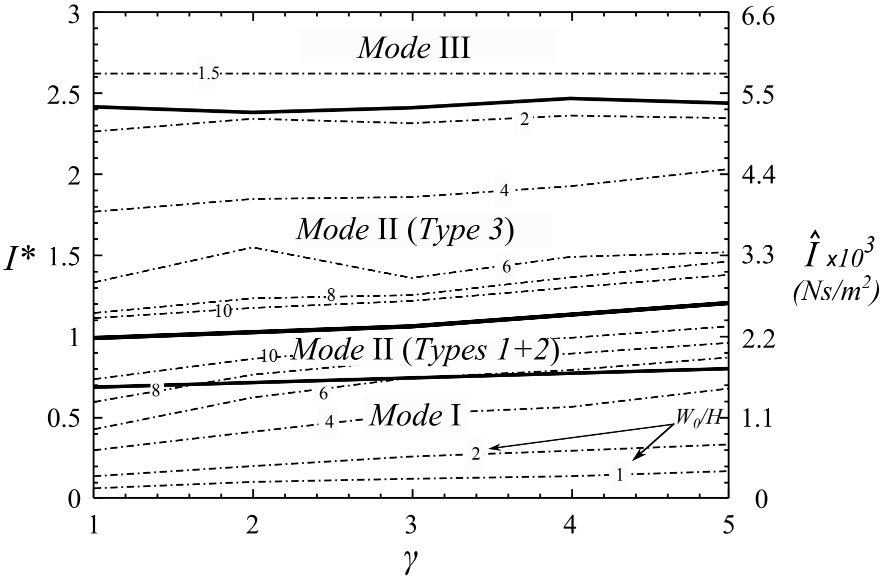

Figure 6.15: Deformation map for a rectangular mild-steel plate with a constant mass per unit area of $\hat{m}_p = 12.53$ kg/m^2 and a total mass of $m_p = 0.0992$ kg. The mild steel properties of Nurick and Shave (1996) is used, see Table 6.2.

the critical impulse I^* at the transition from mode I → II(Types 1+2) and from mode II(Types 1+2) → II(Type 3) increases with plate thickness. By contrast, the boundaries corresponding to mode II(Type 3) → III transition do not appear to change significantly which is consistent with the fact that the corresponding transitional impulse I^* depends only on material properties. On the other hand, Figure 6.14b re-plots the deformation map for $\hat{I}$ (impulse per unit area) versus γ. Increasing k (or the plate thickness) leads to a corresponding increase in $\hat{I}$ which is consistent with Fig 6.14b.

6.5 Effects of finite-period impulse upon the damage mode

Xue and Hutchinson (2003, 2004) have previously shown that the ratio of the blast duration to the overall response time of the structure (t_d/T) determines whether the blast loading may be approximated as a zero-period, *uniform-momentum* impulse. In this section, results from numerical simulations are presented which examine the influence of t_d/T upon the deformation mode of square mild-steel plates.

Figure 6.16a shows the effect of increasing t_d/T upon the area fraction of plate (Ψ) that becomes detached from the supports. Note that the plate is loaded by a zero-period impulse at $t_d/T = 0$. The results show that for the same non-dimensional impulse of $I^* = 0.92$, Ψ decreases with increasing blast duration. If $t_d/T > 0.9$, the mode of deformation switches from mode II(Types 1 or 2) to mode I. Hence, the response of the plate is also dependent upon the non-dimensional blast duration t_d/T.

Figure 6.16b shows how the boundaries corresponding to the transition from mode II(Types 1+2) $\rightarrow$ II(Type 3) and from mode II(Type 3) $\rightarrow$ III shifts in accordance to the blast duration. Increasing the blast duration has an effect of delaying the transition between deformation modes. For instance, a square plate which was previously deforming in mode II(Type 3) at $I^* = 1.5$, under the action of a zero-period impulse, now deforms in mode II(Type 1 or 2) if $t_d/T \geq 2.0$. In a similar vein, the plate deforms in mode II(Type 3) instead of mode III at $I^* = 2.5$ if $t_d/T \geq 3.0$.

6.6 Conclusion

FE model is developed in this chapter to study the dynamic response of plates, subjected to impulsive loading for which experimental data on the permanent inelastic deformation and post-damage observations were available. FE model validations have been performed against a wide range of aspect ratio of plates and non-dimensional impulse I^* as given in the blast tests. In particular, the non-convergence of key local stresses near the plate boundary, due to stress singularities, has been addressed which, subsequently, allowed ductile fracture along the plate boundary to be modelled, within the framework of damage mechanics, using finite elements.

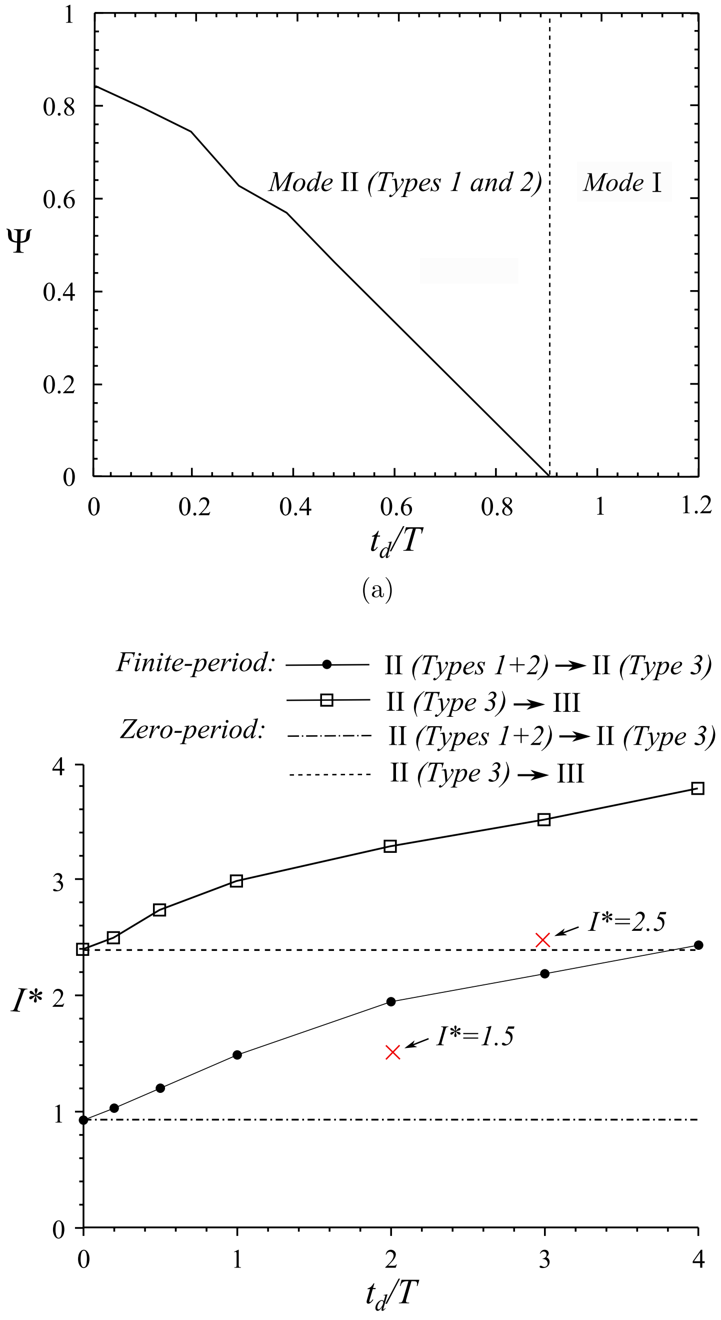

(a)

(b)

Figure 6.16: (a) Influence of blast duration t_d/T upon the area fraction of plate Ψ that becomes detached from the supports; (b) Effects of the blast duration upon the boundaries corresponding to the transition from mode II(Types 1+2) $\rightarrow$ II(Type 3) and from mode II(Type 3) $\rightarrow$ III. Results shown are for square mild-steel plate subjected to a non-dimensional impulse of $I^* = 0.92$. The mild steel properties of Nurick and Shave (1996) is used, see Table 6.2.

After validating the proposed FE model, the parametric study reveals a number of key features regarding the impulsive response of rectangular plates as follows: (i) the impulsive mode II response has been reclassified into three distinct types, depending on whether tearing initiates at the supports; (ii) the central deflection of a rectangular plate deforming in modes I and II (Types 1+2) decreases with aspect ratio for the same I^*; (iii) with increasing plate aspect ratio and thickness, a higher non-dimensional impulse I^* is needed to cause non-through-thickness and through-thickness tearing at the supports; (iv) the mode III response is insensitive to aspect ratio γ and plate thickness. For thin plates, the critical impulse for transition to mode III transition is a function of material properties; and (v) an increase in the blast duration delays the transition between deformation modes for plates of the same dimensions and subjected to the same non-dimensional impulse I^*.

Chapter 7

Discussions, conclusions and further research

7.1 Discussions and conclusions

An understanding of the response of structures to intense blast loadings is important to the nuclear, offshore and defence industries. Blast loadings can be broadly classified as impulsive or non-impulsive depending on the ratio of the loading duration to the natural response time of the structure with which it interacts. A thorough literature review indicates that our current state of knowledge on the dynamic response (i.e. large deformation, damage and failure) of elasto-plastic structures under non-impulsive loadings is relatively under-developed; and, it is also unclear how large elasto-plastic deformation and failure at the supports affect the previously known results on fluid-structure interaction (FSI). This thesis investigates the response of elasto-plastic structural members, viz. beams and rectangular plates, to both impulsive and non-impulsive loadings and the effects of FSI on their performance underwater and in air. Based on the results and analyses presented in Chapters 2-6, this chapter summarises some of the important conclusions that can be drawn from the studies.

7.1.1 A general elasto-plastic structural beam system

An elasto-plastic structural beam model was developed which is sufficiently general to capture large elasto-plastic deformation; incorporate the interactions between bending, membrane stretch and transverse shear in the yield and plastic limit functions; model the structural failure through progressive damage and its subsequent detachment; and, account for general (impulsive and non-impulsive) loading conditions. The analytical model is validated against existing experiments for impulsively loading cases and is validated against present FE simulations for non-impulsively loading cases.

7.1.2 Effects of pulse duration and pulse shape on deformation and failure of elasto-plastic beams

The results presented in Chapter 3 revealed the following: (i) There is a broadly similar overall trend for the mid-span deflection with non-dimensional impulse I^* for both impulsive and non-impulsive load cases, i.e. mid-span deflection W_0/H increases initially before reducing with I^*; (ii) For a given I^*, the mode I deflection reduces with increasing t_d whilst the reverse occurs in mode II and III; (iii) The mid-span deflection at mode I→II transition is not sensitive to t_d; (iv) Increasing pulse duration t_d leads to greater critical non-dimensional impulse at mode I→II and mode II→III transitions; (v) Mode III deflection for non-impulsive loads are considerably higher than its corresponding impulsive counterpart at the same I^*; (vi) The non-dimensional shear energy $\bar{E}_S^s$ reduces while the non-dimensional membrane energy $\bar{E}_S^m$ increases with increasing pulse duration t_d at the same I^*; (vii) The residual momentum and energy in mode II and III reduce dramatically for a given I^* with longer pulse duration t_d and (viii) Youngdahl (1970, 1971)'s approach can successfully eliminate the dependence of the mid-span deflection to pulse shape effects for monotonically decaying, impulsive and non-impulsive, loadings. However, the same approach would under-predict the mode I mid-span deflection when the loading is non-impulsive and non-monotonically decaying.

7.1.3 Effects of fluid-structure interaction (FSI) in water and air

The results (in Chapters 4 and 5) showed that the deflection associated with various modes of deformation for a clamped elasto-plastic beam, substantially influence the beneficial effect of FSI in both incompressible and compressible mediums. In underwater explosions, increasing non-dimensional impulse I^* leads to a substantial decrease in non-dimensional maximum transmitted impulse after mode I→II transition, because a significant proportion of the impulse is transmitted to the beam during elastic rebound in mode I. Both the maximum transmitted impulse $\bar{I}^T$ and energy $\bar{E}^T$ reduces monotonically with non-dimensional impulse I^* in modes II and III, since the time it takes for complete detachment to occur reduces with I^*.

In air blasts, the FSI effect of reducing the load acting on the elasto-plastic beams is evident during structural response at all modes of deformation; this is due to the alleviation of interface pressure by the rapid motion of the beam. The over-predictions of maximum mid-span deflection, maximum transmitted impulse and energy by ignoring FSI effects are considerable in mode I deformation, but are negligible in mode II and III deformations. The influence of the structural and blast pressure wave parameters on the importance of FSI is studied for elasto-plastic beams during mode I deformation. It is found that the error - in predicting structural response when FSI is not considered - increases monotonically, (i) when the maximum mid-span velocity increases relative to the shock speed; (ii) as the time (when the maximum mid-span deflection is reached) decreases relative to the pulse duration; or (iii) when the beam has less mass per unit area.

7.1.4 Sensitivity of blast response of elasto-plastic beams to beam aspect ratio and mass

The variations of maximum impulse and energy transfer to beam mass per unit area, or FSI index (β_w in water and β_s in air) and beam aspect ratio L/H is investigated. The key findings for the incompressible and compressible mediums are as follows. In underwater explosions, an increase of beam aspect ratio L/H or decrease of FSI index β_w (more mass per unit area) always leads to a reduction of maximum transmitted impulse in mode I, and an increase of FSI index β_w results in a reduction of maximum transmitted impulse in mode II and III. In air blast, the elasto-plastic beam acquires less transmitted impulse, with increasing aspect ratio L/H or FSI index β_s in mode I, and with increasing FSI index β_s in mode II and III.

7.1.5 The effects of supports upon the FSI phenomenon

The analysis of structures loaded by underwater blast or air blast is often done by adopting the analysis of Taylor (1941) and Kambouchev et al. (2007) (which will subsequently be referred to as the KNR theory) based on rigid, free-standing structures and ignoring the effect of boundary condition. Employing the aforementioned solutions for elasto-plastic beams could lead to large inaccuracies on the maximum impulse transmitted. The key findings for the effects of boundary on FSI are as follows. In underwater explosions, Taylor's solution under predicts the maximum transmitted impulse and energy for elasto-plastic beams for all modes of deformation. In air blast, KNR's solution would over-estimate the maximum transmitted energy but under-estimate the maximum transmitted impulse for elasto-plastic beams deforming in all three modes, despite some notable cases in mode III where it over-predicts the maximum transmitted impulse.

7.1.6 Deformation and failure of rectangular plates

Deformation and failure of fully-clamped rectangular plates have been investigated. A 3D FE model is developed which is capable of modelling the blast response of rectangular mild-steel plates for a wide range of aspect ratios and non-dimensional impulse. Predictions by the FE model are shown to be in good agreement with experimental results. Parametric studies are carried out to reveal the key features of impulsive and non-impulsive response of rectangular plates. In particular, the impulsive mode II response has been reclassified into three distinct types, depending on whether tearing initiates at the supports, viz. Type 1 (non-through-thickness tearing), Type 2 (through-thickness tearing) and Type 3 (complete detachment from supports). Increasing plate aspect ratio and thickness leads to a higher non-dimensional impulse I^* that is needed to cause nonthrough-thickness (Type 1) and through-thickness tearing (Type 2) at the supports. An increase in the blast duration delays the transition between deformation modes for plates of the same dimensions and subjected to the same non-dimensional impulse I^*. Deformation maps are constructed which allow the maximum central deflection of rectangular plates to be read off for different combinations of blast impulse and aspect ratio, and vice-versa.

7.2 Further research

The findings presented in this thesis collectively provide some new insights into blast response of structures. The analysis of dynamic response of elasto-plastic beams under non-impulsive loading improves the understanding of loading duration upon structural deformation and subsequent failure. The examination of fluid-structure interaction for elasto-plastic structures in air and water explosion underpins the understanding of the outcome of FSI associated with different modes of deformation. Despite the comprehensive studies of these important aspects, some parts in this research still require more thorough investigation, leading to the following suggestions for future research:

1. The current structural beam model is developed and validated for beams made of aluminium 6061 T6 which can be considered as strain-rate insensitive. Chapter 6 shows that neglecting material strain rate sensitivity would lead to significantly over-prediction of central deflection for plates made by materials like mild steel. Future work could incorporate the strain-rate effect into the present structural beam model.

2. In the present structural beam model, the length of the plastic hinge is held constant following the analytical procedure by Jones (1976). Shen and Jones (1992) suggested an empirical relation, where the plastic hinge length changes inversely with the applied impulse. Figure 3.7 in Chapter 3 shows that predictions by Shen and Jones (1992) agree better against experimental data compared to the current analytical predictions. Further work can be carried out in establishing the relationship of hinge length with loading intensity to improve the accuracy of the present analytical model.

3. The present analysis of FSI in underwater explosion neglected the influence of the reflection wave from the closing front in a *Type I* cavitation event (i.e. the breaking front travelling in the positive Z-direction, always arrests before it reaches the fluid-structure interface and inverts its motion as a closing front). Several authors (Schiffer and Tagarielli, 2014, 2015) have found that in a *Type I* cavitation event, breaking shock fronts that eventually strike the target structure always contribute to the transmitted impulse. Current analytical model under-predicts by up to 13.4% of the maximum transmitted impulse compared to present FE predictions. Thus, it would be worthwhile to include the effect of breaking shock front as an extension to the current analytical model.

4. The transmitted impulse of the free-standing plate is often normalised by a function of a single non-dimensional parameter (better known as the FSI index) which characterises the relative time scale of structure and loading (Taylor, 1941; Kambouchev et al., 2006; Hutchinson, 2009). It was found (in Chapters 4 and 5) that the blast response of elasto-plastic structure is govern by beam aspect ratio and its mass per unit area, quantified by the FSI index. Future work should investigate the possibility of finding a re-normalisation for the transmitted impulse of elasto-plastic structure, including both beam aspect ratio and beam mass per unit area, expressed in terms of a single non-dimensional parameter.

5. For rectangular plates deforming in modes IIa and IIb, a crack propagates along each side of the plate boundary. At some point, these crack paths are deflected inwards, circumventing the corner of the plate. When the two crack paths meet, complete plate detachment occurs. It lacks an explanation of why the crack path deviates from the plate boundary as it approaches the corner and this occurs irrespective of the value of the aspect ratio. Similarly, it remains unclear why failure occurs before all the elements at the supports are deleted regardless of the value of impulse. Thus, it would be worthwhile to investigate the crack propagation in rectangular plates subjected to impulsive loadings to elucidate the aforementioned.

Page left empty

Appendix A
The finite difference numerical method

Following closely the algorithmic approach by Drumheller (1998), the domain of interest is discretised into N equally spaced points. The simulations (in chapter 5) have been carried out with between 2000 and 4000 mesh points, depending on the problem. The coordinates of these points are given by $x^0_{e(n)} = X_{(n)} = (n - N)\Delta X$, where $n = 1, 2, ..., N$ is the point number and $\Delta X = (d_0 + d)/(N - 1)$ is the grid spacing. Time is discretised into variable time steps Δt^k, $j = 1, 2, ...$ and the discretised solution is obtained at time $t^0 = 0, t^1, ..., t^{k-1}$, $t^k = t^{k-1} + \Delta t^k$,... The finite difference approximation for particle velocity leads to

$$x^{k+1}_{e(n)} = x^k_{e(n)} + \Delta t^{k+1} v^{k+\frac{1}{2}}_{(n)} \tag{A-1}$$

where the velocity v is computed in the middle of the time intervals,

$$v^{k+\frac{1}{2}}_{(n)} = v^{j-\frac{1}{2}}_{(n)} + \frac{1}{2}(\Delta t^k + \Delta t^{k+1}) a^k_{(n)} \tag{A-2}$$

where the time step is averaged over the current and previous time step and the velocity is defined only in the middle of the time steps. The acceleration for previous equation is obtained from the momentum conservation equation:

$$a^k_{(n)} = -\frac{1}{\rho^0_{(n)}} \frac{p^k_{(n+\frac{1}{2})} - p^k_{(n-\frac{1}{2})}}{\Delta X} \tag{A-3}$$

The rest of the discretised equations are as follows:

$$p^{k+1}_{(n+\frac{1}{2})} = (\gamma - 1)\rho_a \frac{e^{k+1}_{(n+\frac{1}{2})}}{F^{k+1}_{(n+\frac{1}{2})}} - \Theta^{k+\frac{1}{2}}_{(n+\frac{1}{2})} \tag{A-4}$$

$$\Theta^{k+\frac{1}{2}}_{(n+\frac{1}{2})} = -\rho_a \Big(K_1 \Delta x^{k+\frac{1}{2}}_{(n+\frac{1}{2})} d^{k+\frac{1}{2}}_{(n+\frac{1}{2})} \Big)^2 - \rho_a K_2 c^k_{(n+\frac{1}{2})} \Delta x^{k+\frac{1}{2}}_{(n+\frac{1}{2})} |d^{k+\frac{1}{2}}_{(n+\frac{1}{2})}| \tag{A-5}$$

$$c^k_{(n+\frac{1}{2})} = \sqrt{\gamma(\gamma-1) e^k_{(n+\frac{1}{2})}} \tag{A-6}$$

$$d^{k+\frac{1}{2}}_{(n+\frac{1}{2})} = \frac{2}{\Delta t^{k+1}} \frac{F^{k+1}_{(n+\frac{1}{2})} - F^k_{(n+\frac{1}{2})}}{F^{k+1}_{(n+\frac{1}{2})} + F^k_{(n+\frac{1}{2})}} \tag{A-7}$$

$$\Delta x^{k+\frac{1}{2}}_{(n+\frac{1}{2})} = \frac{1}{2} \Big(x^{k+1}_{e(n+1)} - x^{k+1}_{e(n)} + x^k_{e(n+1)} - x^k_{e(n)} \Big) \tag{A-8}$$

$$e^{k+1}_{(n+\frac{1}{2})} = \frac{e^k_{(n+\frac{1}{2})} + \Big(\frac{1-\gamma}{2} e^k_{(n+\frac{1}{2})} + \frac{\Theta^{k+\frac{1}{2}}_{(n+\frac{1}{2})}}{\rho^{k+\frac{1}{2}}_{(n+\frac{1}{2})}} \Big) \Delta t^{k+1} d^{k+\frac{1}{2}}_{(n+\frac{1}{2})}}{1 + \frac{\gamma-1}{2} \Delta t^{k+1} d^{k+\frac{1}{2}}_{(n+\frac{1}{2})}} \tag{A-9}$$

$$\rho^{k+\frac{1}{2}}_{c(n+\frac{1}{2})} = \frac{\rho^0_{c(n+\frac{1}{2})}}{2} \Big(\frac{1}{F^{k+1}_{(n+\frac{1}{2})}} + \frac{1}{F^k_{(n+\frac{1}{2})}} \Big) \tag{A-10}$$

$$\rho^0_{c(n+\frac{1}{2})} = \frac{\rho^0_{c(n+1)} + \rho^0_{c(n)}}{2} \tag{A-11}$$

where the discrete deformation gradient F is given by

$$F^k_{(n+\frac{1}{2})} = \frac{x^k_{e(n+1)} - x^k_{e(n)}}{\Delta X}. \tag{A-12}$$

The solution process consist of applying the following steps to each node n in the domain ($n = 0, ..., N-1$) except the last one $n = N$ which is treated separately - the details will be given later. The initialisation of the simulation at $k = 0$ is to prescribe the following initial velocity field to the compressed air container and ambient air container,

$$\begin{aligned} v^{\frac{1}{2}}_{(n)} &= v_0 e^{-(x^0_{e(n)}/d_0)^2}, \quad x^0_{e(n)} \leq d_0 \\ v^{\frac{1}{2}}_{(n)} &= 0, \quad x^0_{e(n)} > d_0. \end{aligned} \tag{A-13}$$

The initial density field follows immediately from Eq. 5.2,

$$\rho^0_{(n)} = \left[1 + \frac{\gamma - 1}{2}\Big(\frac{v^{\frac{1}{2}}_{(n)}}{c_a}\Big)^2\right]^{1/(\gamma-1)}, \quad x^0_{e(n)} \leq d_0 \qquad \text{(A-14)}$$
$$\rho^0_{(n)} = 0, \quad x^0_{e(n)} > d_0.$$

The first step in each time iteration is to compute the stable time step size:

$$\Delta t^k = \alpha\left[\min\left(\frac{x^{k-1}_{e(n)} - x^{k-1}_{e(n-1)}}{c^{k-1}_{(n-1)}}\right)\right] \qquad \text{(A-15)}$$

where the minimum is taken over all possible values of n and $0 \leq \alpha \leq 1$ is an appropriately chosen time factor. Note that the time step at $j = 1$ is $\Delta t^k = \alpha\Delta X/c_a$. This step is followed by the computation of deformation gradient $F^k_{(n+\frac{1}{2})}$ (Eq. A-12), the deformation rate $d^{k+\frac{1}{2}}_{(n+\frac{1}{2})}$ (Eq. A-7) and the Eulerian spacing $\Delta x^{k+\frac{1}{2}}_{(n+\frac{1}{2})}$ (Eq. A-8). From these the viscous dissipation $\Theta^{k+\frac{1}{2}}_{(n+\frac{1}{2})}$ (Eq. A-5) and the internal energy $e^{k+1}_{(n+\frac{1}{2})}$ (Eq. A-9) can be computed. At the next step the pressure $p^{k+1}_{(n+\frac{1}{2})}$ is obtained from Eq. A-4 and substituted into the expression of acceleration $a^k_{(n)}$ (Eq. A-3). The cycle for the time step is completed by computing the velocity $v^{k+\frac{1}{2}}_{(n)}$ (Eq. A-2) and particle location $x^{k+1}_{e(n)}$ (Eq. A-1). Node N at $X = d_0 + d$ is treated independently as three different cases in each simulation:

1. a free moving air particle, whose equation of motion is represented by Eqs. A-1, A-2 and A-3;
2. a reflective, clamped, rigid wall with boundary condition of $x^{k+1}_{e(N)} = v^{k+\frac{1}{2}}_{(N)} = 0$ and
3. an elasto-plastic beam whose equation of motion can be obtained by substituting interface pressure $p_{\text{Int}} = p^{k+1}_{(N+\frac{1}{2})} - p_a$ into Eq. 2.28.

Bibliography

ABAQUS/Explicit. *User's Manual Version 6.10*, 2012.

Alves, M. and Jones, N. Impact failure of beams using damage mechanics: Part i - analytical model. *Int J Impact Eng*, 27:837–861, 2002a.

Alves, M. and Jones, N. Impact failure of beams using damage mechanics: Part ii - application. *Int J Impact Eng*, 27:863–890, 2002b.

American Society of Civil Engineering. *Design of Structures to Resist Nuclear Weapons Effects.* New York: American Society of Civil Engineers, 1961.

American Society of Civil Engineering. *Design of Structures to Resist Nuclear Weapons Effects.* New York: American Society of Civil Engineers, 1985.

Anderson, J. *Fundamentals of aerodynamics.* New York: McGraw-hill, 2001.

Baker, W. E. *Explosions in Air.* Austin: University of Texas Press, 1973.

Baker, W. E., Cox, P. A., Westine, P. S., Kulesz, J. J., and Strehlow, R. A. *Explosion Hazards and Evaluation.* New York: Elsevier Scientific Publishing Company, 1983.

Biggs, J. *Introduction to Structural Dynamics.* New York: McGraw-hill, 1964.

Blom, F. J. A monolithical fluid-structure interaction algorithm applied to the piston problem. *Comput Meth Appl Mech Eng*, pages 223–24, 1998.

Blom, F. J. and Leyland, P. Analysis of fluid-structure interaction on moving airfoils by means of an improved ale-method. *AIAA*, pages 97–1770, 1997.

Brode, H. L. Numerical solution of spherical blast waves. *J Appl Mech*, 26: 766–775, 1955.

Christopherson, D. G. Structural defence. Technical report, Ministry of Home Security, Research And Experiments Department, 1945.

Deshpande, V. S. and Fleck, N. A. One-dimensional response of sandwich plates to underwater shock loading. *J Mech Phys Solids*, 53:2347 – 2383, 2005.

Deshpande, V. S., Heaver, A., and Fleck, N. A. An underwater shock simulator. *Proc R Soc A*, 462:1021–1041, 2006.

Dewey, J. M. The air velocity in blast waves from tnt explosions. *Proc R Soc A*, pages 366–385, 1964.

Dharmasena, K. P., Queheillalt, D. T., Wadley, H. N. G., Dudt, P., Chen, Y., Knight, D., Evans, A. G., and Deshpande, V. S. Dynamic compression of metallic sandwich structures during planar impulsive loading in water. *Euro J Mech - A/Solids*, 29:56–67, 2010.

Dharmasena, K. P., Wadley, H. N. G., Williams, K., Xue, Z., and Hutchinson, J. W. Response of metallic pyramidal lattice core sandwich panels to high intensity impulsive loading in air. *Int J Impact Eng*, 38:275–289, 2011.

Drumheller, P. S. *Introduction to Wave Propagation in Nonlinear Fluids and Solids*. Cambridge: Cambridge University Press, 1998.

Ebrahimi, H. and Vaziri, A. Metallic sandwich panels subjected to multiple intense shocks. *Int J Solids Struct*, 50:1164 – 1176, 2013.

Fallah, A. S. and Louca, L. A. Pressure-impulse diagrams for elastic-plastic-hardening and softening single-degree-of-freedom models subjected to blast loading. *Int J Impact Eng*, 34:823–842, 2007.

Fallah, A. S., Nwankwo, E., and Louca, L. A. Pressure-impulse diagrams for blast loaded continuous beams based on dimensional analysis. *ASME*, 80: 051011, 2013.

Feng, Z., Zhao, L., Lu, G., and Wang, Z. Deformation and failure of blast-loaded metallic sandwich panels-experimental investigations. *Int J Impact Eng*, 35: 937–951, 2007.

Fischer, K. and Haring, I. Sdof response model parameters from dynamic blast loading experiments. *Eng Struct*, 31:1677–1686, 2009.

Fleck, N. A. and Deshpande, V. S. The resistance of clamped sandwich beams to shock loading. *ASME J Appl Mech*, 71:386–401, 2004.

Gupta, N. K., Kumar, P., and Hegde, S. On deformation and tearing of stiffened and un-stiffened square plates subjected to underwater explosion-a numerical study. *Int J Mech Sci*, 52:733–744, 2010.

Hancock, J. W. and Mackenzie, A. C. On the mechanisms of ductile fracture in high-strength steels subjected to multi-axial stress states. *J Mech Phys*, 24: 1471–1469, 1976.

Hayhurst, D. R., Hutchinson, J. W., McMeeking, R. M., Liang, Y., Spuskanyuk, A. V., Evans, A. G., and Flores, S. E. The response of metallic sandwich panels to water blast. *J Appl Mech*, 74:81–99, 2005.

Henrych, J. *The Dynamics of Explosion and Its Use.* Amsterdam: Elsevier Scientific Publishing Company, 1979.

Hutchinson, J. W. Energy and momentum transfer in air shocks. *ASME J Appl Mech*, 76:051307, 2009.

Hutchinson, J. W. and Xue, Z. Metal sandwich plates optimized for pressure impulses. *Int J Mech Sci*, 47:545–569, 2005.

Izzuddin, B. A. A simplified model for axially restrained beams subject to extreme loading. *Int J Steel Struct*, 5:421–429, 2005.

Johnson, G. R. and Cook, W. H. A constitutive model and data for metals subjected to large strains, high strain rates and high temperatures. In *Proceedings of 7th International Symposium on Ballistics, Netherlands, pp. 541*, 1983.

Jones, N. A theoretical study of the dynamic plastic behaviour of beams and plates with finite-deflections. *Int J Solids Struct*, 7:1007–1029, 1971.

Jones, N. A literature review of the dynamic plastic response of structures. *Shock and Vibration Digest*, 98:131–136, 1975.

Jones, N. Plastic failure of ductile beams loaded dynamically. *Transactions of the ASME J Eng Ind*, B1:131–6, 1976.

Jones, N. Recent progress in the dynamic plastic behaviour of structures parts i and ii. *Shock and Vibration Digest*, 10:21–23, 1978.

Jones, N. Recent progress in the dynamic plastic behaviour of structures parts iii. *Shock and Vibration Digest*, 13:3–16, 1981.

Jones, N. Recent progress in the dynamic plastic behaviour of structures parts iv. *Shock and Vibration Digest*, 17:273–291, 1985.

Jones, N. *Structural Impact*. Cambridge: Cambridge University Press, 1989.

Jones, N. ”Recent Progess in Structural impact” In *Proc. Speciality Symposium on Structures Response to Impact and Blast*. Elsevier Science Pub, 1996.

Jones, N. Some recent developments in the dynamic inelastic behaviour of structures. *Ships and Offshore Structures*, 1:37–44, 2006.

Jones, N. Dynamic inelastic response of strain rate sensitive ductile plates due to large impact, dynamic pressure and explosive loadings. *Int J Impact Eng*, pages –, 2013.

Jones, N. and Shen, W. Q. ”Criteria for the Inelastic Rupture of Ductile Metal Beams Subjected to Large Dynamic Loads” In *Structural Crashworthiness and Failure*. USA: Elsevier Science Pub, 1993.

Jones, N., Uran, T. O., and Tekin, S. A. The dynamic plastic behaviour of fully clamped rectangular plates. *Int J Solids Struct*, 6:1499–1512, 1970.

Kambouchev, N., Noels, L., and Radovitzky, R. Nonlinear compressibility effects in fluid-structure interaction and their implications on the air-blast loading of structures. *J Appl Phys*, 100:063519, 2006.

Kambouchev, N., Noels, L., and Radovitzky, R. Numerical simulation of the fluid structure interaction between air blast waves and free-standing plates. *Comp Struct*, 85:923–931, 2007.

Kennard, E. H. Cavitation in an elastic liquid. *Phys Rev*, 63:172–181, 1943.

Kinney, G. F. *Explosive Shocks in Air.* New York: MacMillan, 1962.

Krauthammer, T. *Modern Protective Structures.* Boca Raton: CRC Press, 2007.

Krauthammer, T. and Altenberg, A. Negative phase blast effects on glass panels. *Int J Impact Eng*, 24:1–17, 2000.

Langdon, G. S., Ozinsky, A., and Yuen, S. C. K. The response of partially confined right circular stainless steel cylinders to internal air-blast loading. *Int J Imp Eng*, 73:1–14, 2014.

Li, Q. M. and Jones, N. Formation of a shear localization in structural elements under transverse dynamic loads. *Int J Solids Struct*, 37:6683–6704, 2000.

Li, Q. M. and Meng, H. Pressure-impulse diagram for blast loads based on dimensional analysis and single-degree-of-freedom mode. *J Eng Mech*, 128: 87–92, 2002.

Liang, Y., Spuskanyuk, A. V., Flores, S. E., Hayhurst, D. R., Hutchinson, J. W., McMeeking, R. M., and Evans, A. G. The response of metallic sandwich panels to water blast. *ASME J Appl Mech*, 74:81, 2007.

Main, J. A. and Gazonas, G. A. Uniaxial crushing of sandwich plates under air blast: Influence of mass distribution. *Int J Solids Struct*, 45:2297–2321, 2008.

Martin, J. B. and Symonds, P. S. Mode approximations for impulsively loaded rigid-plastic structures. *J Eng Mech Div Proc ASCE*, 92:43–66, 1966.

McMeeking, R. M., Spuskanyuk, A. V., He, M. Y., Deshpande, V. S., Fleck, N. A., and Evans, A. G. An analytic model for the response to water blast of unsupported metallic sandwich panels. *Int J Solids Struct*, 45:478 – 496, 2008.

McShane, G. J., Deshpande, V. S., and Fleck, N. A. The underwater blast resistance of metallic sandwich beams with prismatic lattice cores. *ASME J Appl Mech*, 74:352–364, 2007.

McShane, G. J., Deshpande, V. S., and Fleck, N. A. The underwater blast resistance of metallic sandwich beams with prismatic lattice cores. *Int J Solids Struct*, 74:352–364, 2009.

McShane, G. J., Deshpande, V. S., and Fleck, N. A. Underwater blast response of free-standing sandwich plates with metallic lattice cores. *Int J Impact Eng*, 37:1138–1149, 2010.

Menkes, S. B. and Opat, H. J. Broken beams. *Exp Mech*, 13:480–6, 1973.

Mori, L. F., Lee, S., Xue, Z., Vaziri, A., Queheillalt, D. T., Dharmasena, K. P., Wadley, H. N. G., Hutchinson, J. W., and Espinosa, H. D. Deformation and fracture modes of sandwich strucutres subjected to underwater impulsive loads. *J Mech Materials Struct*, 2:257–275, 2007.

Neumann, J. V. and Richtmyer, R. Method for the numerical computation of hydrodynamic shocks. *J Appl Phys*, 21:232–237, 1950.

Nonaka, T. Some interaction e!ects in a problem of plastic beam dynamics. *ASME Appl Mech*, 34:623–43, 1967.

Nurick, G. N. and Shave, G. C. The deformation and tearing of thin square plates subjected to impulsive loads–an experimental study. *Int J Impact Eng*, 18:99–116, 1996.

Olson, M. D., Nurick, G. N., and Fagnan, J. R. Deformation and rupture of blast loaded square plates—predictions and experiments. *Int J Impact Eng*, 13:279 – 291, 1993.

Radford, D. D., Fleck, N. A., and Deshpande, V. S. The response of clamped sandwich beams subjected to shock loading. *Int J Impact Eng*, 32:968 – 987, 2006.

Ramajeyathilagam, K. and Vendhan, C. P. Deformation and rupture of thin rectangular plates subjected to underwater shock. *Int J Impact Eng*, 30:699–719, 2004.

Rigby, S. E., Tyas, A., and Bennett, T. Single-degree-of-freedom response of finite targets subjected to blast loading , the influence of clearing. *Engineering Structures*, 45:396–404, 2012.

Rigby, S. E., Tyas, A., and Bennett, T. Elastica-plastic response of plates subjected to cleared blast loads. *International Journal of Impact Engineering*, 66: 37–47, 2014.

Rudrapatna, N. S., Vaziri, R., and Olson, M. D. Deformation and failure of blast-loaded square plates. *Int J Impact Eng*, 22:449–467, 1999.

Rudrapatna, N. S., Vaziri, R., and Olson, M. D. Deformation and failure of blast-loaded stiffened plates. *Int J Impact Eng*, 24:457–474, 2000.

Schiffer, A. and Tagarielli, V. L. The response of rigid plates to blast in deep water: fluid structure interaction experiments. *Proc R Soc A*, 468:2807–2828, 2013.

Schiffer, A. and Tagarielli, V. L. The dynamic response of composite plates to underwater blast: Theoretical and numerical modelling. *Int J Imp Eng*, 70: 1–13, 2014.

Schiffer, A. and Tagarielli, V. L. The response of circular composite plates to underwater blast: Experiments and modelling. *Int J Fluids Struc*, 52:130–144, 2015.

Schiffer, A., Tagarielli, V. L., Petrinic, N., and Cocks, A. C. F. The response of rigid plates to deep water blast: Analytical models and finite element predictions. *ASME J Appl Mech*, 6:79, 2012.

Schleyer, G. K. and Hsu, S. S. A modelling scheme for predicting the response of elastic-plastic structures to pulse pressure loading. *Int J Impact Eng*, 24: 759–777, 2000.

Schleyer, G. K. and Mihsein, M. Development of mathematical models for dynamic analysis of structures. In *Conference Proceedings on Structural Design against Accidental Loading*, 1992.

Shen, W. Q. and Jones, N. A failure criterion for beams under impulsive loading. *Int J Impact Eng*, 12:101–121, 1992.

Smith, P. D. and Hetherington, J. G. *Blast and Blallistic Loading of Structures.* Surrey: Butterworth-Heinemann Ltd, 1994.

Spranghers, K., Vasilakos, I., Lecompte, D., Sol, H., and Vantomme, J. Numerical simulation and experimental validation of the dynamic response of aluminum plates under free air explosions. *Int J Imp Eng*, 54:83–95, 2013.

Stronge, W. J. and Yu, T. X. *Dynamic Models for Structural Plasticity.* London: Springer, 1993.

Subramaniam, V. K., Nian, W., and Andreopoulos, Y. Blast response simulation of an elastic structure: Evaluation of the fluid structure interaction effect. *Int J Impact Eng*, 36:965–974, 2009.

Symonds, P. S. Elastic, finite deflection and strain rate effects in a mode approximation technique for plastic deformation of pulse loaded structures. *J Mech Eng Sci*, 22:189–97, 1980.

Symonds, P. S. "Elastic-plastic deflections due to pulse loading" In *Dynamic Response of Structures*. New York: ASCE, 1981.

Symonds, P. S. "A review of elementary approximation techniques for plastic deformation of pulse-loaded structures" In *Metal Forming and Impact Mechanics*. Oxford: Pregamon Press, 1985.

Symonds, P. S. and Frye, C. W. G. On the relation between rigid-plastic and elastic-plastic predictions of response to pulse loading. *Int J Impact Eng*, 7: 139–149, 1988.

Symonds, P. S. and Mosquera, J. M. A simplified approach to elastic-plastic response to general pulse loads. *J Appl Mech Trams ASME*, 107:1–7, 1985.

Symonds, P. S., Kolsky, H., and Mosquera, J. M. Simple elastic-plastic method for pulse loading - comparisons with experiments and finite element solutions. *Inst Phys Conf Ser*, 70:479–86, 1984.

Tan, P. J., Reid, S. R., and Harrigan, J. J. Discussion: 'the resistance of clamped sandwich beams to shock loading' (Fleck N. A, Deshpande V. S. ASME J Appl Mech 2004;71:386401). *J Appl Mech*, 72:978–9, 2005.

Taylor, G. I. "The Pressure and Impulse of Submarine Explosion Waves on Plates" In *The Scientific Papers of Sir Geoffrey Ingram Taylor*. Cambridge: Cambridge University Press, 1941.

Teich, M. and Gebbeken, N. The influence of the underpressure phase on the dynamic response of structures subjected to blast loads. *Int J Protect Struc*, 1:–, 2010.

Teich, M. and Gebbeken, N. Analysis of fsi effects of blast loaded flexible structures. *Eng Struct*, 2013.

Thomson, W. T. *Theory of Vibration With Applications 4th Edition.* London: Chapman and Hall, 1993.

Tilbrook, M. T., Deshpande, V. S., and Fleck, N. A. Underwater blast loading of sandwich beams: Regimes of behaviour. *Int J Solids Struct*, 46:3209–3221, 2009.

TM5-1300. *Structures to resist the effects of accidental explosions.* USA: US Department of the army, 1990.

Vaziri, A. and Hutchinson, J. W. Metal sandwich plates subject to intense air shocks. *Int J Solids Struct*, 44:2021–2035, 2007.

Vaziri, A., Xue, Z., and Hutchinson, J. W. Performance and failure of metal sandwich plates subjected to shock loading. *J Mech Materials and Struct*, 2: 1947–1963, 2007.

Wadley, H., Dharmasena, K., Chen, Y., Dudt, P., Knight, D., Charette, R., and Kiddy, K. Compressive response of multilayered pyramidal lattices during underwater shock loading. *Int J Impact Eng*, 35:1102–1114, 2008.

Wadley, H. N. G., Dharmasena, K. P., He, M. Y., McMeeking, R. M., Evans, A. G., Bui-Thanh, T., and Radovitzky, R. An active concept for limiting injuries caused by air blasts. *Int J Impact Eng*, 37:317–323, 2010.

Wadley, H. N. G., Brvik, T., Olovsson, L., Wetzel, J. J., Dharmasena, K. P., Hopperstad, O. S., Deshpande, V. S., and Hutchinson, J. W. Deformation and fracture of impulsively loaded sandwich panels. *J Mech Phys Solids*, 61: 674–699, 2013.

Wen, H. M. Deformation and tearing of clamped work-hardening beams subjected to impulsive loading. *Int J Impact Eng*, 18:425 – 433, 1996.

Wen, H. M. Deformation and tearing of clamped circular work-hardening plates under impulsive loading. *Int J Pres Ves Pip*, 75:67–73, 1998.

Xue, Z. and Hutchinson, J. W. Preliminary assessment of sandwich plates subject to blast loads. *Int J Mech Sci*, 45:687–705, 2003.

Xue, Z. and Hutchinson, J. W. A comparative study of impulse-resistant metal sandwich plates. *Int J Impact Eng*, 30:1283–1305, 2004.

Yim, H. C. and Krauthammer, T. Load-impulse characterization for steel connection. *Int J Impact Eng*, 36:737–745, 2009.

Youngdahl, C. K. Correlation parameters for eliminating the effect of pulse shape on dynamic plastic deformation. *ASME J Appl Mech*, 37:744–752, 1970.

Youngdahl, C. K. Influence of pulse shape on the final plastic deformation of a circular plate. *Int J Solids and Struc*, 7:1127–1142, 1971.

Yu, T. X. "Elastic Effects in the Dynamic Plastic Response of Structures" In *Structural Crashworthiness and Failure*. Elsevier Science Pub, 1993.

Yu, T. X. and Chen, F. L. The large deflection dynamic plastic response of rectangular plates. *Int J Impact Eng*, 12:605–616, 1992.

Yu, T. X. and Chen, F. L. Failure modes and criteria of plastic structures under intense dynamic loading: A review. *Metals and Materials*, 4:219–226, 1998.

Yu, T. X. and Chen, F. L. A further study of plastic shear failure of impulsively loaded clamped beams. *Int J Impact Eng*, 24:613–629, 2000.

Zhu, F., Wang, Z., Lu, G., and Nurick, G. N. Some theoretical considerations on the dynamic response of sandwich structures under impulsive loading. *Int J Impact Eng*, 37:625–637, 2010.